Master thesis and internship[BR]- Master's Thesis : Study of thermomecanical constraints on optical performances for an Interferometric Small Sat[BR]- Internship (linked to master's thesis)

Auteur : Scheffer, Arthur
Promoteur(s) : Loicq, Jerome
Faculté : Faculté des Sciences appliquées
Diplôme : Master en ingénieur civil en aérospatiale, à finalité spécialisée en "aerospace engineering"
Année académique : 2019-2020
URI/URL : http://hdl.handle.net/2268.2/9086

Study of thermomechanical constraints on optical performances for an Interferometric Small Sat

Arthur Scheffer

Thesis submitted in partial fulfillment of the requirements for the Master's degree in Aerospace engineering (120 ECTS)

Supervisor:
Jérôme Loicq

Committee members:
Denis Defrère, Lionel Jacques & Gaëtan Kerschen

Academic year 2019 - 2020

Study of thermomechanical constraints on optical performances for an Interferometric Small Sat

Arthur SCHEFFER

Supervisor: Prof. Jérôme LOICQ

University of Liège, Faculty of Applied Sciences, Aerospace Engineering.

Abstract

The search of life beyond our world is a major challenging question in the 21st century astrophysics. The development of technologies allows to search for habitable and potentially habitable inhabited planets. The space-based nulling interferometry is one of the most promising process to obtain information such as biological signatures on the spectral footprint of exoplanets. Indeed, this is a direct observation method which enabled to recover the planetary signal by removing the light of its host star.

The objective of this paper is to perform a first thermal analysis of a satellite project conducted by the University of Liège, aimed to observe exoplanets. It studies the impact of temperature modifications onto mechanical constraints, and their influence onto optical performances of the spacecraft. The satellite is described in its environment by a thermal model. All needs of the nulling interferometry and variations over a year are applied to the orbit. Then, the computation process provides all ranges of possibilities for temperature and structure elongation.

These ranges are calculated for a panel of different orbits from Low Earth Orbit to High Elliptical Orbit. Finally, they are all compared in order to make a first selection on the most advantageous ones. They are those which should involve the smallest elongation, then the lowest decline onto optical performances.

Keywords: Space interferometry, Small Sat, exoplanet, thermal analysis, structure elongation.

Acknowledgements

First and foremost, I sincerely thank my advisor Professor Jérôme Loicq for allowing me to join its research team at the Centre Spatial de Liège (CSL). He has been supporting me on my thesis researches since the beginning, even during the pandemic containment. All his advises, feedbacks and its strong knowledge were very helpful to me throughout the project.

Then, I wish to be grateful to Colin Dandumont which closely monitor my work, and was always available to answer my numerous questions. I also thank Lionel Jacques which helped me in the resolution of my thermal interrogations and problems that I have encountered in this thesis. Moreover I had the opportunity to meet several people working at CSL. They all welcomed and discussed with me before the containment and I am thankful for that.

Last but not least, I would like to thank my friends and especially my family for their constant support and encouragement that have been crucial in my motivation during this thesis and my studies.

Contents

List of Figures

List of Tables

Acronyms

CSL	Centre Spatial de Liège
ESA	European Space Agency
ESO	European Southern Observatory
FKSI	Fourier Kelvin Stellar Interferometer
GEO	Geostationary Earth Orbit
GTO	Geostationary Transfer Orbit
HARPS	High Accuracy Radial velocity Planet Searcher
HEO	High Elliptical Orbit
HST	Hubble Space Telescope
HUB	Hubble
IR	Infrared
ISS	International Space Station
LEO	Low Earth Orbit
LIFE	Large Interferometer For Exoplanets
LTAN	Local Time of the Ascending Node
MOL	Molniya
NASA	National Aeronautics and Space Administration
NIR	Near Infrared
OPD	Optical Path Difference
OUFTI	Orbital Utility For Telecommunication Innovation
PASO	Plateau d'Architecture des Systèmes Orbitaux
POL	Polar
RAAN	Right Ascension of the Ascending Node
SIM	Space Interferometry Mission
SMI	Solar wind Magnetosphere Ionosphere Link Explorer (SMILE)
SNR	Signal-To-Noise ratio
SSO	Sun-Synchronous Orbit
TPF-I	Terrestrial Planet Finder - Interferometer

UV Ultraviolet

UVES Ultraviolet and Visual Echelle Spectrograph

VIS Visible

VLT Very Large Telescope

XMM X-ray Multi Mirror

Introduction

"The atmospheric characterization of a significant number of terrestrial planets, including the search for habitable and potentially inhabited planets, is probably the major goal of exoplanetary science and one of the most challenging questions in 21st century astrophysics."[1]

Indeed, life beyond our world is a subject which attract more and more people. In this regards, the University of Liège have thought about the development of a small satellite demonstrator able to collect information from extrasolar planets. This mission is based on the nulling interferometry principle. This process has been demonstrated on the ground, but never on a space mission where atmospheric effects are avoided.

This Master's Thesis is dedicated to the first thermal analysis of this satellite project. Furthermore, the impact of temperature modifications on the mission is studied. Indeed, the thermomechanical constraints such satellite's elongation involve a decline onto optical performances.

First, the mission and its objectives are described. It introduces essential processes and subjects which are studied and discussed all along this work. Then, the operating mode of the satellite is explained: the nulling interferometry.

Then, relevant theoretical backgrounds and methodologies are summarized such as basics principles of heat transfers in space, the principal modes of environmental heating or even the main thermal control methods.

Next, the preliminary thermal study is presented after giving some elementary considerations. This is the first thermal model of the satellite. It is the simplest model because the satellite is represented by a single node. This allows to gather qualitative information on temperature behavior and the on influence of the orbit. It gives a first temperature behavior

After that, an advanced thermal study is developed by associate a node to each satellite's face. This is the core of this thesis. The complete computation process is stated and explained for each step. This is therefore applied to one peculiar orbit, acting as a method demonstrator.

Finally, this process is adapted to all various subjects of this study. They are all compared to each other in order to end with a discussion allowing to draw some conclusions from this work.

Chapter 1

Mission description

The first chapter is dedicated to the description of the mission. It begins by stating some facts onto exoplanet detection and a presentation of the space-based interferometry technique. It continues by a brief state of the art and a highlighting onto this thesis objectives. It ends by the presentation of the satellite and the panel of selected stars.

1.1 Exoplanet detection

More than 20 years ago, scientists expressed doubts about the existence of extrasolar planets. Today, on May 2020, more than 4150 exoplanets are identified, while new exoplanets are still being discovered every day.[2] The Fig. 1.1 shows the total number of discovered extrasolar planets year by year, and the method used to find them. Four principal methods have been mainly used to detect exoplanets: transit photometry, radial velocity, microlensing and direct imaging. The transit photometry is the most commonly used method for detecting planets. More than 75% of detections are conducted through transit. The radial velocity is also well used. It has been used in 20% of the cases. Although very effective, transit, radial velocity and microlensing (98% of all detected exoplanets) are indirect methods. This means that detected planets cannot be directly observed, and astronomers just receive indications that an exoplanet is present.

Indirect methods are very successful for detecting planets, but way less for characterizing them. This is why direct methods are required in order to accurately describe exoplanets. Even if transit photometry can provide a spectral footprint of the planetary atmosphere, the planet has to be perfectly aligned from the astronomer's perspective. For these reasons, the great aim is to make direct observations, which are much more advised in order to conduct spectral analyses of large sample of exoplanets. Indeed, the study of the exoplanet's light is essential to determine the chemical composition and assess physical state of these exoplanets.

The ultimate challenge of direct detection is to capture the light of the planet. However, a planet located at several light years from the Earth appears to be very

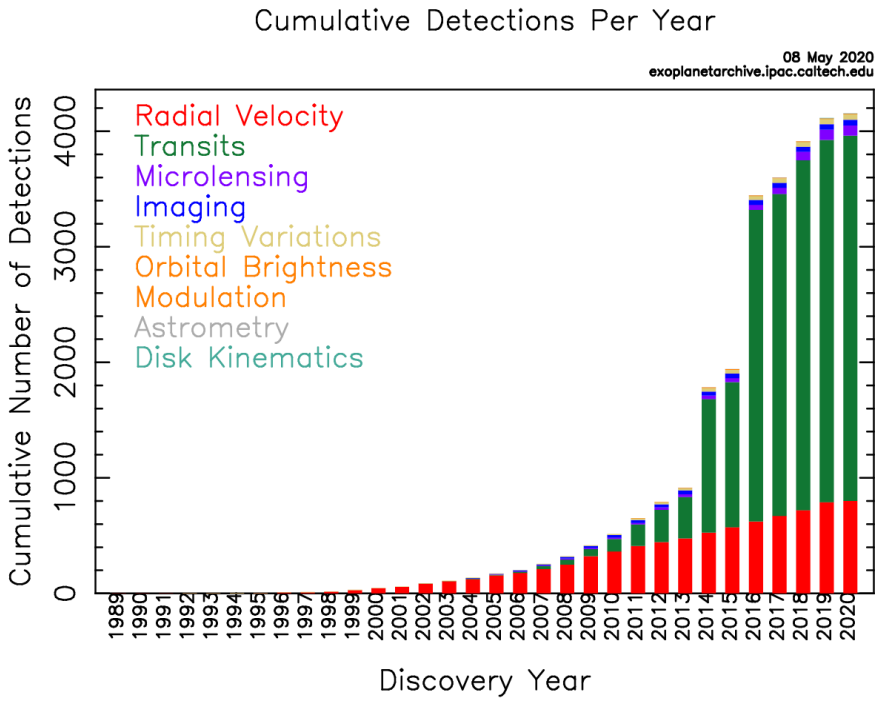

Figure 1.1: Cumulative exoplanets detection per year with their detection methods. Stated on May 08, 2020.[3]

close to its star. Hence, the required angular accuracy has to be extremely high. The closest detected exoplanet is taken as example: Proxima Centauri b. From the Earth point of view, the angle between this extrasolar planet and its star (Proxima Centauri) is 39.5 mas, or also $1.0985 \cdot 10^{-5}$°. Moreover, a planet is outshined by its star because the star is heavily brighter than the exoplanet, by average a billion times. Therefore, this is impossible to distinguish them. For instance, the Proxima b estimated planet-to-star contrast is about 10^{-7} [-] in the VIS-NIR domain.[4]

Two techniques are presently considered in order to perform direct imaging from space: coronagraphy and interferometry. The coronagraphy consists in blocking out the principal component of the direct light coming from the star, and then observing at the pattern of rings provided by the coronagraph. The interferometry process is further described in the next section. This thesis focus on a space platform including an instrument dedicated to nulling interferometry.

1.2 Interferometry in space

1.2.1 Detection method description

In conventional observation of a punctual source at infinity, classical telescope does not form a point but a diffraction pattern. In the case of circular aperture, it consists of a central disk with concentric circles more and more faded. This diffraction figure is called the Airy disk, or Airy pattern. Then, if two observed objects are separated by a too small angle, their Airy disk overlap. Hence, these two objects cannot be clearly distinguished in the image plane. The first minimum

of an Airy pattern occurs for an angle θ approximated by:

$$\theta = 1.22\frac{\lambda}{D} \tag{1.1}$$

where λ is the wavelength of the light and D the telescope diameter. In order to distinguish two objects, the first Airy pattern has to be maximum where the second Airy disk reaches its first minimum. This is the Rayleigh principle.[5] The angular resolution is then directly depending on the size of the Airy disk. Indeed, smaller the Airy pattern, better the image resolution. This is illustrated in Fig. 1.2 in the case of a constant wavelength.

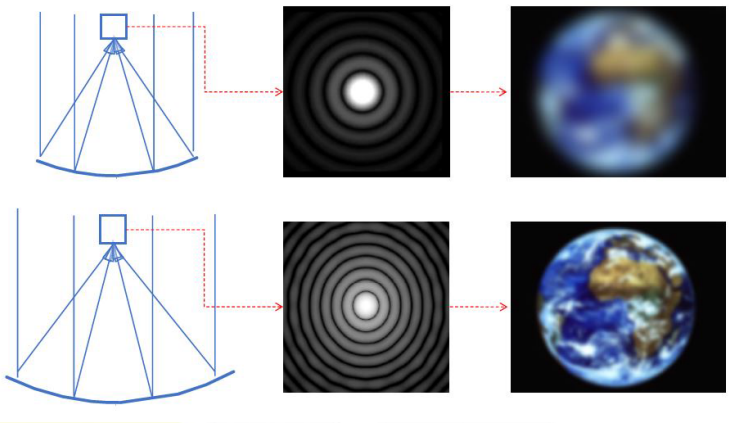

Figure 1.2: Representation of angular resolution with the telescope diameter. Bottom telescope diameter is larger than diameter of top telescope.[6]

The interferometry process consists on the light interference from at least two telescopes separated by a baseline length B. In this technique, the angular resolution is not fully conducted by the telescope diameter anymore, but by this baseline separating them. By combination of these two collected lights, it can be considered as a telescope with an angular resolution given by:

$$\theta = \frac{\lambda}{2B}. \tag{1.2}$$

This θ angle is further used in Fig. 1.3. The great advantage of interferometry is then the possibility to obtain a high angular resolution without having to build a huge telescope. The important key is to increase the baseline length, which is only limited in space by the capacity of the formation flight. This is therefore highly useful to perform space-based interferometry.

The major remaining problem is the brightness contrast between the planet and its host star. This is why Bracewell first introduced the nulling interferometry in 1978.[7] In order to cancel out the starlight, a π phase shift between the two light beams is implemented. By recombination, the two beams are thus in phase opposition. The obtain fringe pattern is then a succession of dark (destructive) and bright (constructive) fringes. In this method, the starlight is highly reduced

by a dark fringe on the line of sight of the interferometer. On the other hand, an optimized baseline length allow the planet to be in the nearest bright fringe, and thus transmitted. The nulling interferometry principle is illustrated in Fig. 1.3.

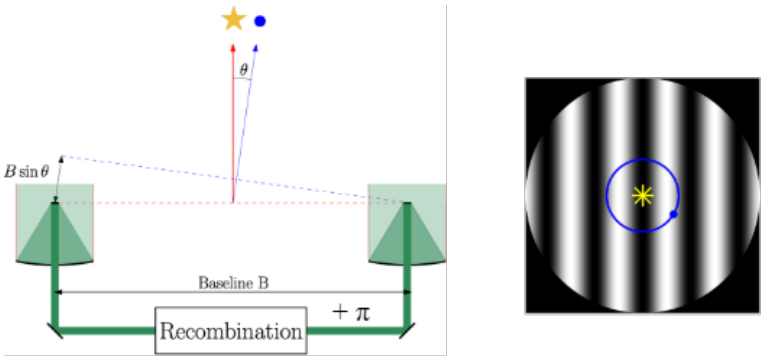

Figure 1.3: Nulling interferometry principle. The star is in *yellow* on a destructive fringe while the planet in *blue* is on a bright fringe.[8]

1.2.2 Interferometer rotation

However, the Earth-like planets are generally undetectable with a static array configuration, even when the starlight is sufficiently reduced. Indeed, the emission is dominated by a series of extraneous signals from the telescope itself, materials in Solar system or even in the vicinity of the targeted star. As a consequence, Bracewell thought about the possibility to rotate the interferometer. Therefore, the planetary signal could be modulated since homogeneous perturbations are constant. A demodulation finally allow to retrieve the planetary signal.[7],[9],[10] The transmission concept is illustrated in Fig. 1.4.

The interferometry method allow working both on Earth and in space. However, a ground-based interferometer is not able to observe wavelengths blocked by the Earth atmosphere. Moreover, a space-based interferometer can be put into an orbit allowing a continuously star observation much longer than on the Earth, due to its rotation.

1.3 State of the art: Space-based interferometry

Several space missions using interferometry were imagined and initiated. Unfortunately, none of them have ever flown.[12] The main reason of these abandons is the too substantial budget. Indeed, the cost of a spatial mission is much bigger than a ground-based mission. Moreover, the lack of technological maturity and the great risk proportion are naturally representing an important curb on these missions. The timeline of the five main space interferometry missions with their cancellation date are given in Fig. 1.5.

[1]The rotation has to follow the star pointing axis, between the two telescopes and in equal distance from them.

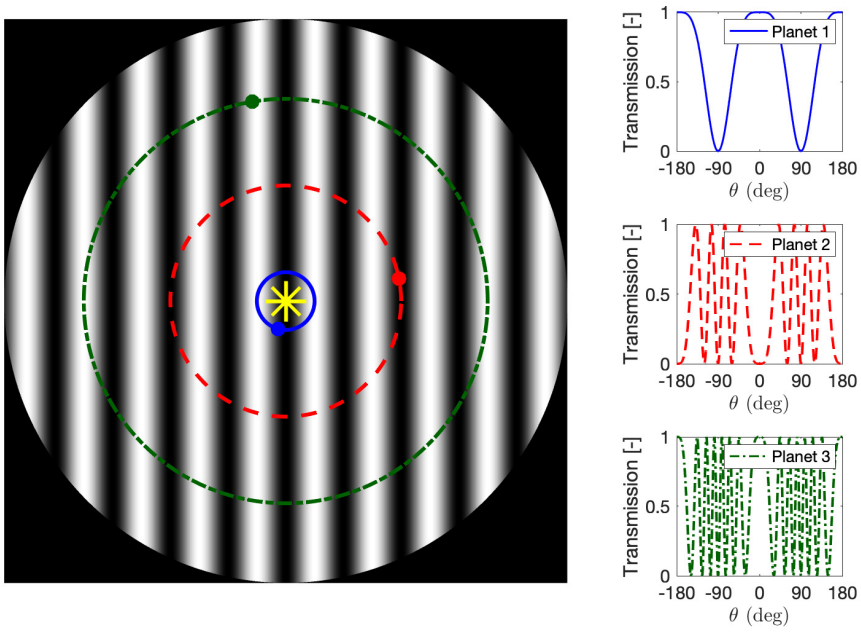

Figure 1.4: Transmission map of a typical nulling Bracewell interferometer. The interferometer rotates and hypothetical planets (1, 2 and 3) cross bright and dark fringes. The signal (small three figures) is modulated. Reference axis for θ is the horizontal one, across the fringes.[11]

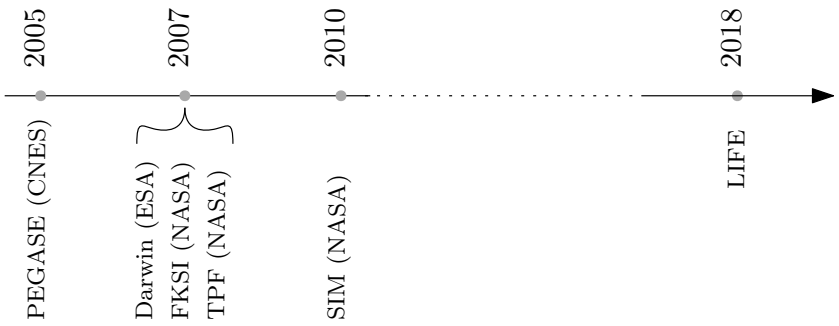

Figure 1.5: Timeline of the main space mission projects using interferometry.[13]

However, due to all limitations from other methods and with the current technology, the interest on space-based interferometry did most recently come back. As a matter of fact, the Large Interferometer For Exoplanets (LIFE) is a mission project which was officially kicked off in 2018.[14] This space mission is designed in order to characterize terrestrial exoplanet atmospheres: biosignatures, habitability and diversity. As such, LIFE is considered as the heir of ESA's Darwin and NASA's TPF-I concepts. This project was presented to ESA in the context of the Voyage 2050 program.[15]

1.4 Project description and thesis objectives

Although the LIFE project is promising, developing a spacecraft using a technology not yet tested under these conditions is a huge challenge. This is why a smaller platform is needed in order to demonstrate the space-based interferometry. The University of Liège and its space research center: Centre Spatial de Liège (CSL), are developing a space-based nulling interferometer on a CubeSat platform. The first objective is to observe and provide information on exoplanets of the nearest stars. The second is to prove this technology in space, which will be a premiere. This finally represents a required first step towards a future large interferometric space-based mission.

This thesis is a development part of the small satellite project. Some thesis have already been done. The first study was the feasibility of a deployable Cubesat carrying two telescopes that have to be deployed with a very high accuracy.[16] The development of a deployable arm to hold mirrors for space interferometric instruments,[17] as a first optic study [18] have already been studied. The observation strategy and in particular the observation possibilities provided for several orbits over a whole year was finally carried out.[13] A PhD is also presently working on this project.[11]

The purpose of this master thesis is to perform the first thermal analysis of this satellite project. That is the study of temperature behavior on each face while taking all various parameter into consideration. For all different considered orbits, the objective is to know how the satellite is reacting in function of its temperature. Indeed, thermal modifications induce mechanical constraints on the satellite dimensions. As shown in Fig. 1.3, the light reaching the two telescopes (located at each satellite extremity) is recombinated in the center with a $+\pi$ dephasing in one arm of the satellite. Then, when the distance between the two telescopes is non uniformly changed, the light will not browse the same distance in each arm anymore. That is called the Optical Path Difference (OPD). It has to be corrected with a dephasing modification in order to keep the arms in the same length. With a simple thermal model, the thermal environment of the satellite has therefore to be known for each selected orbit.

1.5 Satellite

The satellite geometry is not yet fixed as the project is still at its beginning. However, the development is heading towards a 12U small satellite model displayed in Fig. 1.6. This is this geometry which is retained for all this study. The model is in fact a combination of four aligned 3U Cubesats. This enables to have a baseline of about 1.2 m. This length is important to obtain the finest pointing and stability. This combination involves the satellite to possess deployment mechanisms in order to operate once it will be launched. The two apertures are located in each tip of the plateform, while the recombination takes place in the centre of the Cubesat. Other components are however still undetermined.

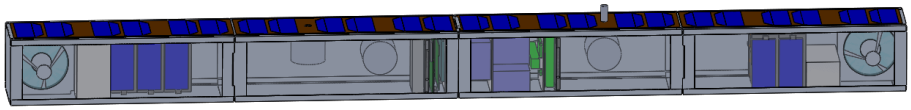

Figure 1.6: Satellite CAD model used for this study. The configuration is a 12U CubeSat: 1200×100×100 mm. This model is used for the rest of this project, but it is subject to change in the future.

1.6 Targeted stars

The satellite has to point a star to observe planets in their vicinity. As the goal is to demonstrate the technology, the five closest stars with at least one confirmed exoplanet are selected. As they are the nearest systems, it ensures therefore a better probability to succeed an exoplanet observation. Furthermore, these five stars limitation is even more justified since such a mission is limited in time. It is then better to concentrate the study on those stars rather than on too many targets.

The five selected stars of this mission are thus: Proxima, Barnard's star, Epsilon Eridani, Ross 128 and Tau Ceti. Their principal characteristics are all summed up in the Tab. 1.1.

	Proxima	**Barnard**	**ϵ Eridani**	**Ross 128**	**τ Ceti**
Distance [LY]	4.3	5.96	10.4	11.0	11.8
Mass [$M_\odot$]	12%	14%	83%	17%	78%
Constellation	Centaurus	Ophiucus	Eridanus	Virgo	Cetus
Type (dwarf)	red	red	orange	red	yellow
Confirmed exoplanet	b	b	b or Ægir	b	b to h?
Detection	Radial velocity	Radial velocity	Radial velocity	Radial velocity	Radial velocity
Mass [$M_\oplus$]	1.6 [$M_\oplus$]	3.2 [$M_\oplus$]	0.78 [M_J][2]	1.4 [$M_\oplus$]	-
Discovery year	2016	2018	2000	2017	2017

Table 1.1: Summary of principal characteristics of studied stars and their companion exoplanet.

In addition, all stars have some peculiarities. First, the Alpha Centauri system is composed of three stars. Alpha Centauri A and Alpha Centauri B (the two spincipal stars of this system) are forming a double star. Proxima Centauri is much smaller and colder than the others and is completing this system illustrated in Fig. 1.7. The European Southern Observatory (ESO) was the first announcing an exoplanet orbiting around Proxima. It has been found using two spectrographs, HARPS telescope from ESO (La Silla Observatory) and UVES on the Very Large Telescope (VLT).[19] Although this is known that this exoplanet is located in the habitable zone of its system, much information about this extrasolar planet are still unknown. This is why the direct method of nulling interferometry is convenient in that case. Due to its nearest exoplanet from Solar system, Proxima is considered as the principal target of the mission. Hence, performances of the orbits while pointing to Proxima star will be carefully analysed.

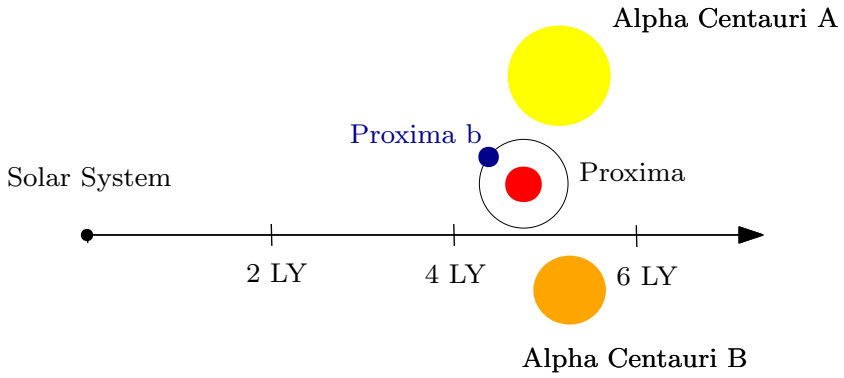

Figure 1.7: System layout of the Alpha Centauri system.[13]

Barnard's star b exoplanet was confirmed also by the ESO in November 2018. Its location is not in the habitable zone, besides, its surface is estimated to be at a constantly frozen temperature of -70°.[20] There is nonetheless a possibility of other orbiting planet.

Unlike other stars, Epsilon Eridani (or ϵ Eridani) can be observed by the naked eye. Its exoplanet was first suspected in the early 1990s, and finally officially discovered in August 2000 mainly thanks to the telescope at McDonald Observatory.[21] The star is expected to be surrounded by two debris disks. In addition, some astronomers are suggesting that another planet is orbiting Epsilon Eridani located at the borders of the second debris disk.[22]

Ross 128b was discovered in November 2017 by the HARPS instrument from ESO. This is a tempered planet orbiting around a calm star. Moreover, this exoplanet is expected to be telluric such as the Earth.[23]

The last but not least is Tau Ceti (or τ Ceti). Indeed, it was first suggest in December 2012 by ESO, a system of five candidates planets (b, c, d, e and f) orbiting

[2] $[M_J]$ unit represents the mass of Jupiter.

Tau Ceti.[24] Moreover, new observations with the improved technology found two more candidates (g and h) in August 2017. The e and f exoplanets were confirmed as candidates, besides b, c which were not consistently detected, while d was not found in all data sets.[25] In any case, the question of existing planets orbiting Tau Ceti no longer arises.

Furthermore, as the potential life beyond the Solar system is a cornerstone of 21^{st} century astrophysics, the race to find new extrasolar planets is more and more significant. Consequently, some new exoplanets from other host stars have been discovered since the beginning of this thesis. Some of them are even closer than Tau Ceti:[26]

- Wolf 359
- Lalande 21 185
- Lacaille 9352
- Struve 2398 B
- Groombridge 34 A.

However, it was decided to continue at this time the study on the five stars first initiated since the objectives remain the same. However, it is obviously possible to integrate these stars in the future.

Chapter 2

Thermal control

This chapter is introducing theoretical elements for the thermal control of satellites. These are essential to understand the temperature computation methodology of following chapters. It begins by a review of heat transfer principles in space. It continues by a presentation of thermal loads acting on a spacecraft in its environment. It ends by a description of standard methods allowing the thermal control of a satellite.

2.1 Heat Transfers in space

The three modes of heat transfer are conduction, convection and radiation. However, as pressure is extremely low in space, heat transport cannot be done by convection but only by conduction and radiative transfer.

2.1.1 Conduction

Thermal conduction is due to atomic and molecular activity inside a matter. It thus appears inside the satellite between the different elements. These particle interactions involve a transfer of energy from the hottest to the coldest surface. This heat conduction is driven by Fourier's law. For a 1D case, in the x-direction, the heat flux q_x $\left[\mathrm{W/m^2}\right]$ is given by:

$$q_x = -k\frac{dT}{dx} \tag{2.1}$$

where k [W/m·K] is the thermal conductivity of the material and dT/dx the temperature gradient.

Considering a steady and linear flow between two isothermal surfaces quoted i and j, the heat rate by conduction $Q_{\mathrm{i,j}}$ [W] is then:

$$Q_{\mathrm{i,j}} = k\frac{A}{L}(T_{\mathrm{i}} - T_{\mathrm{j}}) = GL_{\mathrm{i,j}}(T_{\mathrm{i}} - T_{\mathrm{j}}) \tag{2.2}$$

where T_i and T_i [K] are the temperatures at surface i and j, A is the cross section through the path of heat exchange and L [m] its length. This also introduces the thermal conductance $GL_{\mathrm{i,j}}$ [W/K].

2.1.2 Radiation

2.1.2.1 Blackbody

In space applications, radiation is highly important because this is the only way to receive and reject heat in space. This is achieved by the emission and absorption of photons, and depends on the thermo-optical properties of the material. In order to understand this process, this is useful to introduce the concept of a blackbody:[27]

1. This is an ideal object which perfectly absorb all incident radiation, regardless of direction and wavelength.
2. There is any surface which is able to emit more than a blackbody for a given wavelength and temperature.
3. The radiation emission of blackbody is independent of direction. This is thus a diffuse emitter.

Since those conditions are assumed, the spectral emissive power of a blackbody is given by the Planck distribution:

$$E_{\lambda,bb}(\lambda,T) = \frac{C_1}{\lambda^5\left[exp(C_2/\lambda T)-1\right]} \tag{2.3}$$

with $C_1 = 2\pi hc_0^2$ and $C_2 = (hc_0/k_B)$, where h and k_B are the universal Planck and Boltzmann constants, c_0 the speed of light, λ the wavelength and T the absolute temperature of the blackbody. This equation representing Planck's law is plotted in Fig. 2.1.

This Fig. 2.1 shows that the Sun is approximated as a blackbody with a temperature of 5800 K, which has its maximum radiation in the visible spectrum. Furthermore, at any wavelength, the maximum radiation value increases when temperature is increasing. The maximum corresponding wavelength $\lambda_{\max}$ μm follows the Wien's displacement law:

$$\lambda_{\max} = \frac{C_3}{T}. \tag{2.4}$$

with $C_3 = 2898$ μm·K.

Then, the emissive power of a blackbody E_b is introduced by integration of $E_{\lambda,b}(\lambda,T)$ from Eq. 2.3. It is called the Stefan-Boltzmann law:

$$E_{bb} = \sigma T^4 \tag{2.5}$$

with the Stefan-Boltzmann constant $\sigma = 5.670 \times 10^{-8}$ W/m^2·K^4, depending on C_1 and C_2 given above in Eq. 2.3.

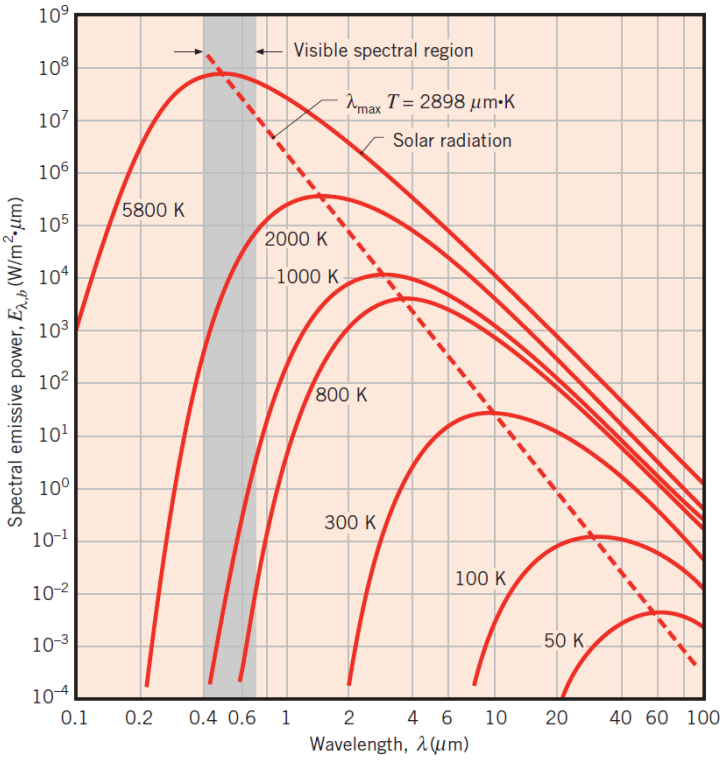

Figure 2.1: Planck's distribution: spectral blackbody emissive power. Taken from [27].

2.1.2.2 Real surfaces

Although the concept of blackbody is presented, this ideal surface behavior is not convenient for real surfaces. Indeed, those are in reality not following the Planck distribution and are not diffuse anymore. This difference is presented in Fig. 2.2.

In order to understand real surfaces behavior, their specifics parameters (each in range from 0 to 1) have to be presented: emissivity ϵ, absorptivity α, reflectivity ρ and transmissivity τ. The emissivity is the ratio between the emissive power of a real surface to the one of a blackbody. Other parameters obviously describe the absorption, reflection and transmission of these surfaces. They are wavelength and angular dependents. For a semi-transparent medium and any given wavelength λ, it respects:

$$\alpha_\lambda + \rho_\lambda + \tau_\lambda = 1. \tag{2.6}$$

Moreover, Kirchoff's law of thermal radiation gives this equality, which is always valid without any restriction onto spectral or directional properties:

$$\epsilon_{\lambda,\theta} = \alpha_{\lambda,\theta}. \tag{2.7}$$

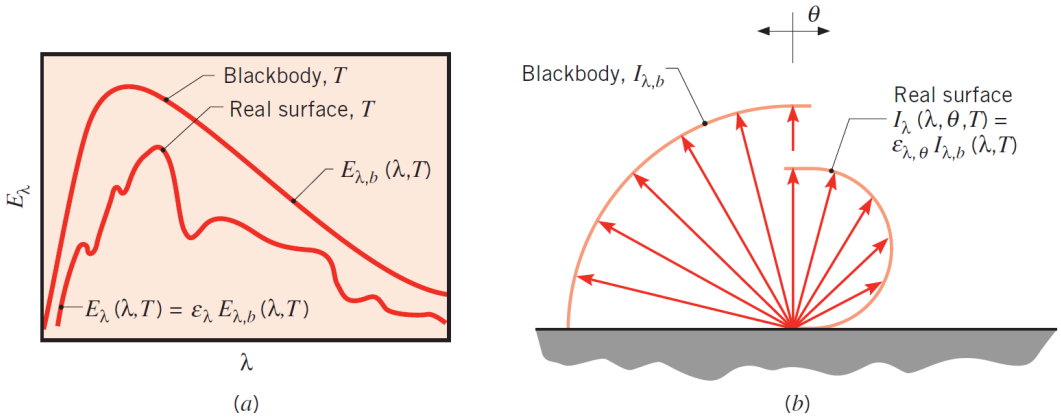

Figure 2.2: Comparison between emission of a blackbody and a real surface for (a) Spectral distribution and (b) Directional distribution. Taken from [27].

However, the semi-grey assumption is used by space engineers in order to simplify space thermal calculations. Therefore, the wavelength domain is divided in two spectral bands where emissivity and absorptivity are considered as constant:[28]

- Thermal visible [0.2 μm - 4.0 μm]: $\alpha := \alpha_{VIS} = \epsilon_{VIS}$,
- Thermal infrared [4 μm - 50 μm]: $\epsilon := \epsilon_{IR} = \alpha_{IR}$.

2.1.2.3 View factors

As radiation exchanges appear between surfaces, this is important to know how surfaces are seeing each others. This is achieved by the concept of view factor $F_{i,j}$ between surfaces A_i and A_j. It represents the proportion of radiation leaving A_i and intercepted by A_j. This is shown in Fig. 2.3.

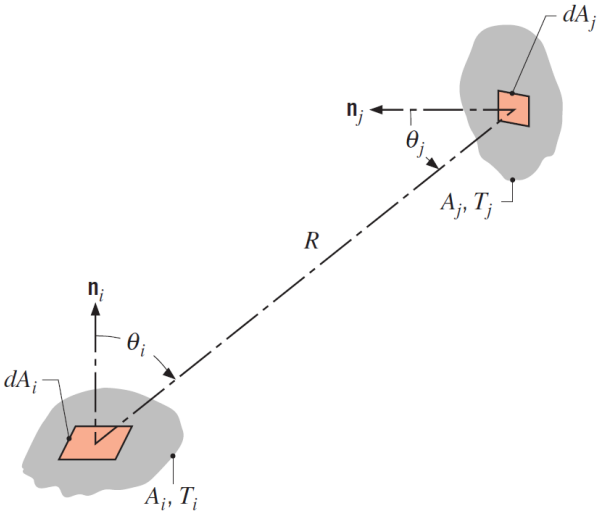

Figure 2.3: View factor of a radiation exchange between two surfaces A_i and A_j. Taken from [27].

Mathematically, this concept is defined by:

$$F_{i,j} = \frac{1}{A_i} \int_{A_i} \int_{A_j} \frac{\cos \theta_i \cos \theta_j}{\pi R^2} dA_i dA_j. \tag{2.8}$$

It respects two fundamental relations:

$$A_i F_{i,j} = A_j F_{j,i} \tag{2.9}$$

$$\sum_{j=1}^{N} F_{i,j} = 1 \tag{2.10}$$

where N is the number of surfaces in the enclosure. Moreover, the Gebhardt factor is another convenient concept because it takes into account surface properties and geometry, thus all reflections. This gives the fraction of the energy coming from a surface A_i and absorbed by A_j. This is computed by:[29]

$$B_{i,j} = F_{i,j}\epsilon_j + \sum_k F_{i,k}(1 - \epsilon_k) B_{k,j}. \tag{2.11}$$

The heat rate obtained by radiation $Q_{i,j}$ [W] can finally be computed:

$$Q_{i,j} = \sigma \epsilon_i A_i B_{i,j} (T_i^4 - T_j^4) = \sigma G R_{i,j} (T_i^4 - T_j^4). \tag{2.12}$$

It then defines the radiative exchange factor $GR_{i,j}$ between the two surfaces A_i and A_j.

2.2 Thermal environment

A satellite orbiting a planet receives heat loads by radiation from its environment. The main external fluxes originate from the direct solar flux, the sunlight reflection on the Earth and the Earth IR radiation. Those are depicted in Fig. 2.4.

The first one is the direct solar flux. This is the greatest source of environmental heating when a spacecraft is orbiting Earth. The distance between the Sun and satellite is assumed to be equal to the one between Sun and Earth. With this, the solar constant S_c representing the rate at which energy browses the mean Sun-Earth distance (1 AU) is 1367 W/m^2. It can vary from 1322 to 1414 W/m^2 respectively at summer and winter solstice due to the Earth's elliptic orbit around the Sun. If the satellite has to move far away from the Earth, the solar constant would change. Nevertheless, the change is not significant because even with the further apogee orbit (n.d.l.r. SMI[3] orbit), the modification should be only by around 3 W/m^2, which represents less than 0.2% of S_c.

[3]Orbit from SMILE mission, 127 000 km apogee altitude.

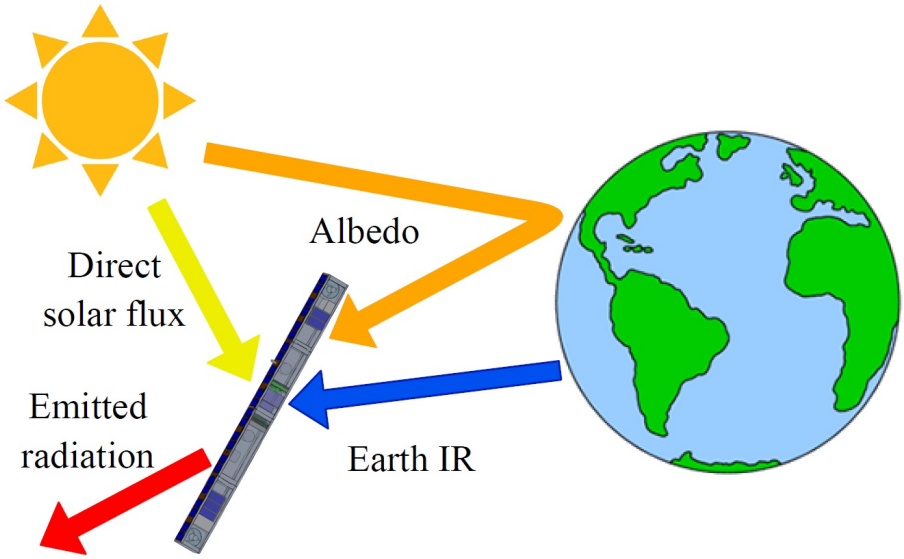

Figure 2.4: Thermal exchanges between the satellite and its environment in LEO.

The second source is the albedo radiation. This is due to the reflection of sunlight by a planet. It depends on surface reflectivity properties of the planet, the view factor with the satellite and the β angle (angle between Sun vector and its projection onto the orbital plane). This mode of radiation is highly variable. Indeed, the albedo radiation depends both of space and time, due to different atmospheric and surface properties. It could vary from 0.05 for oceans to 0.8-0.9 for shiny clouds or ice caps. Finally, the Earth albedo for this study has been approximated by a mean value of 0.3 [-].

The third environmental source is the Earth infrared radiation. This emitted energy from planete's surface and atmospheric gases can be approximated as an equivalent 255 K blackbody, previously explain in Sec. 2.1.2.1. This emission is also spatial and temporal variable, but less significantly than the albedo. This global temperature is representing the Earth's temperature before reaching its atmosphere.

The last heat load corresponds to the internal dissipated power in on-board electronic components. This is explained by the Joule effect. Another possible environmental load could be the aerothermal flux. Nevertheless, it is neglected in this work because it is only convenient during launch or reentry phases.

Throughout its mission, the satellite will be subject to a variation of all previously cited thermal loads. It will be spatially and temporally depending. For example, there will be only Earth's IR radiation during eclipse, or only solar radiation when orbiting at very high altitude. But, there is all the same a cold source for the spacecraft: the Deep Space. It can be modeled as a blackbody emitting at 3 K, corresponding to the Cosmic Microwave Background from the Big Bang.

2.3 Thermal control methods

During its operating mode, temperatures of the different parts of a satellite have to respect their thermal requirements. For this purpose, there are many methods allowing the management of heat transfers on a satellite. Those are divided in two categories: active and passive methods. The most commonly used ones are listed in the Tab. 2.1.[30]

Passive	Active
Radiation	**Heater**
- Coating	- Thermostat control
- MLI blanket	- Electronic control
- Radiator	- Ground control
Latent heat and ablation	**Peltier element**
- Thermal protection system	**Heat pipes**
- Phase change material	- Fixed or variable conductance
Conduction	**Fluid loops**
- Structural material	- Mono or diphasic fluid
- Doubler, filler	
- Washer, strap, bolt	**Louvers**
- Foam	**Coolers**

Table 2.1: Main used thermal control methods.[30]

A passive method does not require any external power because it is not using any movable mechanism. Generally, this kind of method is firstly studied in a thermal design because of its simplicity, its reliability and its low cost. Moreover, this does not provide any constraint on the spacecraft.

However, passive methods are limited in thermal dissipation and are not very precise. Therefore, this is often not enough sufficient in order to ensure a convenient thermal control for all components. Indeed, when the temperature range has to be very tight and precise or when a large amount of heat power has to be managed, active methods are used in addition to the passive ones. In contrast, those control methods are expensive, cumbersome and finally require power.

Chapter 3

Elementary considerations

The third chapter aims to present all additional information needed before performing a first thermal analysis of the satellite and explains it. First, the conventional used notations of this work are introduced. Next, the methodology which will be followed throughout this thesis is detailed. Finally, each orbit of the selected panel is described with its orbital elements.

3.1 Notations

All along this work, the behavior of the satellite will be studied and explained according to its faces. The reference frame used for computations takes its center in the geometrical center of the satellite. All faces are defined with respect to its normal. Those are illustrated in Fig. 3.1. The $+X$ face is the face which is always pointing the star. The $+Y$ is considered as the side face of the satellite. This is the smallest of all faces (as $-Y$). Then, $+Z$ is the upper face. Its size is the same than $+X$. Obviously, faces $-X$, $-Y$ and $-Z$ are the opposites to $+X$, $+Y$ and $+Z$ faces.

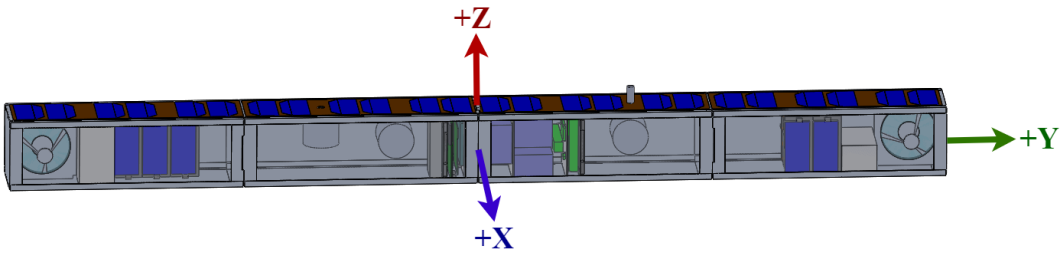

Figure 3.1: Satellite CAD model with normals. The configuration is a 12U CubeSat: 1200×100×100 mm.

3.2 Methodology

The first step of the study is to make a panel of orbits which will be studied. In order to be aware of a wide range of possibilities, it is important to first select many

orbits with some differences in their behavior. This is why one has to consider some common but also some particular orbits since they all have their own features. All orbital elements and altitude have therefore to be fixed.

Once orbits are selected with their corresponding orbital elements, the SIMUCIC extension of SCILAB and CelestLab (Space Mechanics Toolbox) softwares allow to perform simulations. This extension is developed by the CNES and especially by the "Plateau d'Architecture des Systèmes Orbitaux" department (PASO). It enables to propagate each selected orbit and also provides much additional useful information. It finally provides satellite positions and velocities, but also the β angle value, Sun visibility, Sun position and many more other parameters all over the time of simulation. It was decided in this work to study orbits over the whole 2020 year. The time step is set to 60s, which is a good compromise between accuracy and computational time.

After the use of MATLAB to verify positions and orbital elements provided by the propagator, the next step is to define the thermal model of the satellite. This allow to represent the satellite in its environment. It defines the characteristic values describing the environment (Sun, albedo and Earth IR) but also the ones of the satellite components as emissivity, absorptivity or even capacitance. The model is often very basic in the beginning, but it can progressively becomes more and more complex according to the project development.

The thermal analysis is finally done, allowing to gather temperature profiles and ranges of each computed situation. It therefore enables to discuss on thermal constraints and represents temperature ranges appearing over the year. The elongation resulting from these temperature changes, and which is reducing optical performances can therefore be discussed. It ends by the comparison between all different orbits.

3.3 Orbits

This section presents all orbits selected for this work. In order to be convenient with the previous study on this satellite concerning the observation strategy,[13] it was decided to use the same nine types of orbit. Indeed, chosen orbits have all their special feature. By considering all of them, it covers a wider range of possibilities that could be encountered in space. Some are located very close to the Earth: the Low Earth Orbits (LEOs), whereas other have their apogee altitude far away from the Earth: the High Elliptical Orbits (HEOs). In addition, some orbits have been slightly modified from the observation strategy.[13] This is due to the actualisation of real missions or even orbital corrections (SMILE orbit).

Orbits can be classified by many different ways: altitude, shape, or by their orbital parameters. The choice made is to separate circular and elliptic orbits. Furthermore,

it allows to differentiate LEO from HEO, besides GEO which is a particular case of circular orbit with a high altitude. They are presented in Tab. 3.1.

Circular Orbits	Elliptic Orbits
GEO: Geosynchronous	GTO: Geostationary Transfer
HUB: Hubble	MOL: Molniya
ISS: International Space Station	SMI: SMILE
POL: Polar	XMM: XMM-Newton
SSO: Sun-Synchronous	

Table 3.1: Catalogue of selected orbits.

3.3.1 Circular orbits

The orbital parameters of selected circular orbits are presented in Tab. 3.2. Their peculiarity is that the eccentricity is null, or pretty close to zero. They are all put into their theoretical values, considered as initial values. As HUB and ISS orbits are inspired from real mission, selected parameters are thus the real ones.[31],[32] They are chosen in order to be as close as possible that the beginning epoch time of simulation files, i.e. 2020 January 01.

	Altitude [km]	e [-]	a [km]	i [°]	RAAN [°]	ω [°]	Period [min]
HUB	540	0.00030	6 916	28.47	353	82	95
ISS	408	0.00053	6 779	51.64	97	93	93
SSO	400	0	6 771	97	[0:360][4]	0	93
	600	0	6 971	97.75	[0:360]	0	97
	800	0	7 171	98.56	[0:360]	0	101
POL	896	0	7 274	90	12.5	0	103
GEO	35 786	0	42 157	0	0	0	1 436

Table 3.2: Orbital parameters of selected circular orbits. The altitude is considered from the Earth's surface, with the mean Earth radius $R_\oplus = 6\ 371$ [km].[13]

HUB The characteristic parameter of this orbit is its low inclination. It stands out by its ease of launch. As the Hubble Space Telescope (HST), a take-off from Cape Canaveral (Florida) leads the satellite to reach an inclination of 28.5° without any maneuver. If the orbit does not need a change of its inclination, it will considerably reduce the amount of required thrust for the mission. Indeed, an inclination modification needs a change in velocity which is proportional to the double of its own velocity. Therefore, avoiding this maneuver allows an easier and cheaper launch, which is relevant for the study of this orbit.

[4] At SSO, the study is made for a RAAN Ω from 0° to 180° by a range of 30° because this orbit is symmetric.

ISS Study of the ISS orbit is necessary. Indeed, this is now possible to deploy small satellites into orbit from the ISS. The satellite is first sent to the station like a cargo load. Then, a robotic arm of ISS places a Cubesat deployer in order to release the small satellite into orbit.[33]

SSO The peculiarity of this orbit is that the orbital plane makes a constant angle with the Sun vector. It allows to see the Earth's surface in consistent lighting conditions over time. This is then possible to compare images everyday at exactly the same local time throughout the life of the spacecraft. Moreover, it takes advantage of leverage natural orbital perturbations (J_2 due to the oblateness of the Earth) to be more stable. Indeed, for inclinations between 95° and 105°, a good coordination of altitude and inclination enables a precession rate which is exactly the same than the Earth's rotation around the Sun.

It was decided to study SSO with 3 different altitudes: 400, 600 and 800 km (SSO_{400}, SSO_{600} and SSO_{800}). In order to have an heliosynchronous orbit, the associated inclination i has to be chosen with respect to the precession rate of the Earth:

$$\Delta\Omega = -\frac{3}{2} J_2 \frac{R_\oplus^2}{p} \sqrt{\frac{\mu}{a^3}} \cos(i) \tag{3.1}$$

where:

- $\Delta\Omega$ [rad/s] is the precession rate,
- $J_2 = 1.082 \times 10^{-3}$ [-] is the zonal harmonic quantifying the Earth's oblateness,
- $R_\oplus = 6\,371$ km the Earth's mean radius,
- $p = a(1 - e^2)$ [km] is the semi-latus rectum of the orbit. It is equal to the semi-major axis a since the orbit is circular.
- $\mu = 3.986 \times 10^5$ km^3/s^2 is the standard gravitational parameter of the Earth.

Knowing the precession rate of the Earth is one rotation per sidereal year, the corresponding inclinations for SSO_{400}, SSO_{600} and SSO_{800} are then respectively 97°, 97.75° and 98.56°. Furthermore, the design of batteries is simplified since solar arrays can be oriented in such a way that they are always under sunlight conditions.

POL Polar orbits are LEOs with an inclination of 90°. Therefore, the corresponding orbital plane will cross over both poles on each revolution. As the Earth is moving around the Sun, its angle of illumination is changing over time. But, a major advantage from other orbits is the precession rate $\Delta\Omega$ which is null. Indeed, they are not affected by perturbations due to the oblateness of the Earth since $\cos(i)$ is a factor of zonal harmonic J_2. This is why they can also be called inertial orbits.

However, it has to be strictly polar because a deviation of 0.1° involves a drift of 4°/year.[34] The chosen orbit is the one of CoRoT satellite (896 km) from CNES because its mission is to observe opposite targets for several months without any

Earth's eclipse. Finally, it was decided to select the optimal RAAN with respect to targeted stars position. Then, the average of right ascension of the stars leads to a RAAN around 12.5°.[35]

GEO It is a circular geosynchronous orbit with no inclination. It has an exact altitude of 35 786 km, with a period of one sidereal day (23h 56min 04s). It allows the satellite to stay over the same longitude of the Earth. Then, it travels in synchronization with the Earth's rotation.

All trajectories corresponding to circular orbits are drawn in Fig. 3.2a. For SSO, only the 800 km altitude case (SSO_{800}) is presented in order to avoid an overloaded figure. Moreover, GEO is represented with trajectories corresponding to elliptical orbits because of its more appropriate scale. Only the first period is presented for each orbit. Indeed, it allows to avoid showing path superpositions due to the drift motion on each orbit, except for POL orbit.

3.3.2 Elliptical orbits

Orbital parameters of selected elliptical orbits are presented in the Tab. 3.3. They are all put in their initial values, and are obviously changing during simulation. The XMM orbital parameters are the real ones of the mission.[36] They are chosen in order to be as close as possible than the beginning epoch time of simulation files, i.e. 2020 January 01.

	Apogee [km]	Perigee [km]	e [-]	i [°]	RAAN [°]	ω [°]	Period [hr]
GTO	35 786	300	0.73	0	0	0	10.5
MOL	39 700	600	0.74	63.4	85	270	12
SMI	127 000	5 000	0.84	98.2	[0:360][5]	280	54
XMM	114 000	9 000	0.77	71.1	326	94	48

Table 3.3: Orbital parameters of selected elliptical orbits. Apogee and perigee altitude are computed from the Earth's surface, with a considered mean radius of $R_\oplus = 6\,371$ km.[13]

GTO The geostationary orbit is an intermediate orbit which allows to reach GEO. A transfer orbit is usually not used as a final trajectory, but it could be relevant to consider it for this work. Indeed, as this is a small satellite project, it is possible to take part to a bigger mission reaching the GEO as a secondary payload. More and more companies, especially startups, are offering or will offer launches in such orbit.[37]

MOL Molniya is one of the most common eccentric orbits. This orbit was used by Soviet Union in the sixties for civil and military telecommunication.[38] This is

[5] At SMI orbit, the study is made for a RAAN from 0° to 360° by a range of 60° in order to obtain a wider range of possibilities.

due to its ability to act like a geostationary orbit during around 8 continuous hours. Indeed, considering the great difficulty to reach high latitudes for GEO, a three satellites combination in Molniya orbit enables to obtain a continuous and global coverage. Its orbital period is 12h (half a sidereal day). Furthermore, like SSO, it takes advantage of orbital perturbation to be more stable. In point of fact, the J_2 term representing Earth's oblateness affects location of perigee. This shifting of perigee is a factor of altitude, inclination and eccentricity, but inclination has the greatest effect. However, an inclination of 63.4° allows to lock the perigee at its original position and thus avoid drift motion. Therefore, an argument of perigee locked at 270° enables solids to spend the majority of its orbital period over the Northern hemisphere. However, a RAAN drift is still unavoidable.

SMI The SMILE mission is an ESA and CAS (Chinese Academy of Sciences) planned to be launched in 2023 to study the interaction between Solar wind and the Earth magnetosphere.[39] It is defined by an orbit with a high inclination and highly elliptical. Moreover, it takes a third of the way to the Moon at apogee, which represents 20 times the Earth mean radius, i.e. 127 000 [km]. Scientific goals of this mission make this orbit relevant to examine because it is able to collect continuous observations for very long periods. However, a last orbital parameter is still undetermined. Therefore, it was decided to study the case of six different RAAN's: 0, 60, 120, 180, 240 and 300°.

XMM The XMM-Newton mission is relevant to consider because of its extremely elliptic orbit. The major axis is nearly one third of the distance to the Moon. The satellite was launched by ESA in December 1999.[40] The objective of the mission is to study some of the most violent space phenomena, where celestial X-ray sources cannot be blocked by the atmosphere of the Earth. In order to respect needs of the mission, the orbit has to cross the radiation belts without any obstruction during time of observation. It is then obvious that orbital parameters of XMM are going to change a lot over time. As an example, the initial inclination was 40° at start of the mission, against more than 70° actually.

The Fig. 3.2 is illustrating orbital trajectories of selected orbits. As for Fig. 3.2a, trajectories corresponding to elliptical orbits and GEO are drawn in Fig. 3.2b. For SMI, only the 120° RAAN case (SMI_{120}) is presented in order to avoid an overloaded figure. For same reasons than circular orbits, only the first period of each orbit is presented.

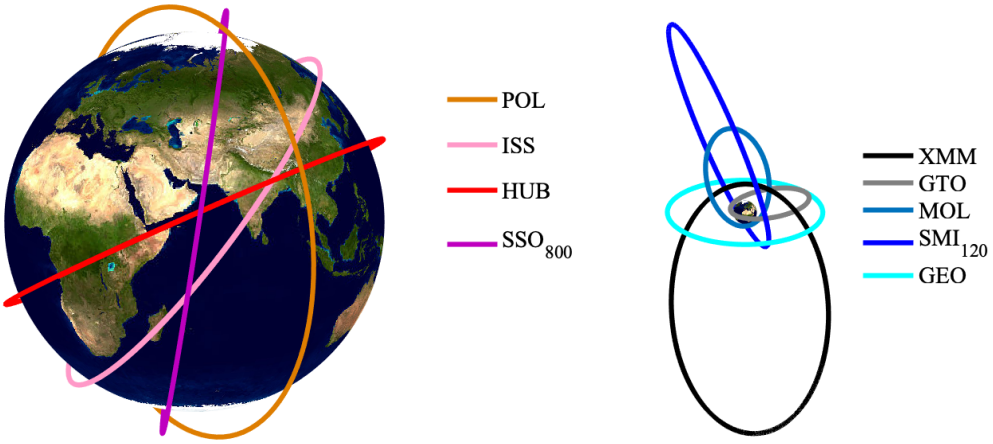

(a) Circular orbits. **(b)** Elliptical and GEO orbits.

Figure 3.2: Representation of orbital trajectories from circular and elliptical orbits.[13]

Chapter 4

Preliminary thermal analysis

At this stage of the thesis, all elements needed for a first thermal analysis are presented. This can therefore be done for a basic thermal model. In this chapter, a single node transient model of the satellite is created and implemented in MATLAB. It begins by the computation of all external thermal fluxes for the purpose of describing the satellite in its environment. It continues with the thermal model presentation, including static and cyclic transient models. A sensitive analysis onto estimated satellite parameters is done. It ends by the results provided by this first thermal analysis. The objective is to have a first idea of the temperature behavior before analyze a more complex model.

4.1 External thermal fluxes

This section explain how to compute all external fluxes corresponding to environmental thermal radiations presented in Sec. 2.2. Those are essential to be known since it describes the thermal loads acting on the satellite. The temperature distribution is then directly deduced from this.

4.1.1 Solar flux

As there is a very long distance from the Sun, its rays can be considered as parallels. Moreover, there is no reflection taken into account between external faces due to the simple geometry of Cubesats. The solar flux $q_{S,i}$ [W/m^2] of each face i is computed by:

$$q_{S,i} = S_c(\hat{\mathbf{n}}_i \cdot \hat{\mathbf{r}}_{sun})V \tag{4.1}$$

where S_c is the solar constant, $\hat{\mathbf{n}}_i$ the normal vector of face i, $\hat{\mathbf{r}}_{sun}$ the unit sun vector and V a Boolean value representing the sun visibility at the corresponding time. This is equal to one when the satellite is viewing the Sun, and zero during eclipse. This sun visibility value is obtained with the SIMU-CIC extension from CNES such as the satellite positions and velocities. This is illustrated in Fig. 4.1 for one POL orbit at 2020 March 01. The *red points* show where the satellite is in eclipse, and *blue points* where the Sun is visible from the satellite.

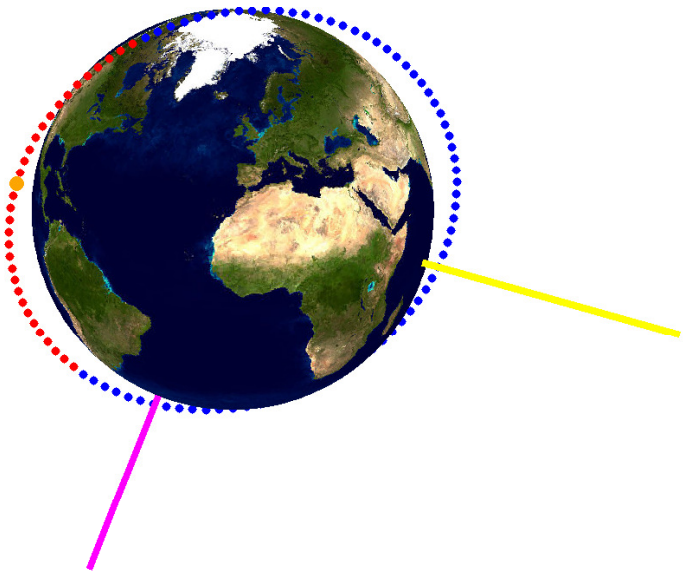

Figure 4.1: Selected polar orbit at 1 mars 2020. yellow: sun, magenta: Proxima, blue: revolution with visibility red: in eclipse, orange point: beginning simulation location.

4.1.2 Albedo flux

The albedo flux is more complex to compute because it depends on many parameters, especially on the Earth view factor. The major problem is that a simple analytic formula does not exist. Moreover, existing tables or expressions to compute the albedo flux are most of the time incomplete or difficult to implement. Therefore, the method used in this study comes from the book *"Spacecraft Thermal Control Handbook"*[41]. The albedo flux $q_{A,i}$ [W/m^2] for each face is given by this formula:

$$q_{A,i} = S_c a \cos^{1.5}(0.9\theta) F_{E,i} \tag{4.2}$$

where a is the albedo coefficient, θ the orbit angle between solar and satellite vectors, $F_{E,i}$ the Earth view factor of each face. The abacus is showed in Fig. 4.2.[41]

However, curves from this abacus are not directly usable for automatic computer computations. This is why an interpolation given by [42] is used:

$$F_{E,i} = r^{2.1} \sin^e\left(\frac{\rho_i}{2}\right) \tag{4.3}$$

where $r = \frac{R_\oplus}{R_\oplus + h}$ (h is the altitude of the satellite) and ρ_i is the angle between the satellite vector and the normal to satellite face i. Finally, e is a parameter find such that:

$$e = -160.31r^6 + 723.36r^5 - 1380r^4 + 1394.6r^3 - 780.65r^2 + 226.81r - 21.232. \tag{4.4}$$

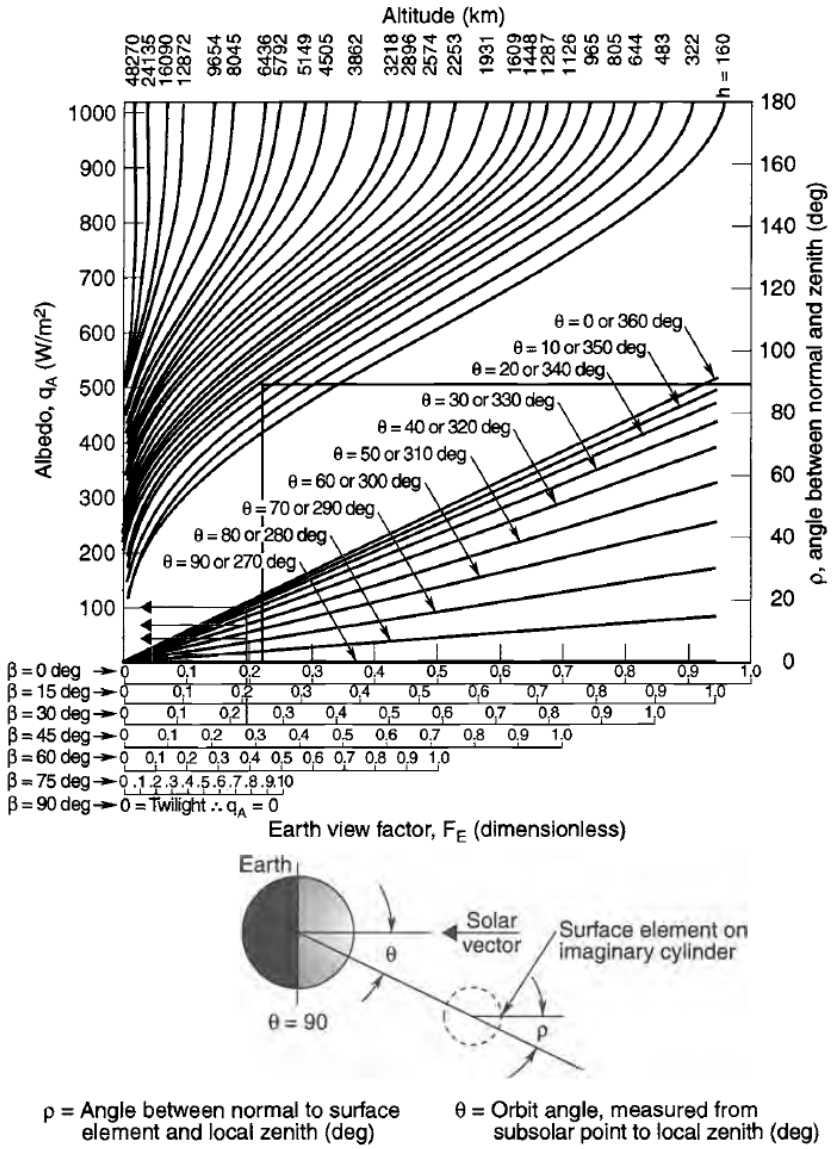

Figure 4.2: Incident albedo irradiation on a surface element in an Earth orbit. (Courtesy of Lockheed Martin.)[41]

Going back on Eq. 4.2, the angle θ is given with a coefficient of 0.9. It allows to better represent the reality. Indeed, once the satellite has passed the terminator line[6] ($\theta = 90°$), it is still receiving albedo radiation from the sunlight part of the Earth. This is the case until reaching $\theta = 100°$. This principle is illustrated in Fig. 4.3.

4.1.3 Earth IR flux

The Earth IR flux is also depending on the same Earth view factor computed just previously. By considering the Earth as a 255 K blackbody while neglecting temperature variations from days and seasons, the i face is receiving the Earth IR

[6]The line that separates day and night

flux computed by:

$$q_{E,i} = E_{bb} F_{E,i} = \sigma T_{E,bb}^4 F_{E,i}. \tag{4.5}$$

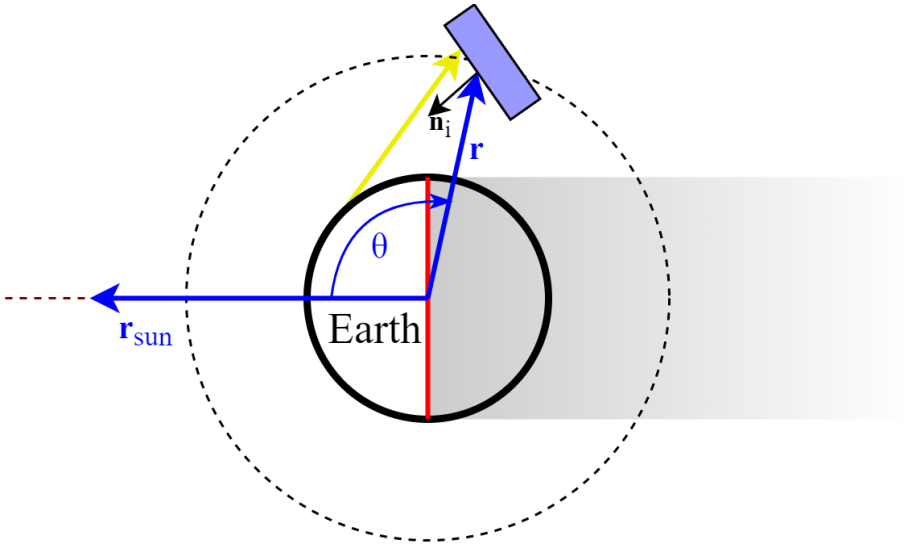

Figure 4.3: Representation of the albedo flux (*yellow arrow*) once the satellite has crossed the terminator line (*red line*).

4.1.4 Results

The numerical results involved by these external thermal loads are presented here for the simplest case. A 1U cubic Cubesat (dimensions: $10 \times 10 \times 10$ cm) which is constantly pointing to Proxima star is then first considered. This 1U geometry allow to conveniently compare the absorbed power of each face with an equal area. Once results of the basic geometry will be introduced, the geometry will directly be adapted to the 12U for the rest of this thesis.

The Cubesat is firstly idealized as a blackbody ($\epsilon = \alpha = 1$). As the objective is to have an average idea on the thermal behavior, the thermal environmental parameters are: a solar constant $S_c = 1367$ [W/m^2], an albedo coefficient of 0.3 [-] and the Earth blackbody temperature of 255 [K]. This is finally orbiting on the selected polar orbit presented in Sec. 3.3.1. Indeed, it was decided to present the study onto one orbit (POL) before comparing with all others. All those parameters are implemented in order to be easily modified in MATLAB. Numerical results for one orbit are displayed from Fig. 4.4 to Fig. 4.9. They are presented for all six faces. The one which is pointing the star is $+X$ (see Sec. 3.1).

First, the absorbed solar power is presented in Fig. 4.4. It shows that power remains constant for the three faces viewed by the Sun. Indeed, as the attitude of the satellite consist to constantly aim a star, view angles of the satellite from Sun perspective are just slightly different days after days. In this configuration, only $-X$, $+Y$ and $+Z$ faces can absorb the direct solar flux. Moreover, as the satellite

is in eclipse before the 18$^{\text{th}}$ minute of simulation and again from the 89$^{\text{th}}$ minute in the orbit($\theta > 0$), none of these faces receives direct power from the Sun. This is then the straight consequence of satellite visibility from the Sun showed in Fig4.1.

The absorbed power due to albedo is displayed in Fig. 4.5. Due to the fact that neither is pointing perfectly away from the Earth, all faces have a view factor which is not null. Then, they are all subject to absorb albedo power.

This graph is more complex to explain because it depends on the two angles θ[7] and ρ[8] for one orbit (see Fig. 4.2). As the satellite is pointing a star rather than the Sun or the Earth, the absorbed albedo power profile is versatile. From this example, the face $-Y$ is absorbing more than others. Indeed, its view factor with the Earth is larger than other faces when flying over the Earth's illuminated part, i.e. where albedo phenomenon takes place.

Moreover, it can be seen that a relay between opposite faces is present. Indeed, as the view factor is depending on ρ_i (then on the orientation of each face) as stated in Eq. 4.3, the maximum value for one face corresponds to the minimum of the opposite face, and conversely. With the addition of θ angle variation on the $+X$ and $-X$ albedo comparison, this is first the $-X$ face which receives more power because its view factor is bigger than the $+X$ one. When the other way around appears, the "relay" takes place to a bigger absorption of $+X$ face.

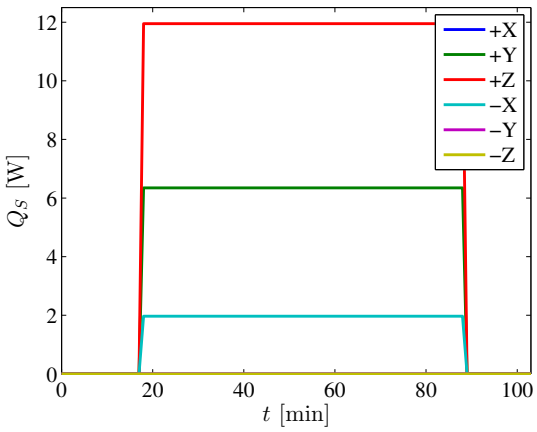

Figure 4.4: Absorbed solar power.

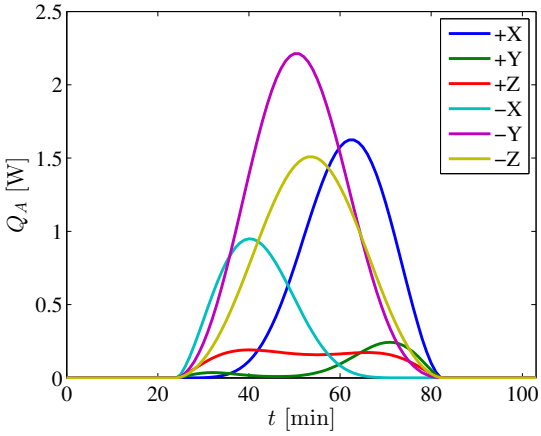

Figure 4.5: Absorbed albedo power.

It can be seen in Fig. 4.6 that absorbed Earth IR power has the same profile for each opposite face. They are shifted by the half period of one orbit. Indeed, when a face is more exposed to the Earth and receives much power from IR, the opposite face does not receive a lot of this type of power. Conversely once located on the other side of the Earth, then after a half orbit time, the behavior is exactly the same for the corresponding opposite face.

However, each face is always absorbing power due to Earth IR, unless its orientation is perfectly away from the Earth. This is also because there is no dependence on illumination, thus no on eclipse but only on the view factor with the Earth.

[7] Angle between Sun vector and satellite vector.

[8] Angle between satellite vector and the satellite's normal for each face.

Results on the total power absorbed by each face due to the three external environmental loads are given in Fig. 4.7. At this step, this is still for a 1U Cubesat considered as a blackbody, pointing Proxima star and orbiting on the selected polar orbit.

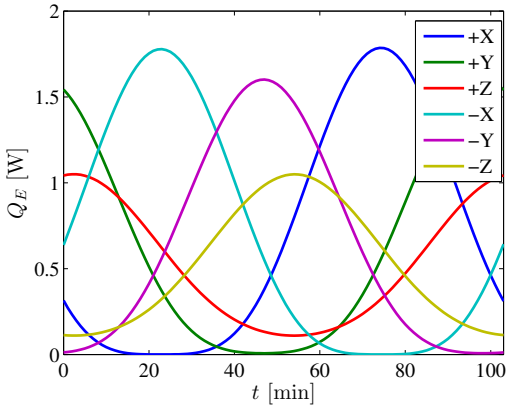

Figure 4.6: Absorbed Earth IR power.

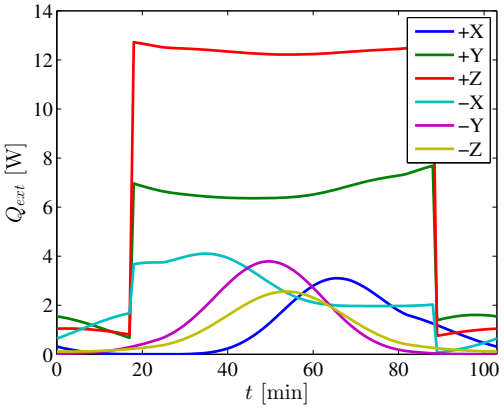

Figure 4.7: Total absorbed power for each face.

Moreover, total results from each external environmental load (solar, albedo and Earth IR) absorbed by all faces of the Cubesat are displayed in Fig. 4.8. Finally, Fig. 4.9 shows the total amount of power absorbed by the entire 1U Cubesat in the actual configuration presented in this section.

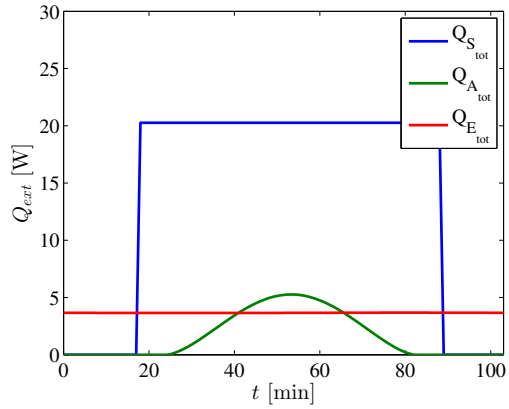

Figure 4.8: Total absorbed power by a 1U Cubesat for each external source.

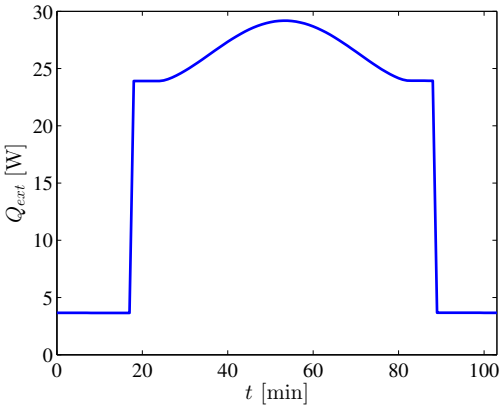

Figure 4.9: Total absorbed power by a 1U Cubesat in selected polar orbit.

The absorbed power profiles are presented for the peculiar polar orbit case. Furthermore, this trend can be generalized for all selected LEOs. Indeed, they are all reacting in the same way than this POL orbit. All absorbed powers are depending on the orientation with the Earth (albedo and Earth IR) or with the Sun (direct solar). In addition, albedo and direct solar fluxes are also depending on the eclipse time.

This is true for all LEOs, but a little different for HEOs and GEO. Actually, a spacecraft following one of these orbits spends most of its time at a high altitude. However, it has been shown in Fig. 4.2 that higher is the altitude, smaller is the Earth view factor. For instance, the maximum Earth view factor is no more that 0.1 [-] at around 13 000 km. According to this figure, it was therefore decided in this work to neglect this view factor and so albedo and Earth IR fluxes for an altitude beyond 25 000 km. Hence, the absorbed power for HEOs ang GEO is mainly governed by the direct solar flux. If the orbit perigee reach an altitude lower than this threshold, albedo and Earth IR will slightly disrupt the total absorbed power distribution at this time.

4.2 Thermal models: Static and cyclic transient

Once all incident fluxes of each face are computed, a first temperature estimate can be calculated for the real 12U geometry. As this is a preliminary analysis, the model has first to be kept very simple: a single node model. As a consequence, the satellite is considered here as isothermal. This single node enables to obtain a first temperature guess of the satellite. In this section, a static and a cyclic transient model are used to obtain a first temperature estimation. This is done by the presentation of the lumped capacitance method and its implementation into MATLAB. A sensitivity analysis onto estimated parameters has finally to be done.

4.2.1 Lumped parameter method

The static and cyclic transient models are based on the lumped parameter method. It consists in a simplification of physical systems into a network made of discrete elements (the nodes). This is done in order to approximate the system behavior under some assumptions. The general form of this method is given by the heat balance on node i, for a system of n nodes:

$$Q_{\text{int},i} + Q_{\text{ext},i} + \sum_{j}^{n} GL_{i,j}\left(T_i - T_j\right) + \sigma \sum_{j}^{n} GR_{i,j}\left(T_i^4 - T_j^4\right) = C_i \frac{dT_i}{dt}. \tag{4.6}$$

In this equation, $Q_{\text{int},i}$ represents the internal dissipated power on node i and $Q_{\text{ext},i}$ is the total external power absorbed by the node (see Fig. 4.7). The parameters $GL_{i,j}$ and $GR_{i,j}$ are respectively the conductive and radiative links presented in Sec. 2.1. Finally, C_i is the thermal capacitance [J/K] of the node i and T_i its temperature [K]. When the satellite is considered as a single node model, the equation becomes:

$$Q_{\text{int}} + Q_{\text{ext}} + \sigma GR_{\text{sat,DS}}\left(T_{\text{sat}}^4 - T_{\text{DS}}^4\right) = C\frac{dT_{\text{sat}}}{dt} \tag{4.7}$$

where Q_{ext} is the total external power absorbed by the entire satellite since it is represented by only one node like in Fig. 4.9. Thereafter, $GR_{\text{sat,DS}}$ is the radiative link between the satellite and the Deep Space ($T_{DS} = 3$ K). Due to the absence

of coupling between faces in a single node system, $GR_{\text{sat,DS}}$ is computed with the equivalent emissivity:

$$GR_{\text{sat,DS}} = A_{tot}\epsilon_{eq} = A_{tot}\sum_{i}^{faces}\frac{A_i\epsilon_i}{A_i}.$$

The first presented model is the static thermal one. It does not depend on time, then the right hand side of the Eq. 4.7 is set to zero. This is mainly used here to obtain the first guess on initial temperature. It will be used for the next model: the cyclic transient method. This model takes into account this right hand side of Eq. 4.7. This process of the cyclic transient method is presented by the flowchart in Fig. 4.10. The cyclic term means the integration of this Eq. 4.7 over one complete orbital period for several times. This cycle considers that the state of satellite has to be the same after one orbit than at the beginning. Then, there will be as many iterations as necessary until reach a predefined tolerance, which represents the convergence limit.

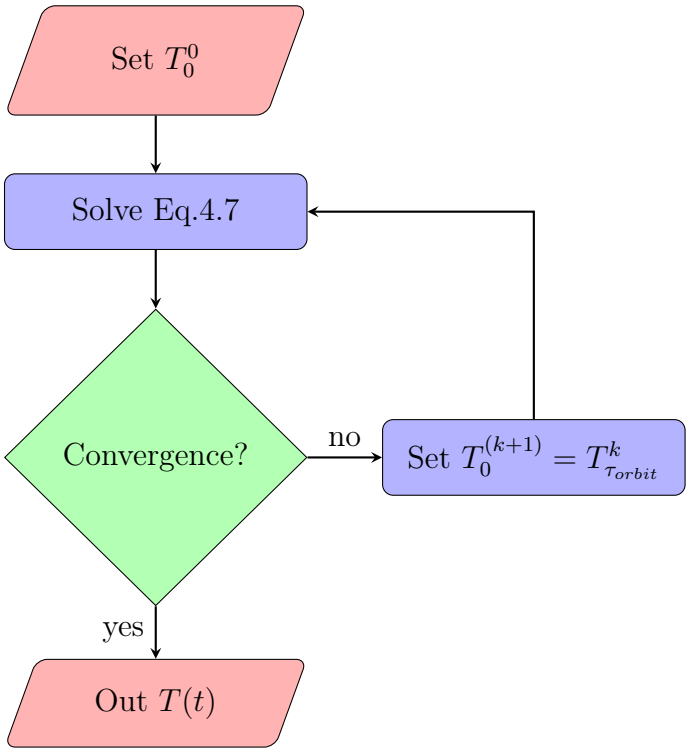

Figure 4.10: Flowchart of cyclic transient model.

This method is generally used for low Earth orbits because their orbital period (τ_{orbit}) is quite short compared to the variational time of the Sun position in Earth reference. Therefore, conditions has to be less rigorous for orbits with long orbital period like SMI or even XMM. Indeed, their orbital period lasts more than one day. As the Sun position is actualized every 24h, they are not in the same configuration than in the beginning after one complete revolution. Hence, criteria of convergence are given here below.

- Temperature reached at the end of the orbital period τ_{orbit} must be the same than temperature at the beginning of this same orbit:

$$\|T(t+\tau_{orbit}) - T(t)\| < tol_T{}^9.$$

- Temperature variation over time at the end of the orbital period τ_{orbit} must be the same than the one at the beginning of this same orbit:

$$\left\| \left.\frac{dT}{dt}\right|_{t+\tau_{\mathrm{orbit}}} - \left.\frac{dT}{dt}\right|_{t} \right\| < tol_{dT}.$$

The first guess on temperature is given by the static model. Then, the cyclic transient equation for one node is solved. If one criteria of convergence is not respected, a new iteration is done. Therefore, the new initial temperature is equal to the last temperature of the previous iteration. Once convergence is reached, the process stops to iterate and the final output temperature distribution is kept.

This can finally be implemented in MATLAB. The non-linear differential equation (Eq. 4.7) is solved with the Runge-Kutta algorithm using `ode` function.[43] This function is using its own time distribution. However, the external power Q_{ext} is given for every minute. Hence, Q_{ext} has to be interpolated in order to be known at each time and no more being only discrete values. The lumped parameter equation can then be solved.

4.2.2 Implementation

As the flowchart is implemented into MATLAB solver, other parameters have also to be chosen. From now, the study is made for the actual geometry of the satellite: the 12U configuration (see Fig. 3.1). Parameters representing external loads (solar, albedo and Earth IR) are still those average of previous section. However, the satellite is not considered anymore as a blackbody.

This interferometric small sat project is at its very beginning. This thesis is the first study on thermal attitude of the satellite. This is good to keep in mind that the objective is to have a first idea of thermal behavior for such a satellite. Therefore, components parts are not yet selected. This is why surfaces values which are necessary for the implementation are approximated from others Cubesats. This is especially first estimated by the analogy with total external surface area and parameters from OUFTI missions.[44],[42] Hence, emissivity and absorptivity of satellite surfaces are assumed to be equal to 0.85 [-].

For both static and cyclic transient case, the total external power due to environmental thermal loads is the same. By analogy with Fig. 4.7 and Fig. 4.9 from previous section, the actual external power acting on the 12U satellite is presented in Fig. 4.11 and Fig. 4.12 for one orbit. The selected orbit is still the polar orbit from Tab. 3.2 at 896 km altitude.

[9] Computed between the temperature variation happening over one minute (the time step).

As the geometry has changed, the peculiarity of the new one is that extremity faces $+Y$ and $-Y$ (see Fig. 3.1) have a twelve times smaller surface area than other faces. The external power distribution profile is therefore not symmetric anymore. Indeed, the equivalent surface area is different when the cubic configuration (1U) is changed.

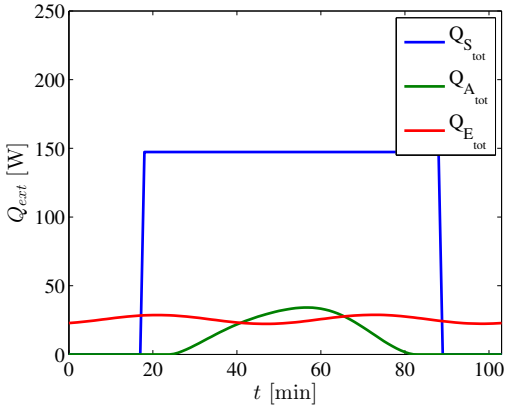

Figure 4.11: Total absorbed power by a 12U Cubesat for each external source for a peculiar POL orbit at 896 km, pointing Proxima star, average thermal case.

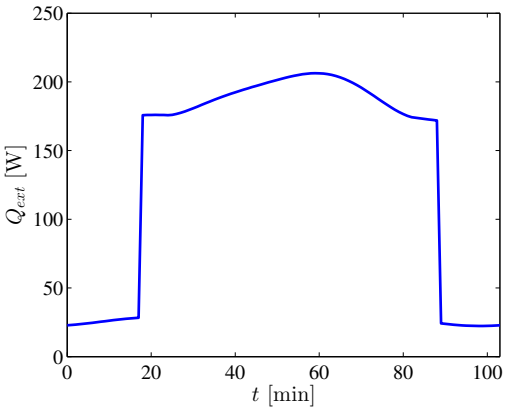

Figure 4.12: Total absorbed power by a 12U Cubesat for a peculiar polar orbit at 896 km, pointing Proxima star, average thermal case.

4.2.3 Static results

The static results are obtained by solving Eq. 4.7 while removing the right hand side. In that case, the only varying parameter is Q_{ext}. Hence, the temperature distribution has exactly the same profile than Q_{ext} which is presented in Fig. 4.12 for one orbital period. The relevant values from this solver are: the minimum temperature happening during eclipse, the maximum temperature appearing in the peak sunlight and finally the mean temperature observed for one complete orbital period. These values are given in Tab. 4.1. As this is a static case which does not take into account satellite temperatures from previous time step, this gives a too wide range of temperature for this peculiar polar orbit compared to real expected values.

Case	Temperature [K]
Minimum: eclipse	174
Mean: one complete orbit	260
Maximum: sunlight	304

Table 4.1: Relevant static temperatures observed for one complete polar revolution at 896 km altitude, pointing Proxima star, average thermal case.

4.2.4 Cyclic transient results

When the right hand side of Eq. 4.7 is taken into account, this is the cyclic transient thermal model. Therefore, the thermal capacitance C has to be approximated. As for emissivity and absorptivity assumptions, this is done by analogy with previous projects (OUFTI).[42] For example, in OUFTI-Next mission[44], the capacitance is equal to 3096.2 J/K for the 3.02 kg Cubesat (3U). As this is a direct consequence of satellite's mass, it is first considered in this project to have a capacitance of 1000 J/K per unit. Consequently, for a 12U geometry considered here, the first capacitance is first guessed to be around 12 000 J/K.

The flowchart of Fig. 4.10 is afterwards used in MATLAB. The initial considered temperature is equal to the mean value from the same orbit given by the static solver. The cycle of convergence is then launched. As relevant temperature results are given with an accuracy of 1°, a tolerance value of 0.1° is therefore acceptable.

The temperature distribution along the orbit is finally represented in Fig. 4.13 for the static and cyclic transient cases. The satellite is reminded to be isothermal, with parameters $\alpha = \epsilon = 0.85$ [-] and $C = 12\,000$ J/K. As expected, the temperature is obviously decreasing during eclipse time, and is increasing during sunlight period.

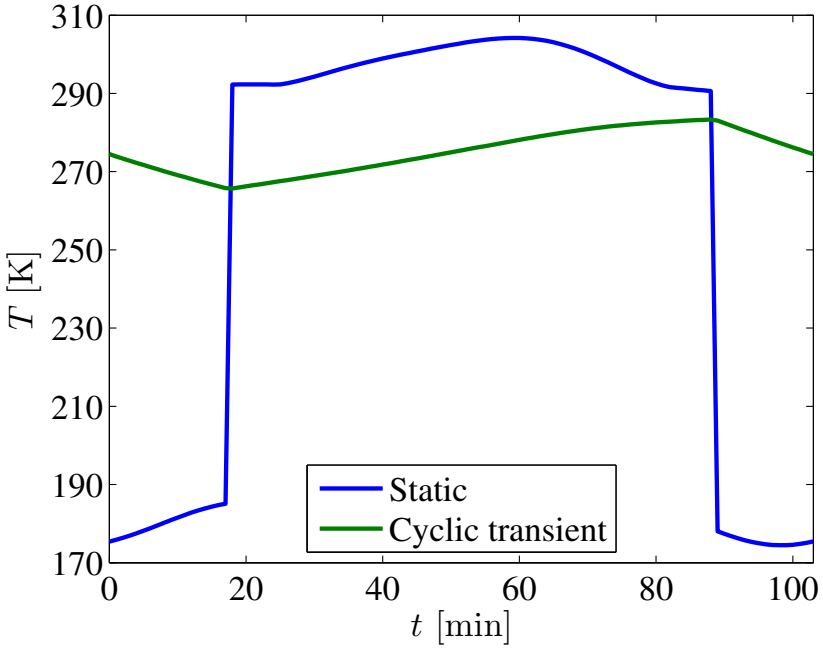

Figure 4.13: Temperature distribution for static and cyclic transient model for a peculiar POL orbit at 896 km, Proxima star, average thermal case.

This figure shows clearly that the temperature distribution of the cyclic transient model is included between the minimum and maximum temperature provided by the static model. Moreover, the temperature due to cyclic transient case is well decreasing when the static temperature is low, and conversely as expected. This is

directly governed by the Sun power, depending on the condition if the satellite is in eclipse or not.

4.2.5 Sensitivity analysis

Values on emissivity, absorptivity and capacitance parameters are stated. However, this is important to be aware of their influence onto temperature results. This sensitivity analysis is represented in the Fig. 4.14. The emissivity and absorptivity are still first considered as equal. In this analysis, they are made varying from 0.75 [-] to 0.95 [-] while the capacitance parameter is varying from 10 000 J/K to 14 J/K.

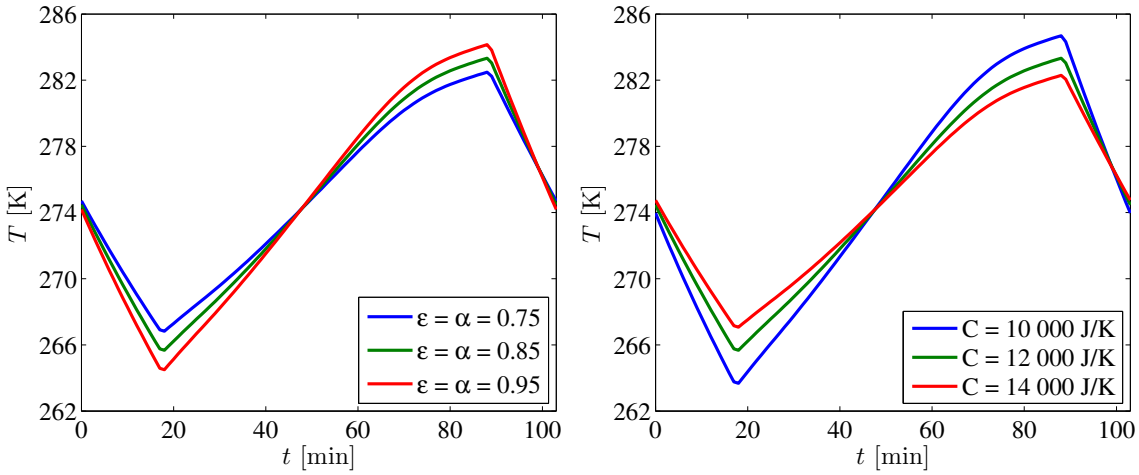

(a) Emissivity and absorptivity variation. **(b)** Capacitance variation.

Figure 4.14: Cyclic transient temperature for the 12U satellite on the peculiar POL orbit with various parameters.

These two figures show that higher the emissivity, higher the temperature distribution amplitude. Indeed, more the emissivity and absorptivity are close to the unit, more it acts as a blackbody. In this case, the maximum temperature has increased of almost 2 K from $\epsilon = 0.75$ [-] to $\epsilon = 0.95$ [-] while the selected value of 0.85 [-] is located between them. The capacitance parameter is equal to 12 000 J/K. After a value change of approximately 17% in both directions, the temperature changes by only 2 K maximum. Actually, the temperature distribution is flattening with a capacitance increase. This is due to the larger thermal inertia of the satellite.

4.3 Results

Results are currently presented for the specific POL orbit while pointing to Proxima star. However, the objective of this work is to study the influence when pointing to all five selected stars, but also for all the different chosen orbits.

4.3.1 Different stars

This project has then to study the case of pointing to the five selected stars. The satellite orientation is therefore changed, because the $+X$ face has to be always pointing to the star. Hence, for the same orbit used in previous section, the Fig. 4.15 represents the temperature distribution given by cyclic transient thermal model in each star case.

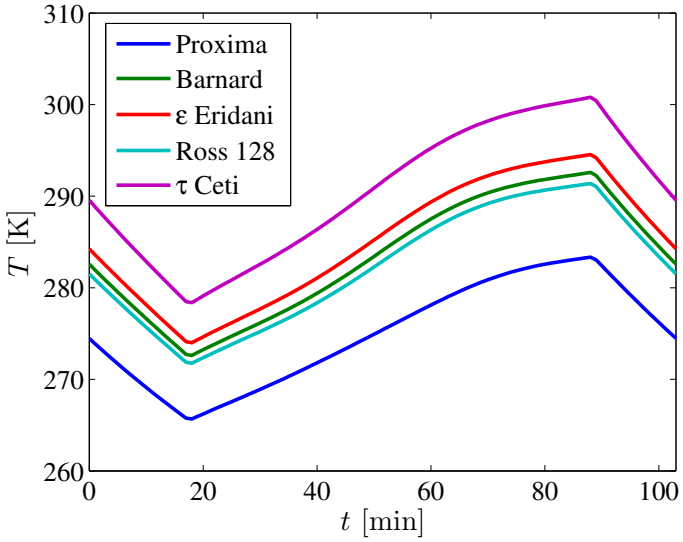

Figure 4.15: Temperature distribution over one orbit for each star for a peculiar POL orbit at 896 km.

The five distributions have the same profile. However, the maximal amplitude is different in each case. Actually, a same orbital plane involves a same temperature distribution profile but a different star direction with respect to the Earth leads to a various maximum temperature. The direction of the five stars and the Sun are illustrated in Fig. 4.16. The used orbit is also displayed in this figure.

In fact, the amplitude variation can be explain by the effective area which is changing for the five cases. This effective area A_{eff} can be defined as the ratio of received power compared to the nominal power incident to a unit surface. It is calculated for a satellite with n faces by:

$$A_{eff} = \frac{1}{q_{nom}} \sum_{i}^{n_{faces}} A_i q_i. \tag{4.8}$$

As seen previously in Fig. 4.11, the total absorbed power is mainly due to direct solar loads. Then, effective areas for each star pointing case are presented in Tab. 4.2. This is good to remind that the face $+X$ is pointing the star, with a surface area (1200 cm^2) twelve times bigger than faces $+Y$ and $-Y$ (100 cm^2) in the 12U configuration. This is why in this case, pointing Tau Ceti star has the higher temperature distribution, as the direction of Tau Ceti is the closest to Sun's direction.

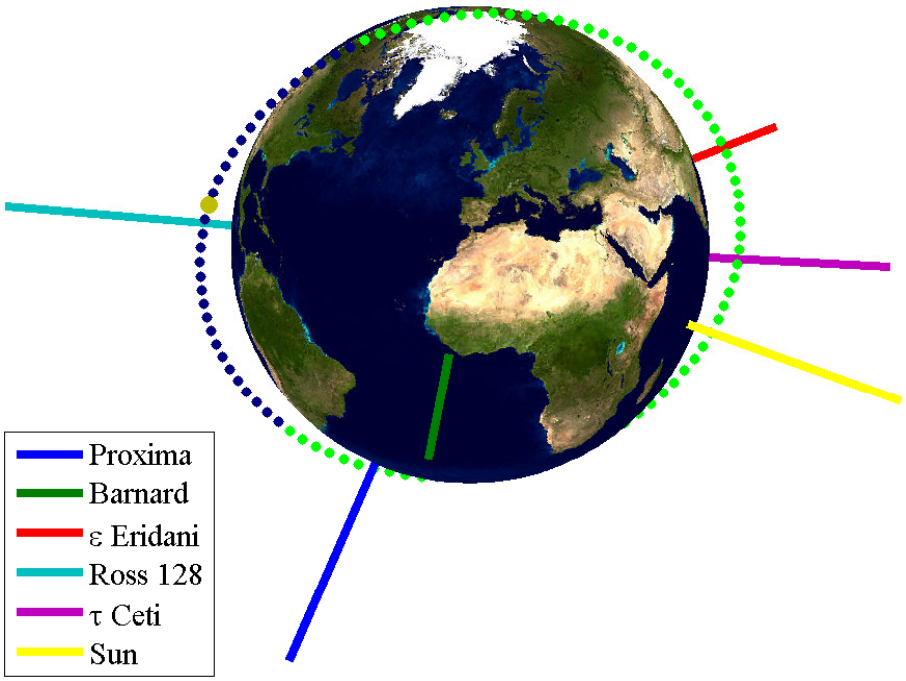

Figure 4.16: Stars and Sun directions from the Earth for a peculiar POL orbit at 896 km. Green points when the satellite orbiting is visible from the Sun, dark blue otherwise. The orange point is the satellite's position at the beginning of simulation. Its first direction is going to the South pole.

Pointing star	Effective area [cm^2]	Effective area [%]
Proxima	1 268	100
Barnard's star	1 493	118
Epsilon Eridani	1 541	122
Ross 128	1 464	115
Tau Ceti	1 697	134

Table 4.2: Effective areas for each star pointing case computed with nominal direct solar power.

Those values are finally correctly describing the main cause of maximum amplitude variance observed in Fig. 4.15.

4.3.2 Different orbits

Furthermore, another objective is to study the thermal behavior for all selected orbits presented in Tab. 3.1. That is why the temperature distributions are given in Fig. 4.17 for all LEO, and in Fig. 4.20 for all HEO and GEO. The actual pointed star is Proxima.

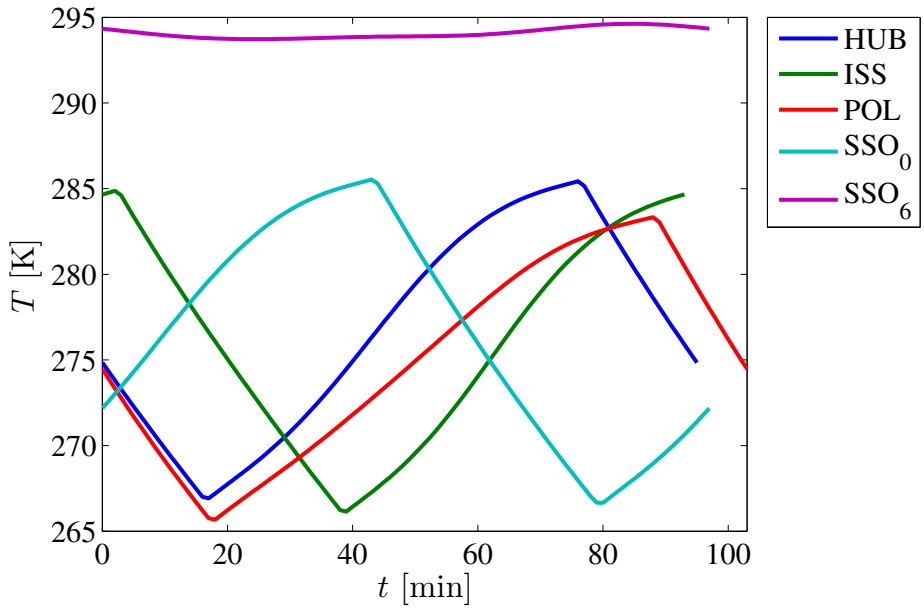

Figure 4.17: Temperature distribution over one orbit for each selected LEOs. Pointed star is Proxima.

In the Fig. 4.17, all decreased temperatures for each orbit correspond to their own eclipse time, besides SSO with 06h00 LTAN[10] which has no eclipse time. Then for other orbits, the range of temperatures remains quite similar. However, small variations of amplitude are observed.

It can mainly be explained by the variation of effective area ratio due to the position of satellite with respect to the Sun vector from one orbit to another (as explain previously for Fig. 4.15). Moreover, the altitude has also a role in the maximum temperature. This is shown in Fig. 4.18 and Fig. 4.19 than higher is the altitude, lower is the amount of absorbed power. As a consequence, a high altitude involves a smaller maximum temperature. Nevertheless, this difference is not significant since the mean difference is about 2 K less from 400 km to 800 km.

[10]For SSO, a LTAN of 06h00 is the same than 18h00. This is the same for all LTAN shifted by 12h.

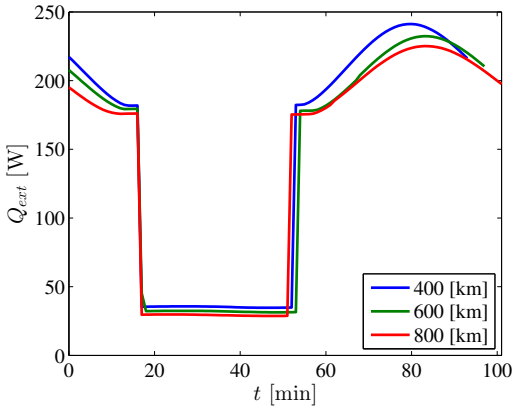

Figure 4.18: Total absorbed power by a 12U Cubesat for different altitudes in SSO, 00h00 LTAN.

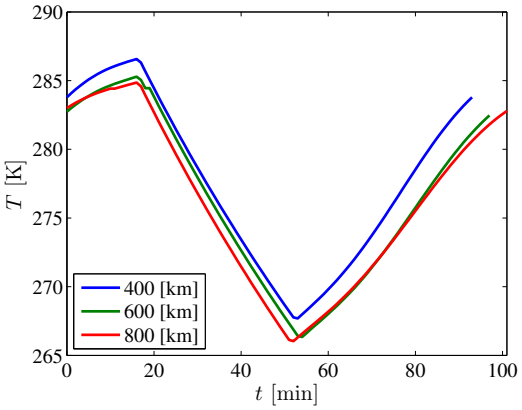

Figure 4.19: Temperature of a 12U Cubesat for different altitudes in SSO, 00h00 LTAN.

The Fig. 4.20 presents the temperature distribution for all HEOs and GEO over one orbit. Every profile is computed over one orbital period at a date where there is no eclipse time because this is a main advantage of this kind of orbits compared to the LEOs. The chosen time range in abscissa axis is governed by the longest orbital period: SMILE (54h orbital period).

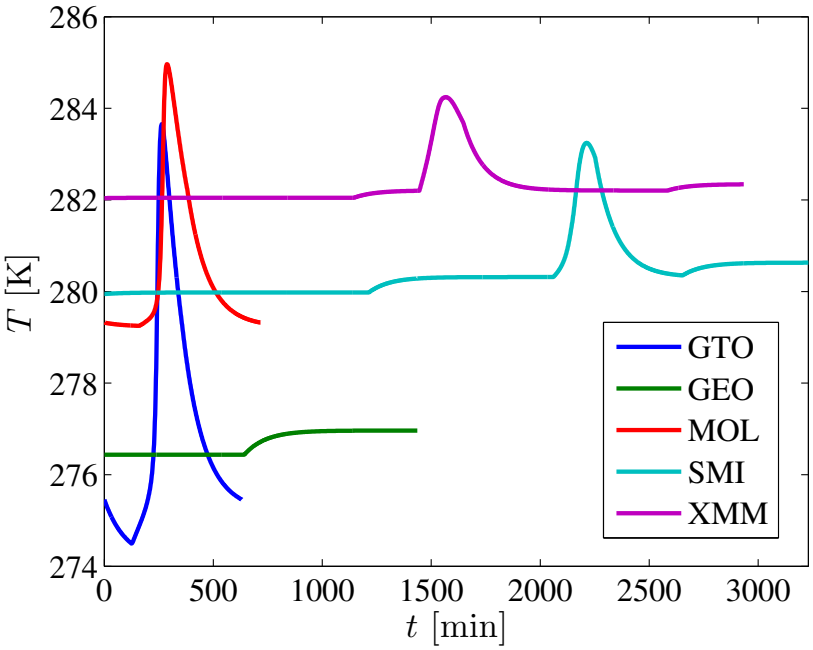

Figure 4.20: Temperature distribution over one orbit for each selected HEOs and GEO. Pointed star is Proxima.

Then without eclipse, the temperature range of each HEO and GEO is highly smaller and much more stable than LEOs. Actually, this range between the maximum and minimum temperature over one complete orbital period is about almost 20° for LEOs besides 00h00 LTAN SSO, while it is between 0.5° and 9° for GEO

and HEOs. This is because the absorbed power variation is way less important than in low Earth orbits. Indeed, this is mainly governed by the Sun loads because altitude is here much higher and so thermal loads from the Earth are most of the time neglected. Moreover, the small jumps in value observed in Fig. 4.20 are a direct consequence of the direct Sun thermal load, which is approximated to be equal for a day, and then approximated again the next day.

This preliminary thermal analysis gives a first guess on thermal behavior for each selected orbits. However, as the satellite is here considered as isothermal, this is actually impossible to know the behavior of different faces. Furthermore, the two optical sub-pupils allowing to gather the exoplanet light are located at both extremities. Hence a more detailed model is needed.

Chapter 5

Advanced thermal model adapted on orbital situation

In this chapter, an advanced thermal model of the 12U satellite is introduced: the multi-nodes model. This allows to obtain the temperature at each individual node, which was not possible with the previous single node model. Moreover, as the temperature can be known at several locations, gradients between nodes can also be calculated.

This chapter will begin by the multi-nodes thermal modeling applied on the 12U linear satellite. Then, the satellite rotation needed by the interferometry process to modulate planetary signal (see Sec. 1.2.2) is implemented in the simulation. Next, variations happening over the year are discussed. After that, the elongation computation process is presented and results from a peculiar orbit are summed up. Finally, the extreme elongation range computation is explained and calculated.

In summary, temperatures and elongations are computed and explained in this chapter. For this purpose, it has to be applied to an orbit. Then, it has been agreed to present computations for the peculiar polar orbit in order to make a convenient analysis before considering and compare all other orbits.

It was decided to put a node in the center of each face, so six nodes in total. In order to respect the notations of all faces presented in Sec. 3.1 and Fig. 3.1 for the 12U linear satellite, nodes are quoted as:

- $1 = +X$
- $2 = +Y$
- $3 = +Z$
- $4 = -X$
- $5 = -Y$
- $6 = -Z$

5.1 Thermal modeling of the six nodes 12U satellite

The method is also based on the lumped parameter method represented by the Eq. 4.6. All nodes (then all faces) are considered as isothermal in a thermal network.

This analysis is performed in two stages: the geometric mathematical model (GMM) and the thermal mathematical model (TMM). The temperature distribution of the six nodes model is finally computed.

5.1.1 Geometric mathematical model

The GMM allows to compute radiative coupling between nodes and heating rates from environment thermal fluxes. Equivalent radiative links are computed by:

$$GR_{i,j} = \frac{1}{\frac{1-\epsilon_i}{A_i\epsilon_i} + (A_i F_{i,j})^{-1} + \frac{i-\epsilon_j}{\epsilon_j A_j}} \tag{5.1}$$

with $F_{i,j}$ the view factor of node i to j. They are computed for the 12U geometry of the satellite. The method used to estimate them comes from *"Fundamentals of Heat and Mass Transfer"* by F.Incropera et al.[27]. The 3D view factor computation processes are given with their corresponding equation in the appendix. This is in the Fig. 20 for two aligned parallel rectangles and in Fig. 21 for two perpendicular rectangles with a common edge.

Then, for the 12U geometry satellite, the obtained $(i \times j)$ matrix of view factors F from node i to j is:

$$F = \begin{pmatrix} 0 & 0.021 & 0.284 & 0.391 & 0.021 & 0.284 \\ 0.249 & 0 & 0.249 & 0.249 & 0.002 & 0.249 \\ 0.284 & 0.021 & 0 & 0.284 & 0.021 & 0.391 \\ 0.391 & 0.021 & 0.284 & 0 & 0.021 & 0.284 \\ 0.249 & 0.002 & 0.249 & 0.249 & 0 & 0.249 \\ 0.284 & 0.021 & 0.391 & 0.284 & 0.021 & 0 \end{pmatrix}$$

This view factor matrix between faces i and j is respecting the Eq. 2.10 which states that the sum of all view factors from a same face i is equal to the unit. Indeed, the sum of each line of F matrix is equal to one. This matrix is not symmetric since all faces of the 12U satellite do not have the same surface area.

5.1.2 Thermal mathematical method

The TMM gives the conductive links and the heat capacity. The temperatures at different nodes of the spacecraft can be then predicted. Equivalent conductive links are computed by:

$$GL_{i,j} = \frac{kA_c}{L} \tag{5.2}$$

with k the material conductivity [W/m·K], A_c the cross section area [m^2] and L the length [m] separating nodes i and j.

The satellite is first considered to be covered by an entire shear panel which supports solar cells. The chosen material is the *Aluminium 6061*. The thickness is first considered to be 1 mm.[45] Its conductivity is $k_{Al6061} = 180$ W/m·K.[41] With this consideration, all $GL_{i,j}$ are assembled in a $(i \times j)$ matrix GL representing all conductive links from node i to node j:

$$GL = \begin{pmatrix} 0 & 0.0277 & 2.1600 & 0 & 0.0277 & 2.1600 \\ 0.0277 & 0 & 0.0277 & 0.0277 & 0 & 0.0277 \\ 2.1600 & 0.0277 & 0 & 2.1600 & 0.0277 & 0 \\ 0 & 0.0277 & 2.1600 & 0 & 0.0277 & 2.1600 \\ 0.0277 & 0 & 0.0277 & 0.0277 & 0 & 0.0277 \\ 2.1600 & 0.0277 & 0 & 2.1600 & 0.0277 & 0 \end{pmatrix} W/K$$

Once all values are known, the lumped capacitance equation (Eq. 4.6) can be solved by its implementation in MATLAB. Compared to the single node case, it is not anymore one but the six absorbed external power Q_{ext} (one for each node) which has to be interpolated in the `ode` function based on the Runge-Kutta method.[43] The temperature distribution can finally be computed for each face.

5.1.3 Temperature results

Under this six nodes thermal model, the temperature distribution at each node can therefore be computed. For the selected polar orbit case, the temperature over one orbital period is given in Fig. 5.1. The pointed star is currently Proxima. This figure is also displaying the temperature distribution obtained for the basic single node thermal model.

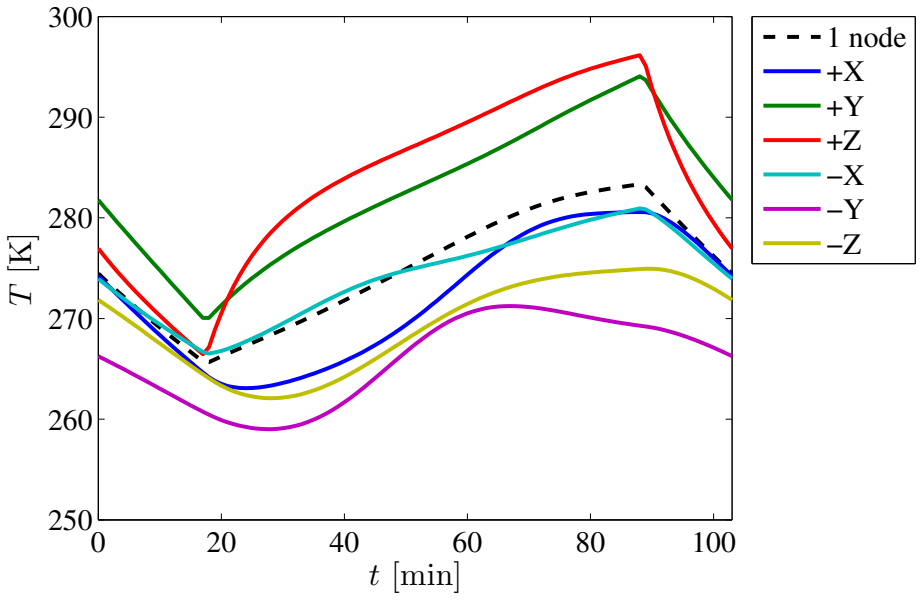

Figure 5.1: Temperature distribution comparison between one node and six nodes for selected polar orbit at 896 km altitude, pointing Proxima star and for the average thermal case.

As expected from Fig. 4.13, the temperature range is close to the first temperature approximation obtained by the single node temperature distribution. The one node model is in fact computing the mean temperature of all faces. All of them are approximately following this single node distribution, with a slightly different amplitude explained by the satellite orientation according to the Sun.

5.2 Rotational case

At this stage, results can be obtained for a static satellite case. However, as explained in Sec. 1.2.2, the satellite has to spin around itself due to interferometry process needs. This rotation is made around the axis which is pointing to the star ($+X$). It allows the signal to be modulated, thus to detect exoplanets. The rotation is first described, then temperature distributions can be computed before the analysis of temperature variations.

5.2.1 Rotation description

A radiometric study have stated that the ideal integration time is 24h. Longer the integration time, larger the amount of received photons. However, increase this 24h integration will induce strong constraints on the attitude control of the satellite. In addition, below this 24h value, the obtained Signal-To-Noise ration (SNR) is too weak and so an exoplanet detection will be unlikely.[11] Furthermore, the rotation allow the planet signal to be modulated. Therefore, by rotating an integer number of time over the integration duration, it provides the same number of modulated period. This is why it was decided to study cases with a spinning period of 3, 6, 12 and 24 hours. The rotation is presented in Fig. 5.2 for one polar revolution according to Proxima star point of view. The satellite is represented by *green* and *cyan lines* as it is split in two equal parts. This point of view allows to understand the rotation around the normal to $+X$ face which is pointing the star.

However, the convergence conditions computed after each orbital revolution presented in Sec. 4.2.1 are no more valid. Indeed, the satellite cannot be considered to be in the same configuration before and after one complete revolution because it has in addition to spin also around the normal to $+X$ face. The only possibility is to have a rotating period around normal to $+X$ face equals to the orbital period. But this is not applicable since this time is not an integer divider of the 24h integration time.

Hence, the used method is to take initial temperatures obtained previously when the satellite was not spinning around itself. Furthermore, as the profile is no more periodic, the calculation period has to be much longer than one single orbital period. It has to be at least as long as the time of one complete spin. Finally, in order to avoid the convergence problems due to the spin, temperatures are computed over several orbital periods, and only temperatures from last periods are retained.

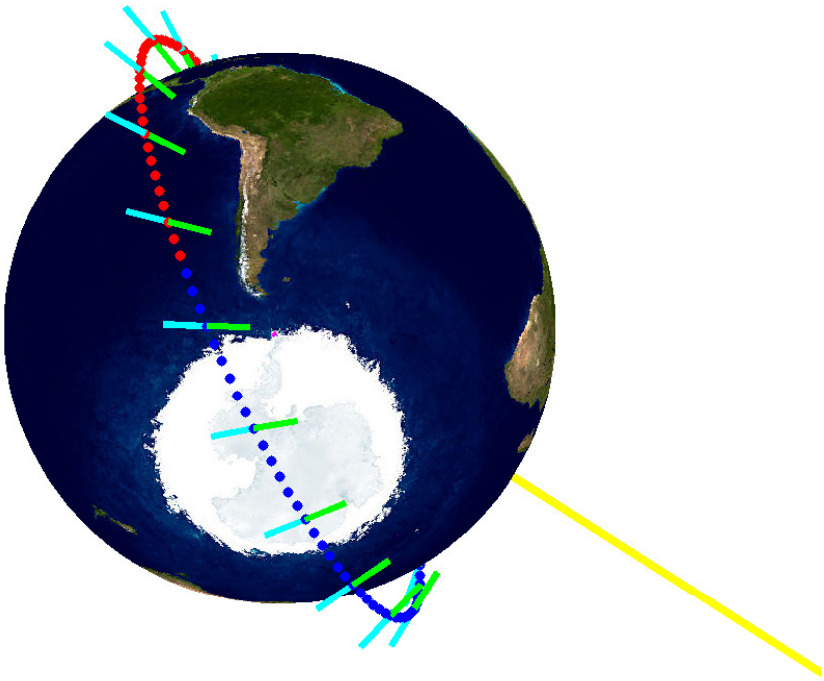

Figure 5.2: Satellite rotation around normal to $+X$ face from Proxima star point of view. Polar orbit 896 km, 3h period for one complete spin. *Yellow line* is the Sun direction, *blue* and *red points* are respectively the orbit trajectory when it is visible and no visible from the Sun. *Green* and *cyan lines* are the two split parts of the satellite.

5.2.2 Temperature distributions and variations

The temperature distributions of the four different spinning periods are shown in Fig. 5.3. This is displayed only over a single orbital revolution because the goal is here to compare behavior with the no spin case presented in Fig. 5.1.

Obviously, slower the satellite rotation is, more similar to the no spin case the temperature distribution is. However, there is much more variations when the spinning period is short. A relevant observation can be done on the temperature variation over time. The absolute mean temperature variations are summed up in the Tab. 5.1 for each face and each spinning period. All temperature variations are computed between two discrete temperatures separated by the time step (60s) of the simulation over the orbital period. Absolute values allow here to understand the variation rate of each spinning case. These values are given over an entire day time simulation in order to respect the time condition given in the previous paragraph.

From this Tab. 5.1, temperature variation on opposite faces $+X$ and $-X$ does not change much compared to other faces. Indeed, $+X$ is pointing to the star. And since the rotation is made around the normal to these faces, their effective area computed with external environmental loads remains constant. The only small variation is due to interactions with others faces.

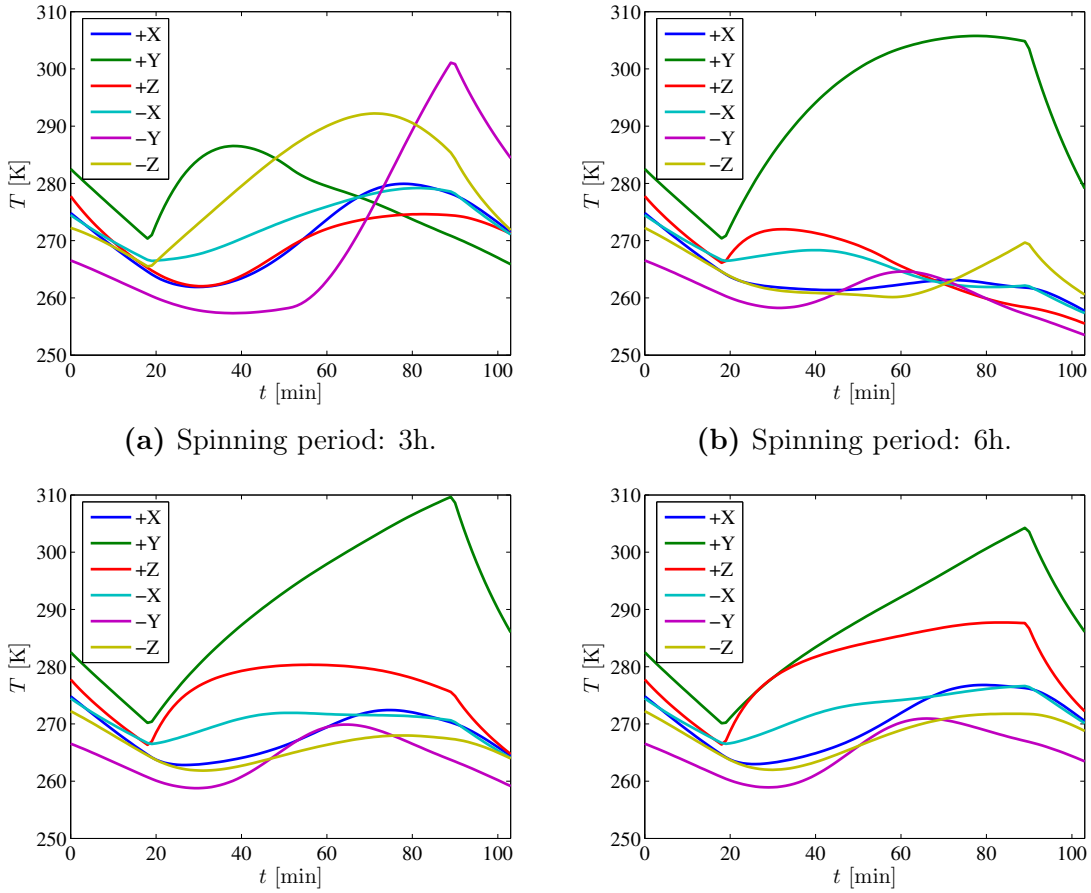

(a) Spinning period: 3h.

(b) Spinning period: 6h.

(c) Spinning period: 12h.

(d) Spinning period: 24h.

Figure 5.3: Temperature distribution for selected polar orbit when satellite is rotating around the normal to $+X$ for different selected spinning periods. 896 [km] altitude, Proxima star, average thermal case.

$\lvert\dot{\boldsymbol{T}}\rvert_{\text{mean}}$	Face $+X$	Face $+Y$	Face $+Z$	Face $-X$	Face $-Y$	Face $-Z$
3h spin	0.32	0.55	0.42	0.26	0.55	0.42
6h spin	0.32	0.46	0.38	0.26	0.47	0.38
12h spin	0.32	0.44	0.35	0.25	0.42	0.37
24h spin	0.31	0.42	0.34	0.24	0.42	0.34
No spin	0.34	0.47	0.58	0.28	0.24	0.25

Table 5.1: Absolute mean temperature variation over time [K/min] of each face for all selected spinning periods. POL orbit, one day simulation, Proxima pointing.

Furthermore, as stated above, the mean temperature variation is increasing with a faster rotation due to the fact that the satellite is more in motion. In addition to this, the Tab. 5.2 presents the maximum temperature variation in one minute (time step duration) for each face and all selected spinning periods.

$\dot{\boldsymbol{T}}_{\max}$	Face $+X$	Face $+Y$	Face $+Z$	Face $-X$	Face $-Y$	Face $-Z$
3h spin	0.73	2.23	2.08	0.64	2.33	2.16
6h spin	0.73	2.44	2.25	0.59	2.54	2.19
12h spin	0.73	2.30	2.24	0.53	2.64	2.25
24h spin	0.69	2.57	2.33	0.55	2.57	2.34
No spin	0.60	1.02	2.14	0.53	0.53	0.45

Table 5.2: Maximum temperature variation over time [K/min] of each face for all selected spinning periods. POL orbit, one day simulation, Proxima pointing.

From those two tables, it can be stated that spinning around itself increases the maximum temperature variation. Moreover, the period for one complete rotation around $+X$ axis is just acting on the mean variation. Smaller the period is, faster the rotation speed will be, and therefore more varying the temperature of a face will be too.

5.3 Variations over the year

At this point of the study, simulations are studied mainly over one single orbital period, or for maximum one day. However, there is often much more variations observed over one year. This is why it is useful to study the selected orbits behaviors on a whole year. For this purpose, the β angle is introduced. Then, the corresponding temperature distributions are presented without any spin around $+X$ normal axis. This is next justified for the static satellite case. It is finally presented the satellite rotation consequence over the year onto satellite environment.

5.3.1 β angle variation

A relevant parameter allowing to expand the study over one year is the β angle. This is the angle between the Sun vector and its projection onto the orbital plane. Basically, this angle definition is depicted in Fig. 5.4[11]. The β angle is presented in Fig. 5.5 for the POL orbit example from 2020 January 01 to 2020 December 31.

From this table, there are four meaningful values which have to be studied. The two firsts are when β angle distribution is reaching its maximum and minimum value. Others are when it crosses the null value: $\beta = 0°$.

[11]This is the concept of β angle which is presented in the figure, not the β angle of selected POL orbit.

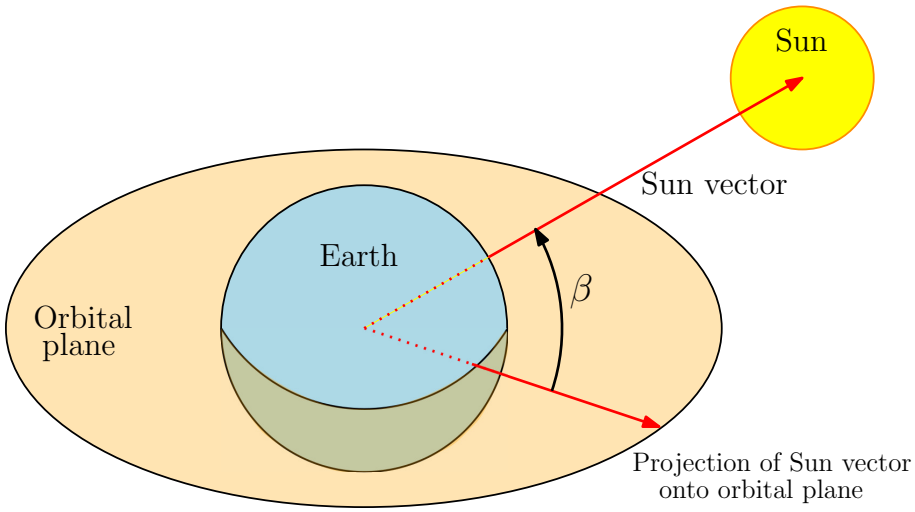

Figure 5.4: Angle between the Sun vector and its projection onto the orbital plane. It is commonly known as "beta angle".

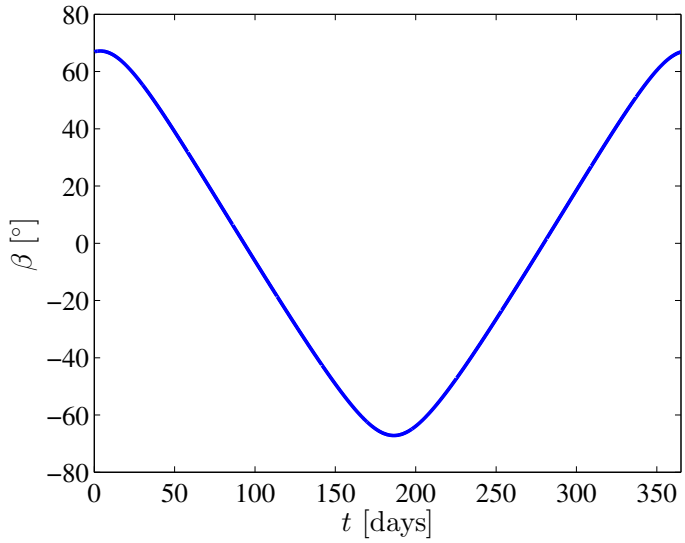

Figure 5.5: Beta angle over 2020 year. POL orbit.

As this happens two times a year, they are differentiate by the β angle variation: while decreasing and while increasing. The lumped parameter equation has then to be solved for orbits when all those singular angles are encountered.

The dates corresponding to singular β angle values are then:

- β is maximum (67.18°) at January 04 18:26.
- $\beta = 0°$ at April 02 03:50.
- β is minimum (-67.18°) at July 04 10:27.
- $\beta = 0°$ at October 05 16:06.

All dates are approximately separated by a quarter year. The temperature distribution on each date are given in Fig. 5.6 and Fig. 5.7.

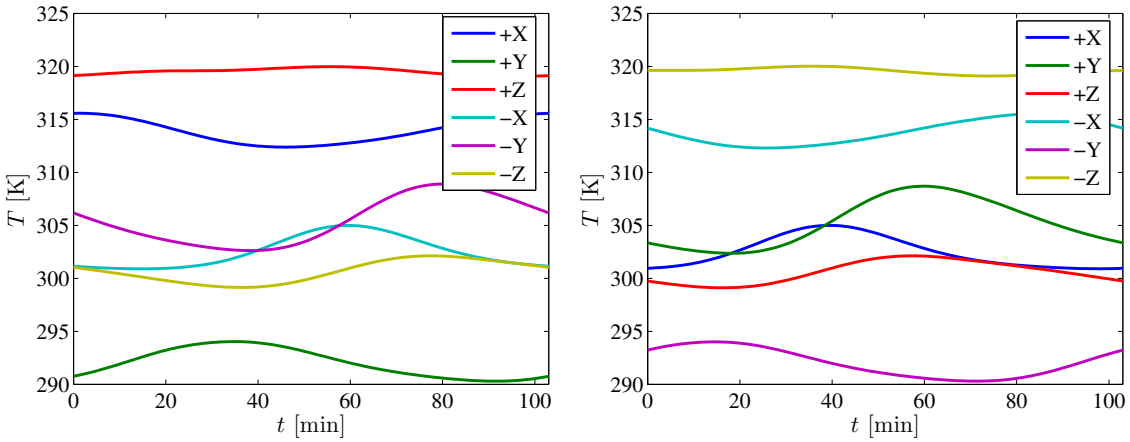

(a) β is maximum. **(b)** β is minimum.

Figure 5.6: Temperature distribution of POL orbit when β angle is maximum and minimum. Pointed star is Proxima, no spin around normal to $+X$ face.

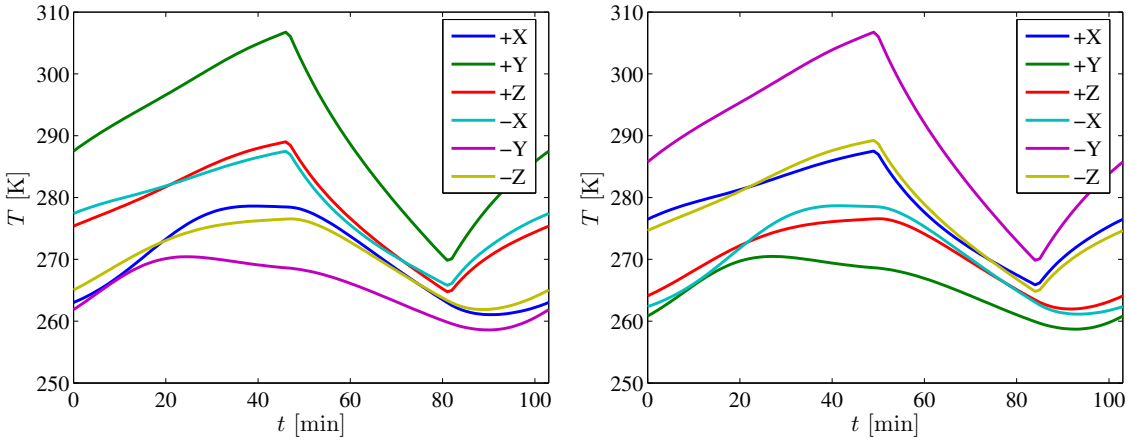

(a) $\beta = 0°$ and is decreasing. **(b)** $\beta = 0°$ and is increasing.

Figure 5.7: Temperature distribution of POL orbit when β angle is null. Pointed star is Proxima, no spin around normal to $+X$ face.

These figures clearly show that in the selected POL orbit case, opposite faces have exactly the same temperature distribution when two simulations are half-year spaced. This particular case is present for this orbit because of the symmetric profile of β angle. This method enables to know the widest range of possible temperatures over the whole year. Indeed, temperature ranges of Fig. 5.6 and Fig. 5.7 can be compared. An extreme β angle (see Fig. 5.5), whether maximum or minimum, leads to maximum temperatures. Otherwise, lower temperatures happen when this angle is null. It is simply explained by the eclipse time of each case. Indeed, a null angle means that the Sun vector is in the same plane as the orbital plane. This directly involves the longest possible eclipse duration, thus the lowest absorbed power by the satellite. Contrariwise, there is no eclipse when β is at its peak values (in this POL orbit case). The absorbed power is then much more important, which allows faces to be at their maximum temperatures.

5.3.2 Temperature distribution justification

Those temperature distributions can be explained by the external environmental fluxes [W/m^2]. Indeed, the absorbed power (governing satellite's temperatures) comes from these fluxes. They are therefore studied at the four strategic dates given in previous subsection. To do this, the absorptivity and emmissivity parameters are not taken into account, as the geometry of satellite faces in order to avoid misunderstandings from the different surface area of faces. These external fluxes are presented here by histograms, giving the mean value on each face at a period corresponding to the strategic date. This is then displayed over one orbital period in Fig. 5.8 for maximum and minimum β angle, and in Fig. 5.9 for the two case of $\beta = 0°$. External fluxes are represented by bars. In blue for Earth IR, in light green for direct Sun and in dark red for the albedo.

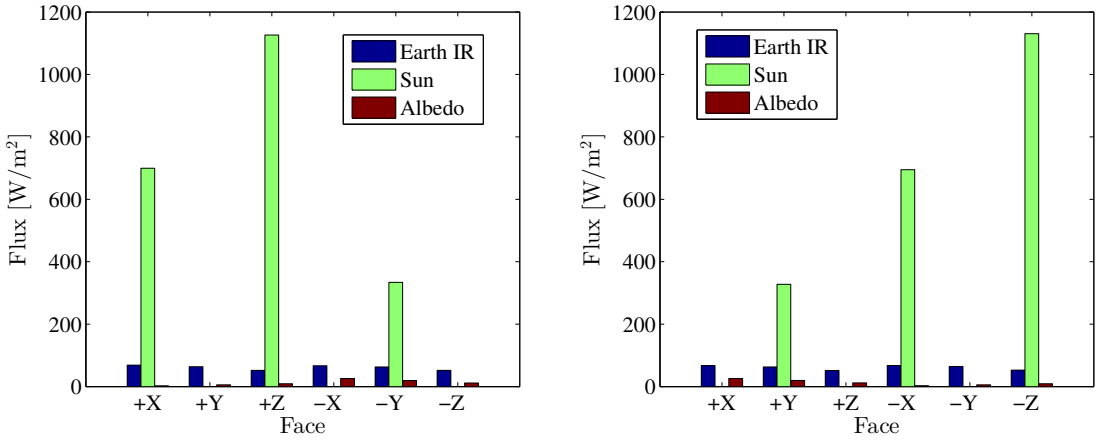

(a) β is maximum. **(b)** β is minimum.

Figure 5.8: Histograms of each external flux acting on each face of the satellite over one POL orbital period when β angle is maximum and minimum. Pointed star is Proxima, no spin around normal to $+X$ face.

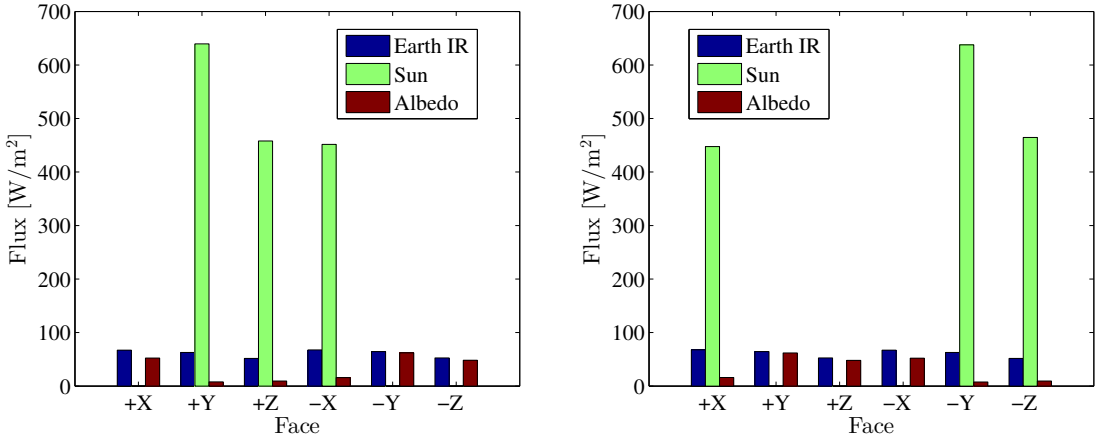

(a) $\beta = 0°$ and is decreasing. **(b)** $\beta = 0°$ and is increasing.

Figure 5.9: Histograms of each external flux acting on each face of the satellite over one POL orbital period when β angle is null. Pointed star is Proxima, no spin around normal to $+X$ face.

An analogy with Fig. 5.6 and Fig. 5.7 allows previous observations to be confirmed and explained by Fig. 5.8 and Fig. 5.9. Indeed, opposite faces receive the same amount of incident external flux from each source when two simulations are done while shifted in time by an half-year. Moreover, this is duly shown that more important is the incident flux on a face, hotter is the equivalent temperature distribution over the corresponding orbit. The main external load for this POL orbit is clearly the direct solar flux.

Furthermore, as it was decided to study selected orbit over a complete year, incident fluxes acting on faces has then to be summarized for all this period. This is illustrated in Fig. 5.10. This is still here without any spin around normal to $+X$ face.

Not surprisingly, the main external fluxes of each face is coming from the direct Sun. But its amplitude is lower compared to the four singular dates where extreme conditions take place. There is also still great similarities between opposite faces during the year. On the other hand, Earth IR and albedo fluxes remain very constants all over the year.

5.3.3 External environmental fluxes while spinning

Actually, the satellite has to rotate around itself in order to enable the nulling interferometry process. This allows incident fluxes generated by external environmental sources to be generalized over the year. This is illustrated with an histogram of external fluxes acting on each satellite's face in Fig. 5.11. Compared to Fig. 5.10 (without any rotation around $+X$ normal axis), whatever the spinning rate is, it will provide the same histogram. Indeed, the very long period here allows the satellite to be in any possible position for several times. Then, all faces receive in average the

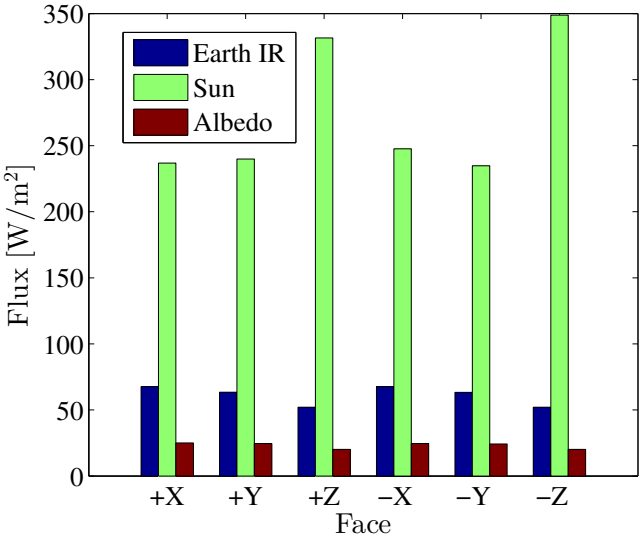

Figure 5.10: Histograms of each external flux acting on each face of the satellite over one year POL orbit. Pointed star is Proxima, no spin around normal to $+X$ face.

same amount of external fluxes during the year, besides $+X$ and $-X$ faces. This is because their orientation remains the same all over the year due to the constant pointing on the star direction.

5.4 Elongation computation

Once temperature distribution can be computed on each node (then each face) thanks to the multi-node model, the satellite linear elongation can hence be deduced. To this end, the temperature variations between faces is introduced before the presentation of elongation computation. As previous sections, this is first performed without any spin and after by spinning the satellite according to the normal of $+X$ face.

5.4.1 Temperature variations between faces

This section presents differences on temperature between satellite's faces. They are noted $\Delta T_{i,j}$ between node (or face) i and j, at each time step (60s). An example is given in Tab. 5.3 which represents maximum differences happening over one revolution when β angle is maximum. This difference can be positive or negative, depending on nodes direction.

The table finally gives a skew-symmetric matrix. Then, the study of the four β cases on POL orbit can be reduced to only β max and $\beta = 0$. Furthermore, the faces of interest in our case are the extremities $+Y$ and $-Y$ because this is where will be placed the two apertures. The temperature differences between the $+Y$ and other faces are illustrated over one POL orbital period in Fig. 5.12. All these differences have been normalized in order to graphically compare all of them.

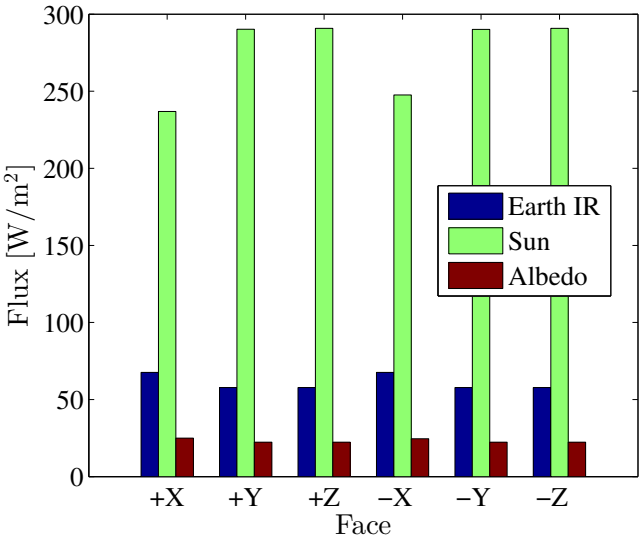

Figure 5.11: Histogram of each external flux acting on each face of the satellite over one year POL orbit. Pointed star is Proxima and satellite is spinning around normal to its $+X$ face.

$\boldsymbol{\Delta T_{i,j\ \max}}$	$+X$	$+Y$	$+Z$	$-X$	$-Y$	$-Z$
$+X$	0	-25	8	-15	-11	-15
$+Y$	25	0	29	13	18	12
$+Z$	-8	-29	0	-19	-17	-21
$-X$	15	-13	19	0	6	-5
$-Y$	11	-18	17	-6	0	-7
$-Z$	15	-12	21	5	7	0

Table 5.3: Maximum temperature difference between faces over one POL orbital revolution pointing Proxima star while β angle is maximum.

This was carried out by subtract the corresponding mean value of each temperature difference. The same figure for $-Y$ with maximum β, as differences when $\beta = 0$ are displayed in the appendix (Fig. 22 and Fig. 23).

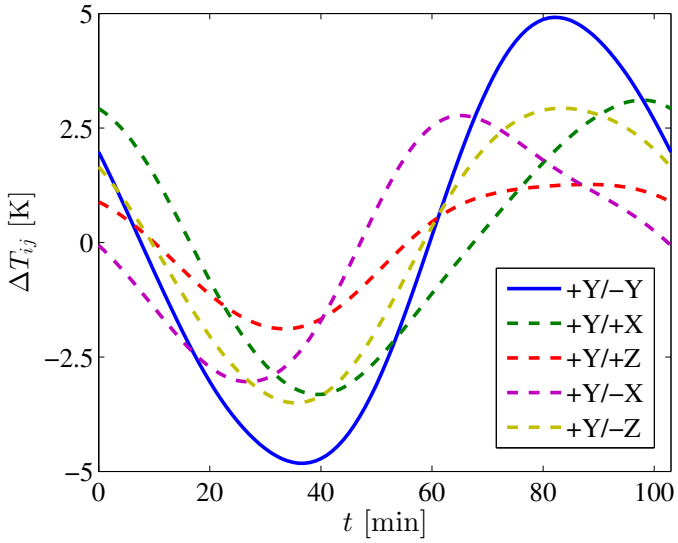

Figure 5.12: Normalized temperature differences between the $+Y$ and other faces over one POL orbital period pointing Proxima star. β angle is maximum.

Those graphs give a first behavior of temperature differences between faces. In each case, extreme difference values appear between $+Y$ and $-Y$ faces. Indeed, those are the furthest faces of the satellite. Then, the evolution of their temperature differences ΔT_{+Y-Y} over one revolution are shown in Fig. 5.13 when β is maximum and also when it reaches zero.

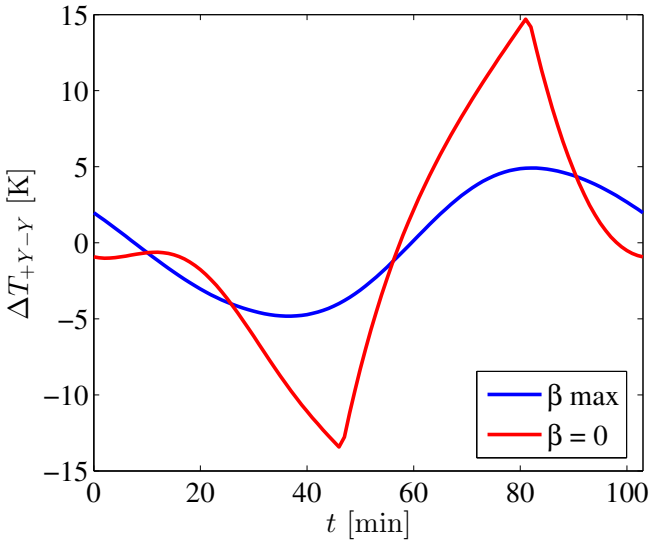

Figure 5.13: Normalized temperature differences between opposites $+Y$ and $-Y$ faces over one POL orbital period pointing Proxima star.

It comes that in this POL orbit case without spinning, the temperature difference between the two opposite faces $+Y$ and $-Y$ (where are located sub-pupils) is generally higher when $\beta = 0°$ at each time step. This temperature difference is the one which governs the elongation of the satellite which will be explain in next subsection. The objective is to minimize this difference in order to have the smaller possible elongation. It could be useful to increase the radiative link between these two faces. Indeed, the two mirrors have to be thermally linked together in order to reduce their temperature difference.

5.4.2 Elongation of satellite's structure

Afterwards, the modified length of satellite after elongation can finally be computed at each time step i. This is useful to be aware of the satellite elongation because it causes defects onto optical performances of the satellite. Actually, the light is reaching the two telescopes which are located at each extremity of the satellite. This light is recombined in the center with a π dephasing angle in one arm of the satellite (see Fig. 1.3). Therefore, a distance modification between the two telescopes involves that the light will not travel the same distance in each arm anymore. This OPD phenomenon involves the decline of optical properties.

Then, the modified length is following this equation:

$$\begin{aligned} L_i &= L_{i-1} + \Delta L_i \\ &= L_{i-1} + L_{i-1}\alpha_{\mathrm{Al}}\Delta T_{+Y-Y}, \end{aligned} \tag{5.3}$$

where L_i is the previous length of the satellite ($L_{init} = 1.2$ m), and $\alpha_{\mathrm{Al}} = 23$ K^{-1} the linear thermal expansion of aluminium.[46]

The relative elongation ΔL in regards to initial length is represented over one POL orbital period in the Fig. 5.14. It is important to not confuse data from this figure with the elongation increment. Indeed, here is represented the deformation length evolution over the orbital period.

Knowing $\Delta L = L\alpha_{\mathrm{Al}}\Delta T_{+Y-Y}$, α_{Al} remains constant while the modified length can also be considered constant due to the highly small deformation compared to the length of satellite (less than 0.1%). The elongation profile is thus the same than ΔT_{+Y-Y}.

The difference between maximum and minimum elongation over one POL orbital period is 0.269 mm when β is at its extremum and 0.776 mm when $\beta = 0$. Those two cases indicate the best and worst possible deformation at this time for that POL orbit. This is still here no spin around normal to $+X$ face.

5.4.3 While spinning

It was stated in Sec. 5.2 that the integration time of the interferometry process is set to 24h. This is then important to know the total linear deformation that will

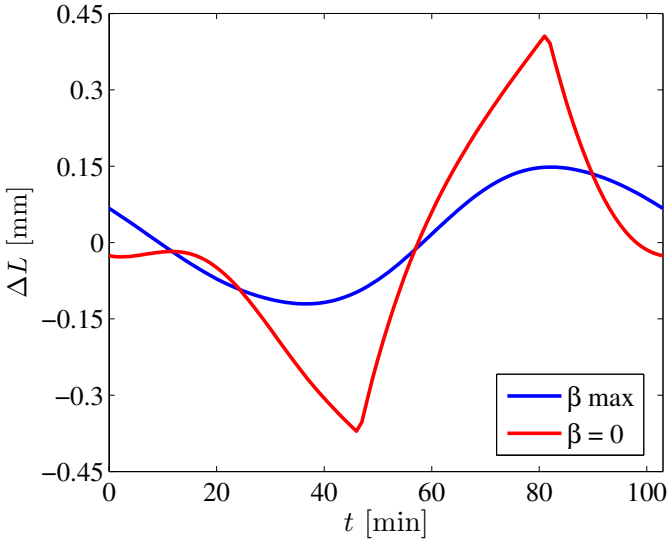

Figure 5.14: Relative elongation of the satellite over one POL orbital period pointing Proxima star.

happen on this day. This is why the elongation is presented in Fig. 5.15 for each different spinning rate around $+X$ normal in the selected POL orbit during a 24h integration time. The two cases of β angle are still taken into account because the objective is to know what is changing during the year.

These figures show that spinning the satellite around itself involves that the deformation profile is governed by a coupling of two distributions: a sinusoid with a period corresponding to the spinning period and the relative elongation profile of one revolution. Indeed, the relative elongation is mainly following a distribution with a period equal to the duration of one complete spin around the normal to $+X$ face. In addition to this, the selected POL orbit makes almost fourteen revolutions around the Earth in 24h. The relative elongation (already presented in Fig. 5.14) due to this orbit is thus repeated fourteen times, acting like perturbation. For example, Fig. 5.15d (for 24h spinning period) enables to clearly distinguish this coupling. Actually, the 24h spinning period is well present, leading the elongation profile. Moreover, the fourteen orbital revolutions are each involving local peaks.

The total elongation ΔL_{tot} seems to slightly increase with a longer spinning period. Moreover, the dilatation rate noted $\dot{L}$ is highly changing. Indeed, shorter is the period for one complete spin, higher will be the rate. However, the evolution of the total difference between the maximum and minimum elongation is not precise enough with only these graphs. This is why the Tab. 5.4 provides all those values in each situation. Note that this is here the mean absolute dilatation rate value $\dot{L}_{\text{mean}}$ which is given.

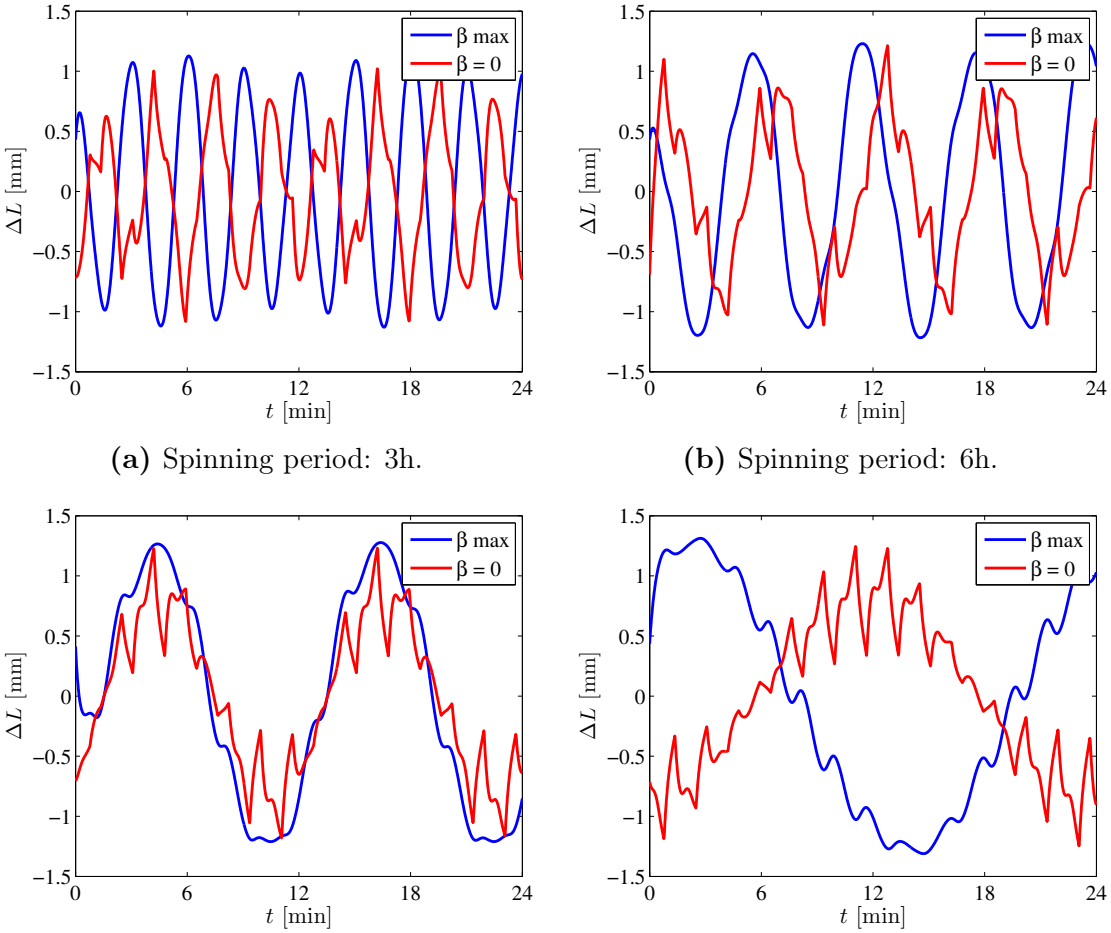

(a) Spinning period: 3h.

(b) Spinning period: 6h.

(c) Spinning period: 12h.

(d) Spinning period: 24h.

Figure 5.15: Relative elongation of the satellite for a one day simulation while satellite is rotating. POL orbital period pointing Proxima star.

Spinning period [h]	β **case**	$\Delta L_{\mathbf{tot}}$ **[mm]**	$\dot{L}_{\mathbf{mean}}$ **[μm/min]**
3	β max	2.26	23
	$\beta = 0$	2.10	20
6	β max	2.45	13
	$\beta = 0$	2.32	16
12	β max	2.49	7
	$\beta = 0$	2.41	13
24	β max	2.62	5
	$\beta = 0$	2.49	12

Table 5.4: Elongation values on each situation of POL orbit pointing Proxima star.

The elongation is slowly increasing with a longer spinning period, contrariwise to the elongation rate which slows down with a long rotation period. Finally, the elongation is highly important to be taken into account. Indeed, after one observation day by the satellite, this elongation has to be offset by satellite components at time t_0 before a new observation day. This offset will allow to be again pointing the exact star position because the elongation of satellite involves an optical shift.

5.5 Complete results for one orbit: POL

All key principles have been introduced until here. Hence, all relevant results can be presented in this section. It was decided to give results from the peculiar polar orbit while pointing to all chosen stars. The aim is to be convenient by describing the whole process for the same specific orbit before adapt it to all other ones. Pertinent temperature and elongation values are finally discussed.

5.5.1 Relevant values

Results of the selected POL orbit can finally be computed for all five chosen stars: Proxima, Barnard's star, Epsilon Eridani, Ross 128 and Tau Ceti. First, in addition to the histogram of Fig. 5.11 for Proxima star, all histograms of each external flux acting on each face of the satellite over one year are given in Fig. 5.16. The observation already given when pointing Proxima star is the same for all other stars. Indeed, all faces receive in average the same amount of external fluxes during the year, besides $+X$ and $-X$ faces. This is due to their position which remains the same all over the year by constantly pointing the star.

Secondly, all relevant faces temperature values in all corresponding cases are summed up in the Tab. 5.5 for Proxima star and in the appendix (Tab. 3 and Tab. 4) for the four other stars. This is given for all spinning periods noted τ_{spin} and only the two β angle cases (maximum and null) because the two others are equivalent. However, only $+Y$ and $-Y$ faces are represented since the two sub-pupils will be located near to these extremities of the satellite. The maximum, minimum and mean temperature are represented. Maximum and mean absolute temperature variation of faces are also given. Those temperature values are given for a 24h simulation, which represents one observation duration of the satellite.

From these tables, the same remark stated in Sec. 5.2 can be done on the temperature variation. When the period of spin τ_{spin} around normal to $+X$ face is decreasing, the mean temperature variation on a face is increasing. In addition, higher is the period, more the minimum temperature is diminishing, while the mean temperature remains constant as the maximum temperature.

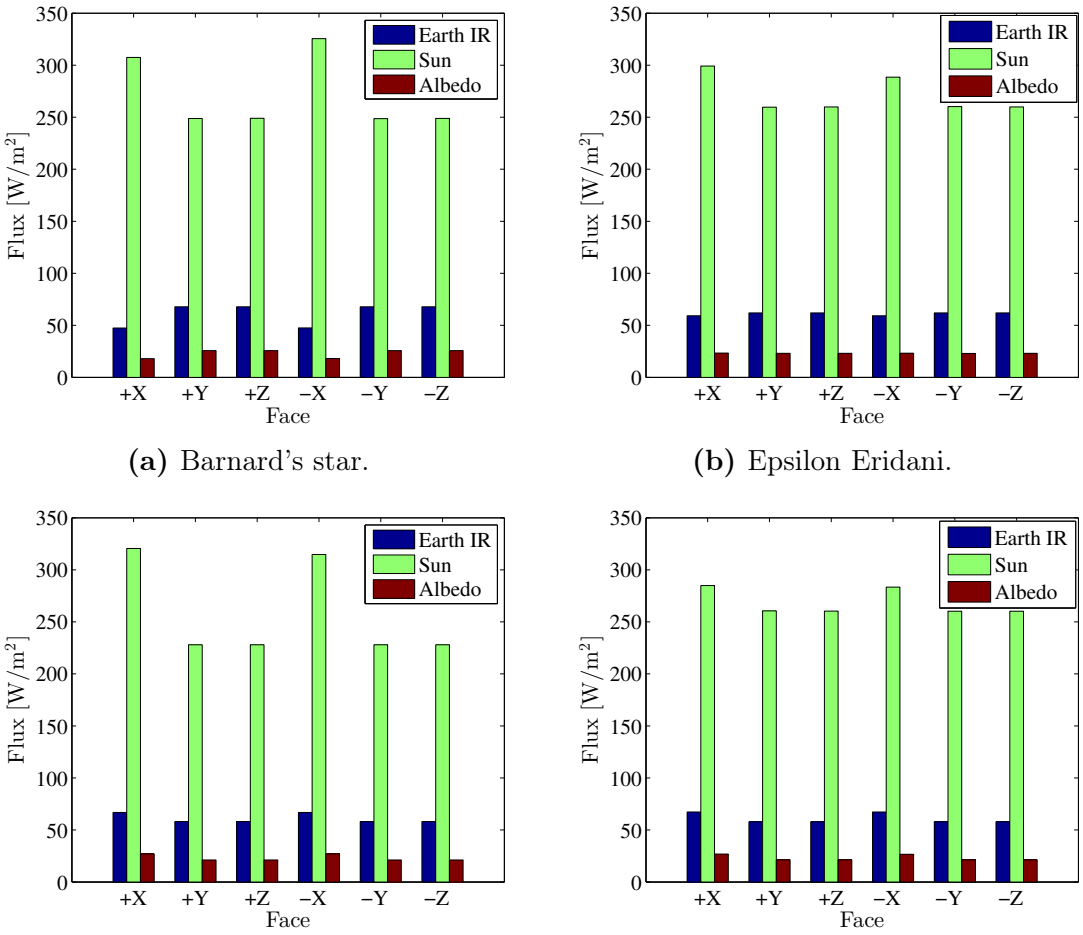

(a) Barnard's star.

(b) Epsilon Eridani.

(c) Ross 128.

(d) Tau Ceti.

Figure 5.16: Histogram of each external flux acting on each face of the satellite. Results over one year POL orbit while spinning around normal to $+X$ face and pointing Barnard's star, Epsilon Eridani, Ross 128 and Tau Ceti.

Star	τ_{spin}	case	Face	$T_{\max}$	$T_{\min}$	T_{mean}	$\lvert\dot{T}\rvert_{\max}$	$\lvert\dot{T}\rvert_{\text{mean}}$
				[K]	[K]	[K]	[K/min]	[K/min]
Proxima	3h	β max	$+Y$	324	278	297	1.16	0.44
			$-Y$	322	278	296	1.33	0.44
		$\beta = 0$	$+Y$	311	260	276	1.97	0.51
			$-Y$	312	260	276	1.83	0.51
	6h	β max	$+Y$	325	276	297	0.85	0.26
			$-Y$	324	275	296	0.78	0.27
		$\beta = 0$	$+Y$	313	253	276	1.95	0.45
			$-Y$	311	256	276	2.15	0.45
	12h	β max	$+Y$	325	271	296	1.16	0.17
			$-Y$	323	271	296	0.74	0.16
		$\beta = 0$	$+Y$	313	254	276	2.02	0.42
			$-Y$	313	252	276	2.22	0.42
	24h	β max	$+Y$	322	267	296	0.35	0.11
			$-Y$	326	274	296	1.42	0.13
		$\beta = 0$	$+Y$	312	249	277	2.17	0.42
			$-Y$	312	252	277	2.18	0.42

Table 5.5: Summary of relevant temperature values on $+Y$ and $-Y$ faces. Proxima star, all spinning periods τ_{spin}, the two β angle cases, one day simulation.

5.5.2 Corresponding elongation

For the following step, it is important to know the total elongation of the satellite in each situation: pointed star, spinning period and β angle. Results of these elongations are then given for two separate situations. The Fig. 5.17a shows results when the angle between Sun vector and its projection on the orbital plane (β) is maximum. The Fig. 5.17b illustrates elongations when Sun vector is on the orbital plane (i.e. $\beta = 0°$).

The first observation that can be made is on the increase of the total elongation according to a longer rotation period τ_{spin}. This is due to the fact observed two paragraphs below on the minimum temperature. In fact, due to the drop on minimum temperature, the variation between faces $+Y$ and $-Y$ (ΔT_{+Y-Y}) is obviously more important. Hence, the total elongation which is considered to be proportional to this temperature difference (see Eq. 5.3), is increasing with a longer τ_{spin}.

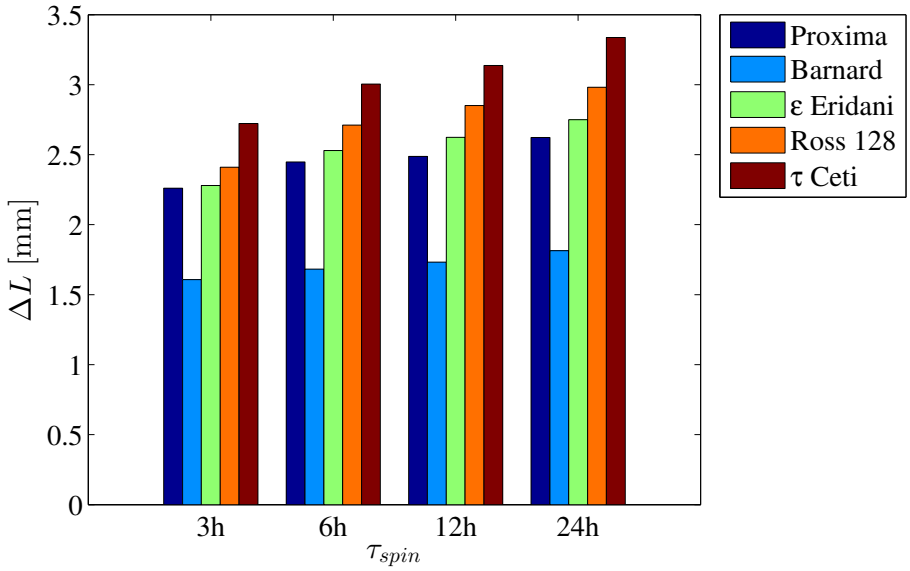

(a) β angle is maximum.

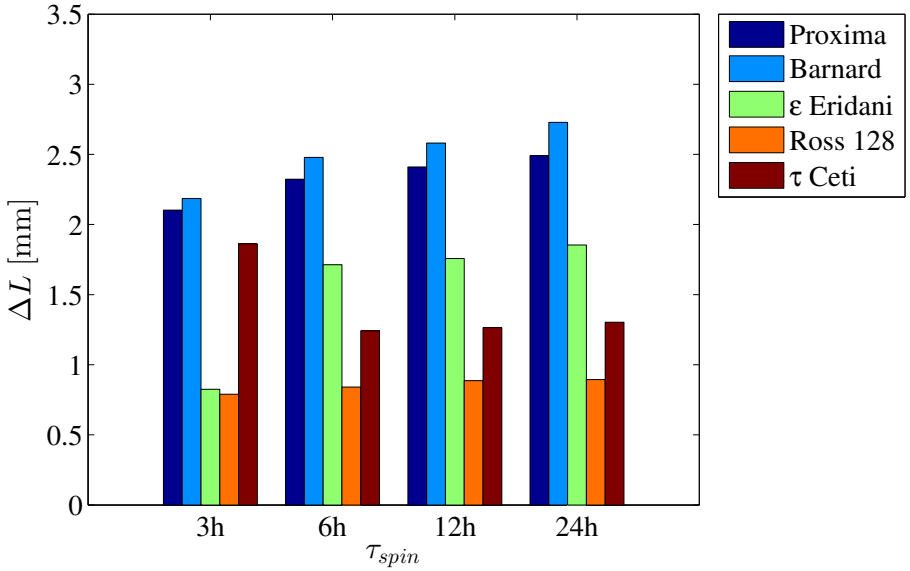

(b) β angle is null.

Figure 5.17: Total elongation of one day simulation on POL orbit in each star pointing case.

5.6 Elongation range

The objective of this section is to present the elongation ranges of the selected POL orbit. That is the smallest and the largest possible elongation estimation over the year. The Φ angle is first introduced. Then, this approach is applied onto POL orbit.

5.6.1 Introduction of Φ angle influence

From the previous section, the total elongation appears to be bigger when β angle is maximum for all stars, besides for Barnard's star. However, this is not β angle which has the main influence on the total elongation but the angle between Sun and star vectors. This angle is noted Φ and depicted in Fig. 5.18[12]. For the two β cases then, the POL orbit is represented with all stars and Sun directions in Fig. 5.19 in order to be able to do a visual estimation of Φ angles. Moreover, values of those angles are picked up with the corresponding total elongation (τ_{spin} = 12h case) in Tab. 5.6. The Φ angle is ranged from 0° to 90° instead of 180° due to the symmetry beyond 90°.

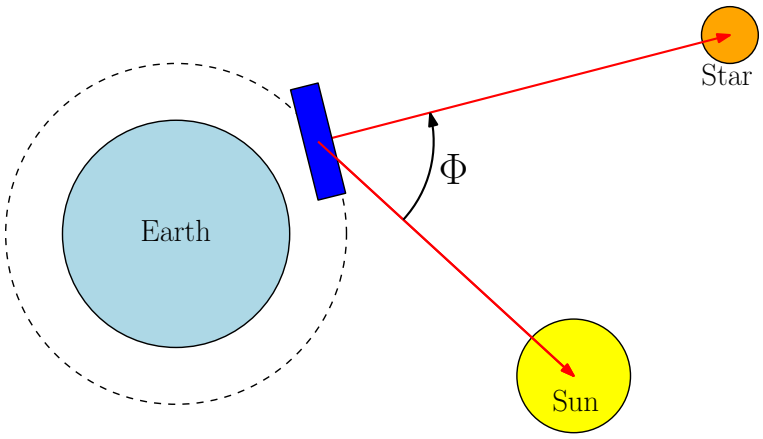

Figure 5.18: Presentation of Φ angle: angle between the Sun and star vector.

	β max		$\beta = 0°$	
Star	Φ [°]	ΔL_{tot} [mm]	Φ [°]	ΔL_{tot} [mm]
Proxima	59	2.49	60	2.41
Barnard's star	31	1.73	77	2.58
Epsilon Eridani	59	2.62	43	1.76
Ross 128	74	2.85	17	0.89
Tau Ceti	86	3.14	25	1.26

Table 5.6: Summary of Φ angles and their corresponding total elongation when τ_{spin} = 12h for all selected stars.

[12] Φ angle is assumed to be the same from the Earth and the satellite because their difference is highly negligible compared to the distance with those stars.

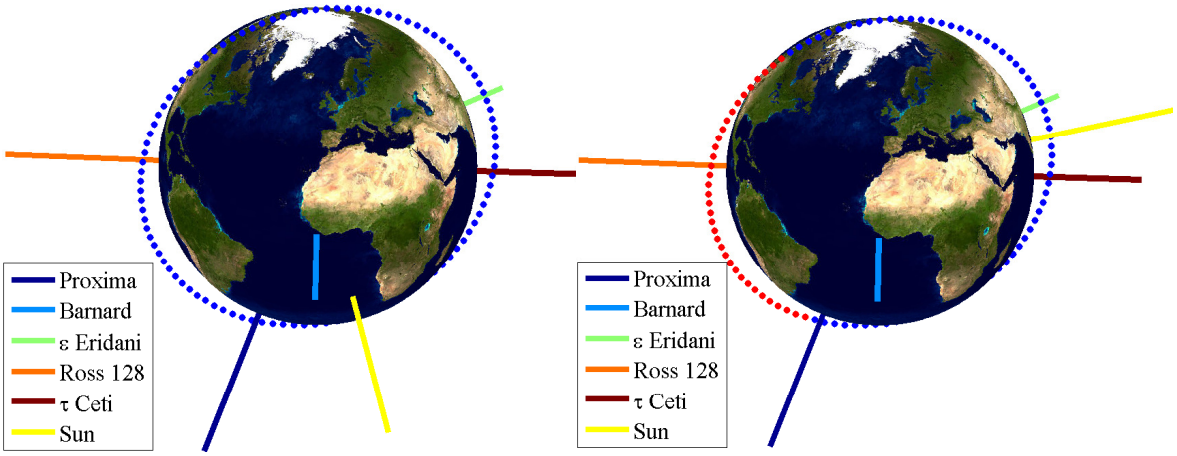

(a) β is maximum. **(b)** $\beta = 0$.

Figure 5.19: Stars and Sun directions for POL orbit in the two β cases.

This Tab. 5.6 confirms that the total elongation is mainly governed by the Φ angle. Higher is this angle, more important will be the corresponding elongation. Indeed when Φ is maximum, i.e. $\Phi = 90°$, the Sun is perpendicular to the rotation axis of the satellite. Because $+X$ face is always pointing the star, it cannot be viewed directly by the Sun, as $-X$ face. Hence, the rotation of the satellite around itself makes that others faces ($+Y$, $+Z$, $-Y$ and $-Z$) are successfully pointing the Sun. As a consequence, the temperature difference between opposite faces where are located sub-pupils (ΔT_{+Y-Y}) is obviously in the worst possible case. This is entirely due to the view succession of these faces to the Sun with the optimal angle.

On the other hand, the β angle influence on this maximum elongation cannot be neglected. Taking as example Proxima in the Tab. 5.6, even with a slightly smaller Φ angle (59° versus 60°), the total elongation is a little bigger when β angle is maximum. In fact, the main impact of β angle is on the satellite temperatures as shown in Tab. 5.5, with still a role on the elongation but considered as secondary compared to the influence of Φ.

5.6.2 Application on POL orbit

The Φ angle is introduced representing the angle between Sun and star vector. Hence, extreme cases can be presented. Indeed, this is then possible to find the worst and the best possible elongation in the actual configuration of the satellite and for all pointed stars. It has been explained just previously that the largest elongation appear when $\Phi = 90°$. Otherwise, the smallest elongation happens when this angle is at its extremum. The Φ angle evolution over the year is therefore illustrated in Fig. 5.20 for all stars.

This figure of Φ evolution enables to detect the dates at which this angle is at an extremum or at the 90° value. Indeed, this identification is useful in order to do the simulation for each star at those corresponding dates over the year. Moreover, the angle evolution is identical for all orbits since its definition is done with respect

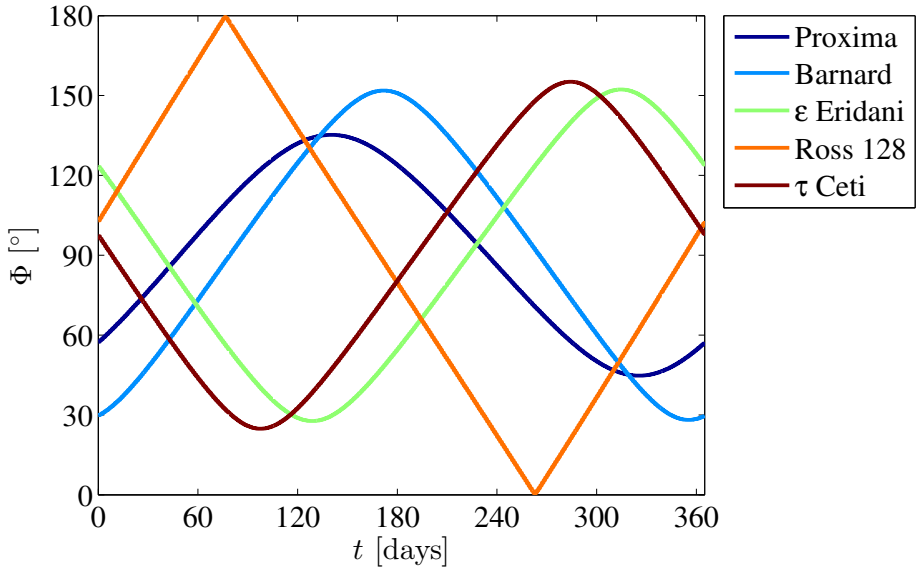

Figure 5.20: Evolution of Φ angle over year 2020 for all selected stars.

to the satellite position. Relevant dates are then summed up in Tab. 5.7. All Φ evolutions reach two times per year both extremum and a value equal to 90°.

Dates	Maximum Φ	First Φ = 90°	Minimum Φ	Second Φ = 90°
Proxima	May 20	February 18	November 21	August 21
Barnard's star	June 20	March 19	December 21	September 22
Epsilon Eridani	November 10	February 07	May 08	August 10
Ross 128	March 17	June 17	September 19	December 18
Tau Ceti	April 07	January 08	October 11	July 09

Table 5.7: Relevant dates where important Φ values happen over 2020 year.

Therefore, the total best and worst case on satellite elongation are shown in Fig. 5.21. This finally allows to be aware of the elongation range of possibilities, done for satellite's structure in its actual configuration. A remark on POL orbit is that results are identical for both maximum and minimum Φ angle, or even for each date where Φ = 90°. This is due to the fact that β and Φ evolution are both symmetric. However, these four dates are still useful since some β angle profile from other orbits are not perfectly symmetric.

All relevant data for the selected POL orbit over one year are then presented and explained in this chapter. Those methods can now be adapted to all other selected orbits of this study.

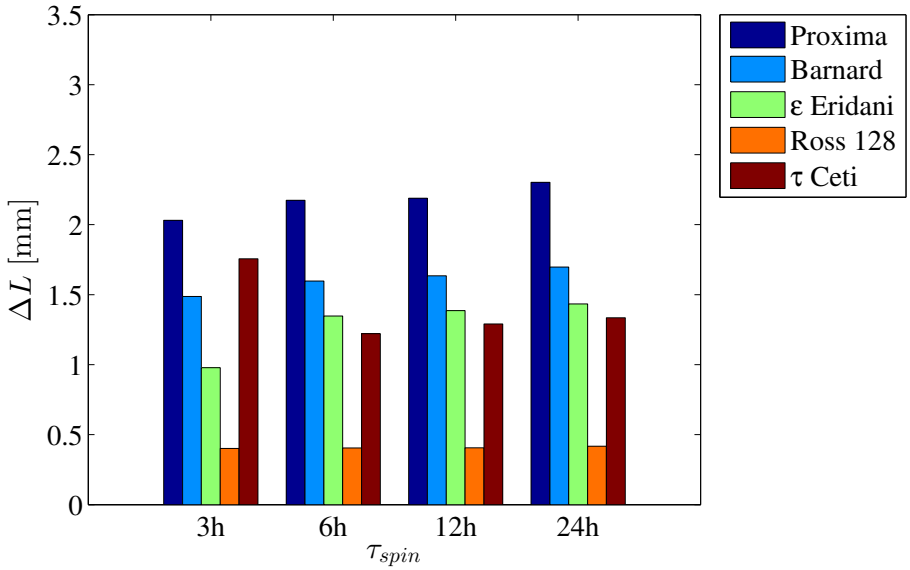

(a) Smallest possible elongation: Φ is extremum.

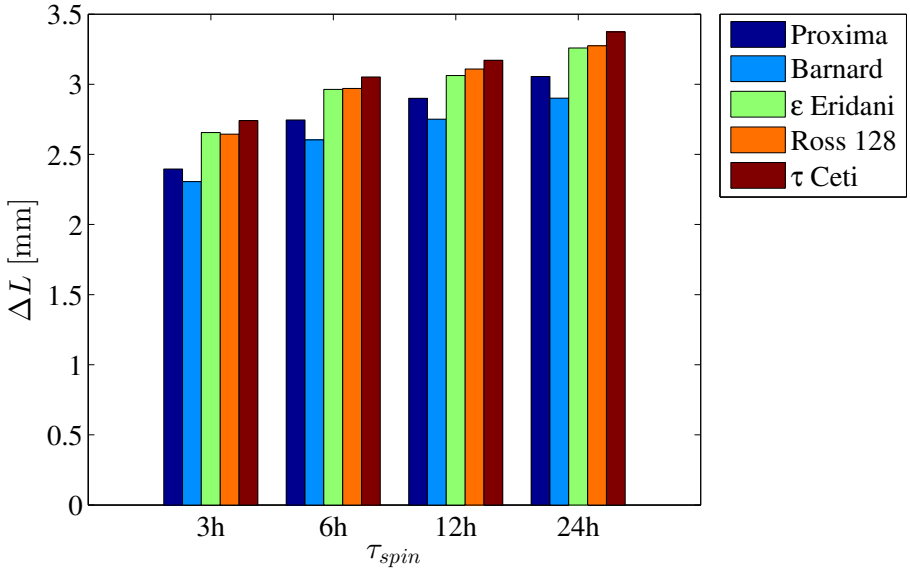

(b) Biggest possible elongation: $\Phi = 90°$.

Figure 5.21: Smallest and largest possible elongations over one day of POL orbit for all stars and spinning periods.

Chapter 6

General results

All parameters allowing the study of temperature distribution, variation and also the corresponding satellite's elongation for POL orbit are analysed. This chapter is then presenting the results for all other selected orbits from Tab. 3.1. As stated in Sec. 3.3, some orbits are fixed while others have some variables in their orbital parameters. This is the case of SMI and SSO orbits because they was introduced with some different Local Time of the Ascending Node (LTAN). In addition, SSOs are also study for three altitudes: 400 km, 600 km and 800 km. It begins by the presentation and discussion of the complete results from these two various orbits (SSO and SMILE). It continues by giving and compare results for each kind of orbit: first the LEOS, second the HEOs and GEO. It ends by a discussion onto improvements ideas on optical properties of the nulling interferometry process, according to the obtained results.

All ranges from this chapter are presented for all spinning period studied in this work: 3h, 6h, 12h and 24h. The corresponding spinning period of each range is specified on the left of each graph. In addition, each range presents the minimum and maximum value (both temperature and elongation) of the considered case. A range is therefore drawn and represented by an horizontal color bar from the minimum value (left) to the maximum value (right).

6.1 SSO results

The first results of this chapter are given for SSO orbits because their altitude and its LTAN was introduced as variables. The principal characteristic of this kind of orbit is reminded to make a constant angle between the orbital plane and the Sun vector.

6.1.1 Angles variations: β and Φ

First parameters taken into account are the angles β and Φ. β allows to obtain the dates at which the maximum and minimum temperatures take place, while Φ enables to know the largest range of possible elongations. The β angle (between

Sun vector and its projection onto the orbital plane) remains constant with respect to the altitude of the orbit. In contrast, it is varying with the LTAN. The β angle evolutions over the year for the different considered LTAN (from 0 to 24h) are displayed in Fig. 6.1.

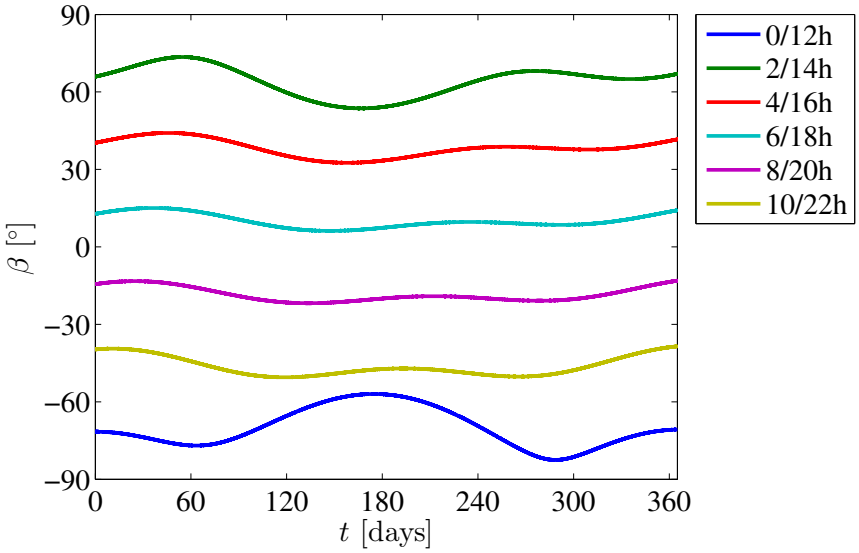

Figure 6.1: Evolution of β angles over 2020 year for SSOs with different LTAN from 0 to 24h.

Compared to β angle evolution of POL orbit, SSO is much less varying. In addition, this is even more true when the LTAN is corresponding to a β angle close to zero. In order to obtain the largest range of possibilities, it is convenient to compute results from extreme β angle cases. That are when this angle distribution is extremum and when it is the closest to zero. For this purpose, two new simulations comes from this Fig. 6.1. They are done for a LTAN of 1/13h and 7/19h using the SIMU-CIC propagator from CNES. This allows to obtain the best and worst possible cases because a LTAN at 1/13h corresponds to the higher β angle distribution while a 7/19h LTAN gives always a β angle pretty close to a zero. This is illustrated in Fig. 6.2.

As explained at the end of the previous chapter, the Φ angle remains the same regardless the selected orbit. Temperature ranges will then be obtained when the β angle is at its maximum and minimum, i.e. for 1/13h and 7/19h LTAN. In addition, elongation ranges will be presented for dates combining $\Phi = 90°$ with the maximum β for the largest elongation, and a β close to zero while Φ is at an extremum for the smallest elongation.

6.1.2 Temperature range

The study of SSOs for the two LTAN of 1/19h and 7/19h allows to estimate the range of temperatures happening on satellite faces for the extreme β angle cases. At an altitude of 600 km, these ranges are represented in Fig. 6.3 for Proxima star, and

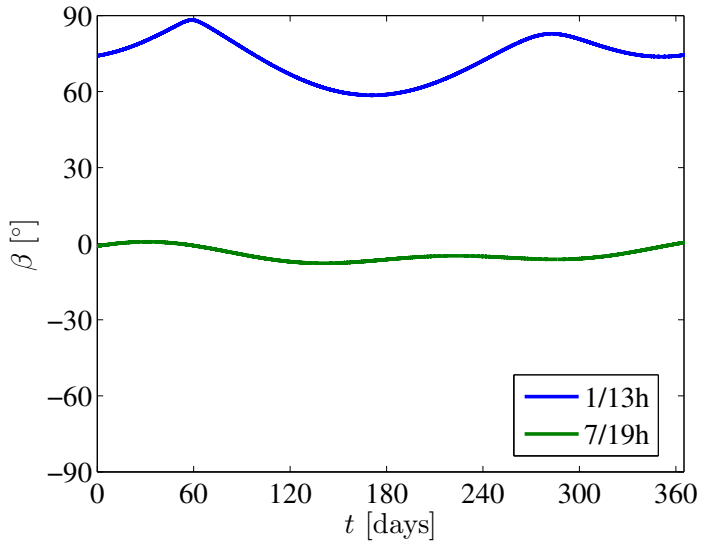

Figure 6.2: Evolution of β angles over 2020 year for SSOs at extreme LTAN: 1/13h and 7/19h.

in the appendix from Fig. 24 to Fig. 27 for all other stars. The minimum temperature is found by taking the minimum temperature of the corresponding orbit when β angle is null, or the closest to zero. On the other hand, the maximum temperature comes from the moment when β angle is at one of its extremum. Results from all spinning periods are given in these figures. Note also that the considered temperatures ranges are the worst of each opposite face. In fact, those ranges are quite similar since once a face is in a particular situation, its opposite face will hence be in a very similar situation during the year. They are therefore considered as equals.

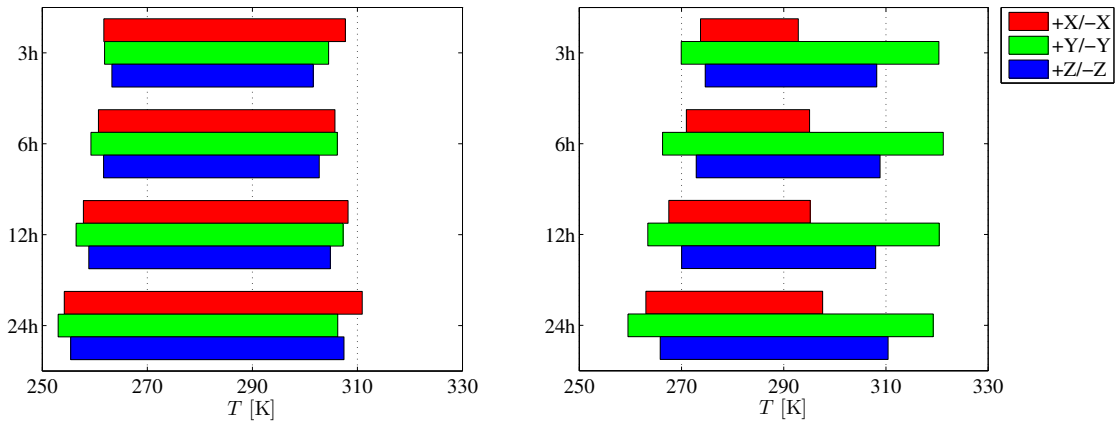

(a) 7/19h LTAN. **(b)** 1/13h LTAN.

Figure 6.3: Faces temperature ranges of the two studied extreme 600 km SSOs over 2020 year, for all selected spinning periods and pointing Proxima.

As expected, graphs from all pointed stars are respecting the predicted range behavior. Indeed, temperatures obtained with the 7/19h LTAN (β angle close to zero) are weaker than the ones of 1/13h LTAN where β at its extremum. Temperatures

maximum and minimum are however approximated. The minimum temperature is still lower when the spinning period is higher. In many cases, values are quite similar for all faces. Ranges are then based on estimations because simulations cannot be done at each time step over the whole year, but only at some strategic days of when $\beta = 0°$ or is extremum. This is why a few defects can appear in some results. Moreover, orders of magnitude of those ranges are varying across the stars. This is due to the orientation of the satellite compared to the Sun at the date where temperature estimations are performed. If satellite's orientation is in a way involving a high effective area ratio from the direct Sun, the corresponding satellite's temperature will therefore be hotter and vice versa. Finally, at this 600 km altitude, a SSO with an arbitrary LTAN will therefore have its temperature included in those ranges given by SSO results with 7h/19h and 1h/13h LTAN.

6.1.3 Elongation range

The ranges corresponding to the elongation are created by computing the smallest and largest elongation happening over the year. This is done by finding the combination between Φ and β angles which provides those elongations. Reminds that Φ is the angle between star and Sun vector (see Fig. 5.18). As stated in Tab. 5.7, situations where $\Phi = 90°$ or Φ is extremum are happening at two dates over the year. The date is finally chosen according to the β angle. Ranges of elongation possibilities appearing in 24h over the year are then given in Fig. 6.4 for the two SSOs at 600 km altitude.

First, a low rotation period around normal to $+X$ face seems to produce lower elongations. Indeed, it was previously seen that a long rotation period involves a colder minimum temperature. Therefore, it is directly increasing the temperature difference between faces, and then the equivalent elongation of the structure. Depending on the LTAN and the pointed star, ranges order of magnitude are stabilizing from a certain spinning period, as mainly seen in Fig. 6.4a.

Concerning values of elongation extremum, the maximum elongation is quite similar regardless of the pointed star. Indeed, this is due to the fact that the date at which the elongation is computed corresponds to $\Phi = 90°$ for all the stars. The small variation on these larger elongations is then due to the β angle value at this date, which involves a little impact on this maximum compared to Φ. Otherwise, the minimum elongation is more varying. As the corresponding date for this elongation over 24h is computed when Φ is extremum, depending on this angle value. Referring to Fig. 5.20, the maximum values are summed up in Tab. 6.1, which is valid for all orbits. The minimum Φ angle could also be given, but it cannot yield more information since it has the same influence than the maximum Φ.

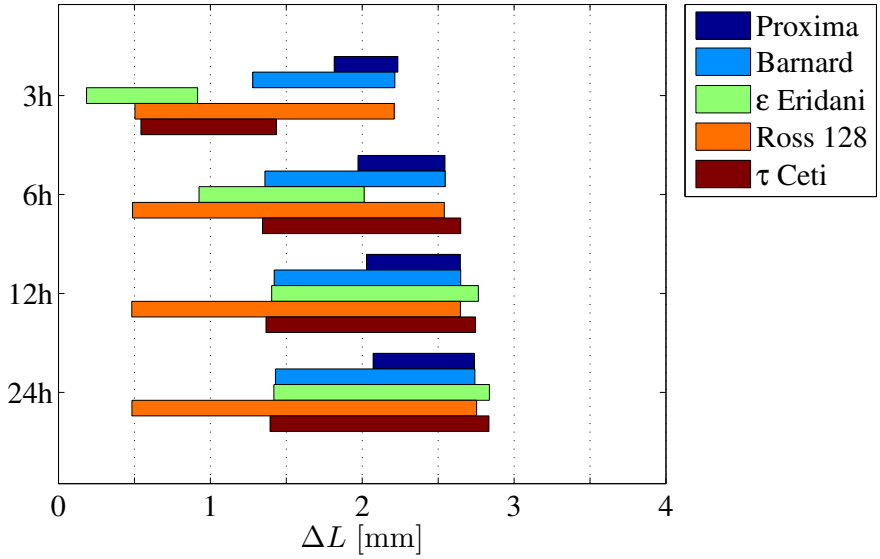

(a) 7/19h LTAN.

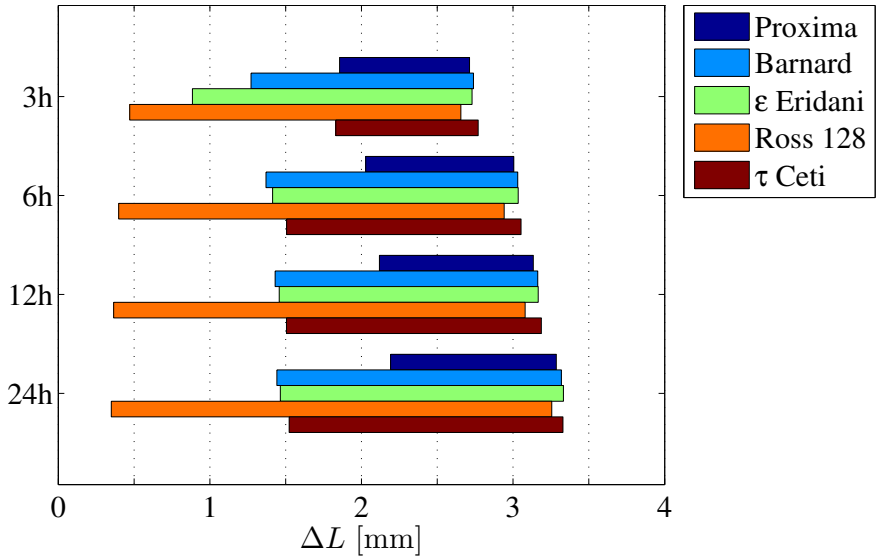

(b) 1/13h LTAN.

Figure 6.4: Elongation ranges in 24h of the two studied extreme 600 km SSOs over 2020 year for all selected spinning periods.

Star	Φ_{max} [°]
Proxima	135
Barnard's star	152
ϵ Eridani	152
Ross 128	180
τ Ceti	155

Table 6.1: Values of maximum Φ angles happening over the year for all selected stars.

This table confirms the influence of this angle. Indeed, the higher Φ appears when pointing Ross 128, which has the lower possible elongation. In the other hand, the maximum angle observed when Proxima star is pointed is the lowest of all stars. This is therefore for this reason that the minimum possible elongation of the satellite is higher for Proxima than for the others. Finally, minimum elongation for Barnard's star, ϵ Eridani and τ Ceti are quite similar as expected from the table. The widest range of elongations is then observed for Ross 128, while the smallest is for Proxima. It is also important to remember that there is still a small influence which is coming from β angle.

Since the two cases of LTAN providing the extreme β angle distributions are presented, the ranges of possible elongations for SSOs at 600 km altitude are included between these two cases, whatever their LTAN are. Furthermore, the range bandwidth will be wider when the chosen LTAN is providing a higher β distribution, as the 1/13h LTAN case.

6.1.4 Altitude variation

The two previous subsections present the temperature and elongation ranges for SSOs. The altitude was fixed to 600km, but it is interesting to look if altitude has a significant influence on those ranges.

6.1.4.1 Temperatures

First, temperature variations are compared for the same orbit at 400 km, 600 km and 800 km. Once again, the two SSOs cases of 7/19h and 1/13h LTAN are studied in order to be aware of the coldest and hottest possibilities. Results are presented in Fig. 6.5 for Proxima star, and from Fig. 28 to Fig. 31 in the appendix for all other stars. Temperature ranges are no more given for each opposite faces. Indeed, it was decided to generalized them for all the satellite. This is done by taking the minimum temperature of all faces as the coldest and the maximum of faces as the hottest one. They are estimated in order to be able to represent the range of possibilities all over the year.

Most of the graphs show that gaining altitude is not significantly changing the temperature ranges. The bandwidth seems all the same to slowly diminish while increasing the temperature. This change is most of the time extremely small, but could rarely be reduced by more than 10% after an altitude rise of 400 km (which represents a dubbed altitude). While ranges behavior for all stars are consistent, there are however some strange changes happening at the minimum temperature of the 7/19h LTAN case. In order to understand this, one has to look at the date when those temperatures are computed. For this purpose, β angle distributions for each altitude have to be displayed in Fig. 6.6. Even if those distributions seems to be very similar, a zoom where those angles are crossing zero allow to see that dates are not the same for the different altitudes. Indeed, they are shifted by approximately four days for every 200 km. Therefore, it explains the variations on minimum temperatures, which are induced by the different attitude and satellite orientation.

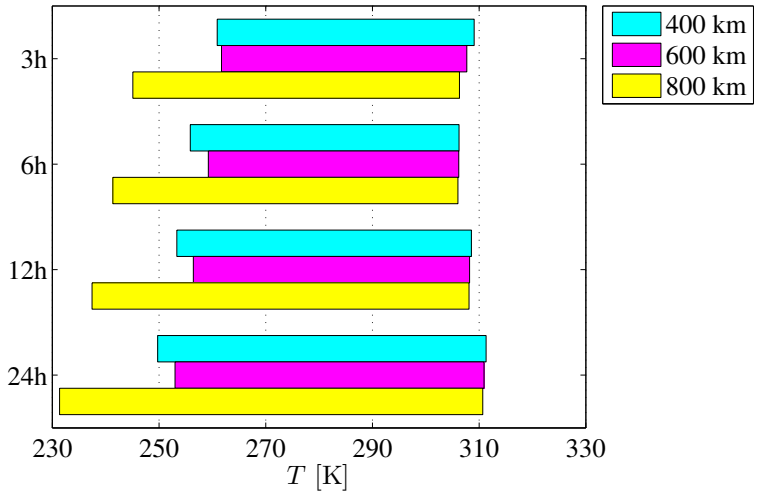

(a) 7/19h LTAN.

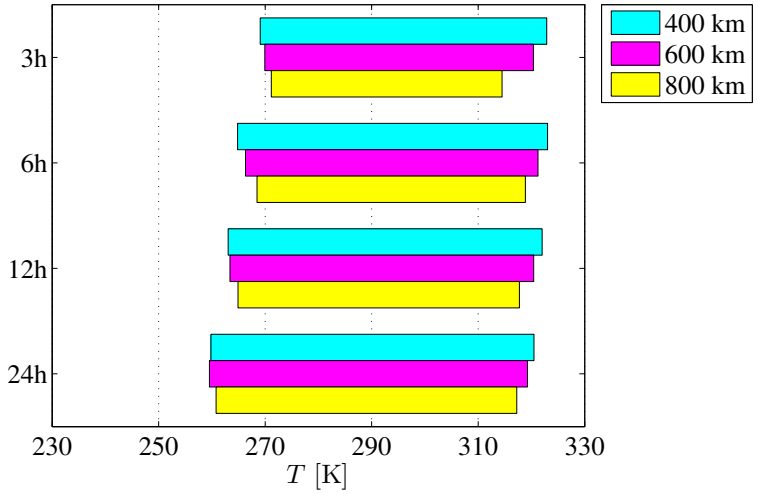

(b) 1/13h LTAN.

Figure 6.5: Temperature ranges of the satellite for different altitudes of SSOs over 2020 year. Two extreme LTAN cases are represented for all selected spinning periods and pointing Proxima.

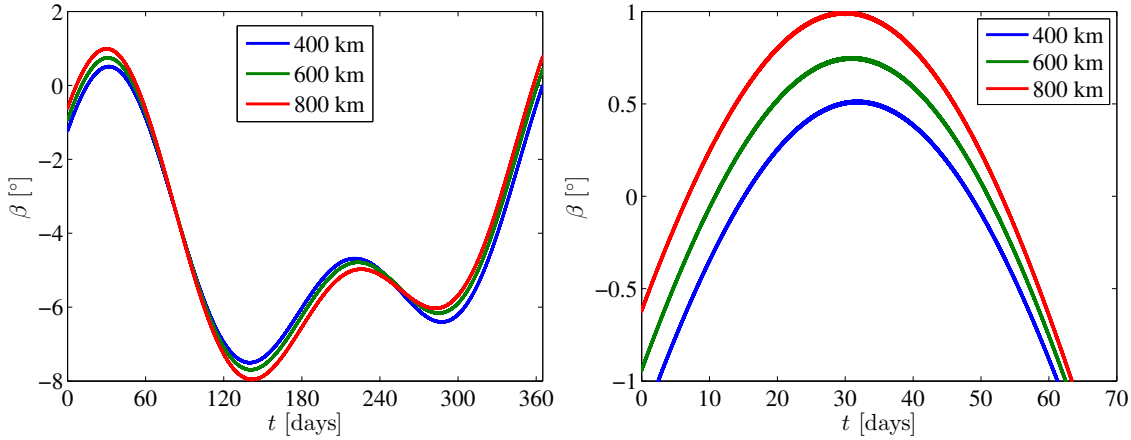

Figure 6.6: Evolution of β angles over 2020 year for 7/19h LTAN SSOs with different altitudes (400 km, 600 km and 800 km) and its zoom on dates where it crosses zero.

6.1.4.2 Elongations

This is also important to be aware of the altitude's influence onto elongations. To that end, the elongation ranges are estimated and represented in Fig. 6.7 and Fig. 6.8 for the two LTAN SSOs cases at the different selected altitudes. The elongations are still the one that can be observed in one day over the year.

The first observation that can be done is that an altitude change is not involving a significant change on satellite's elongation. Results from the spinning period of 3h in both LTAN cases but mainly 7/19h seems to be too sparse in order to take those estimations under consideration. This is clear that results are much more stabilized and useful start from a spinning period of 6h, even if they are not yet perfectly constant at this period. As explained previously, maximum elongations are increasing with a lower spinning period around normal to $+X$ face because the temperature difference between tip faces is higher. However, for a same spinning period, this is not convenient to speak about elongation modifications since changes are hardly slights. Indeed, the range's widths are rarely exceeding 15% of increase for 7/19h LTAN with a 400 km rise of altitude. Even better, bandwidths are not increasing more than 3% for 1/13h LTAN, besides when pointing ϵ Eridani which is at 400 km in a more particular orientation. In fact, all those ranges are conducted by the temperature differences shown just previously, which remain fairly constants with the altitude. This is why an altitude increase is not involving meaningful variations on those ranges.

6.2 SMILE orbits results

"The SMILE mission aims to build a more complete understanding of the Sun-Earth connection by measuring the solar wind and its dynamic interaction with the magnetosphere."[47]

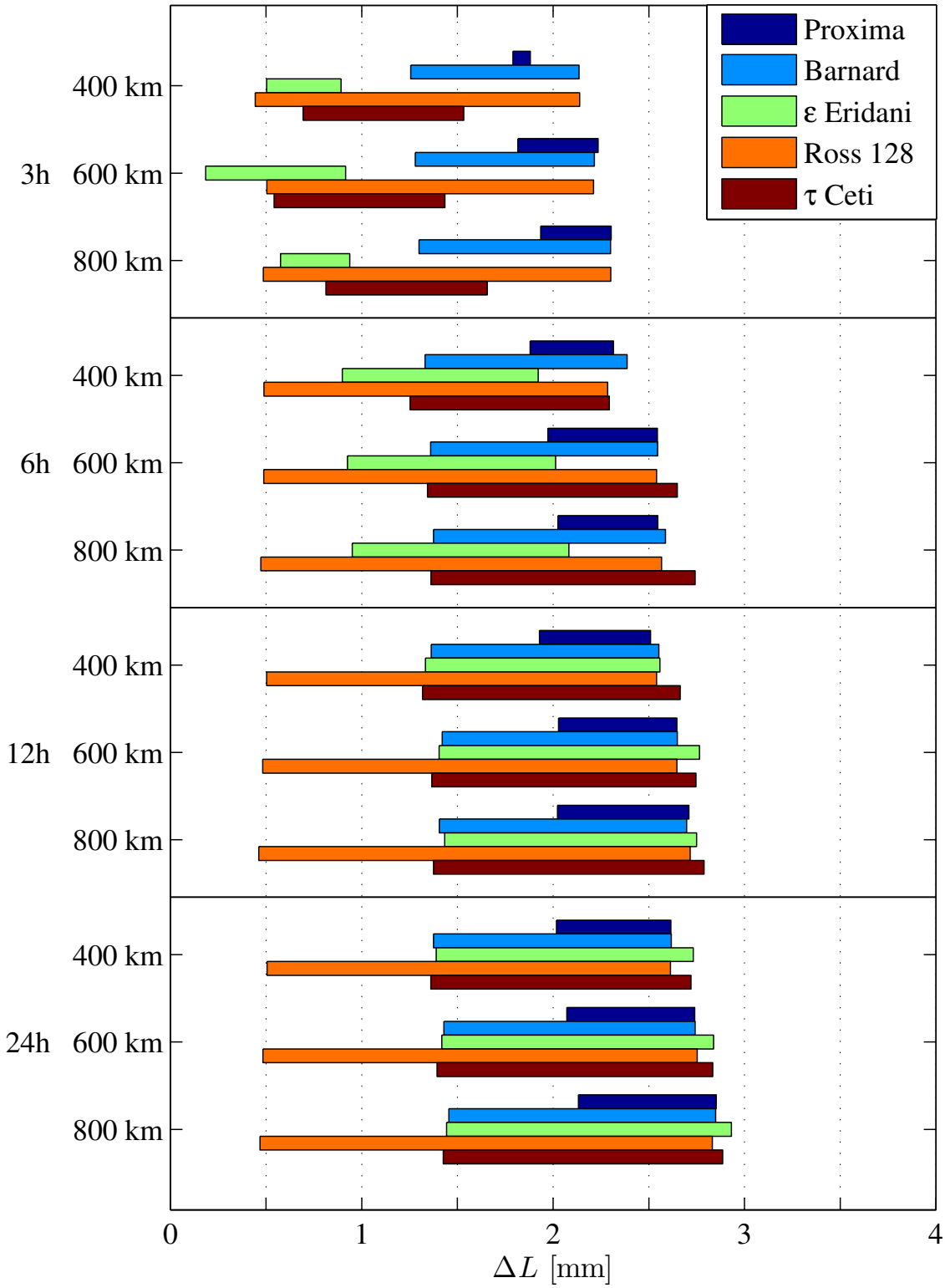

Figure 6.7: Elongation ranges estimation in 24h for 7/19h LTAN SSOs at different altitudes and for all selected spinning periods.

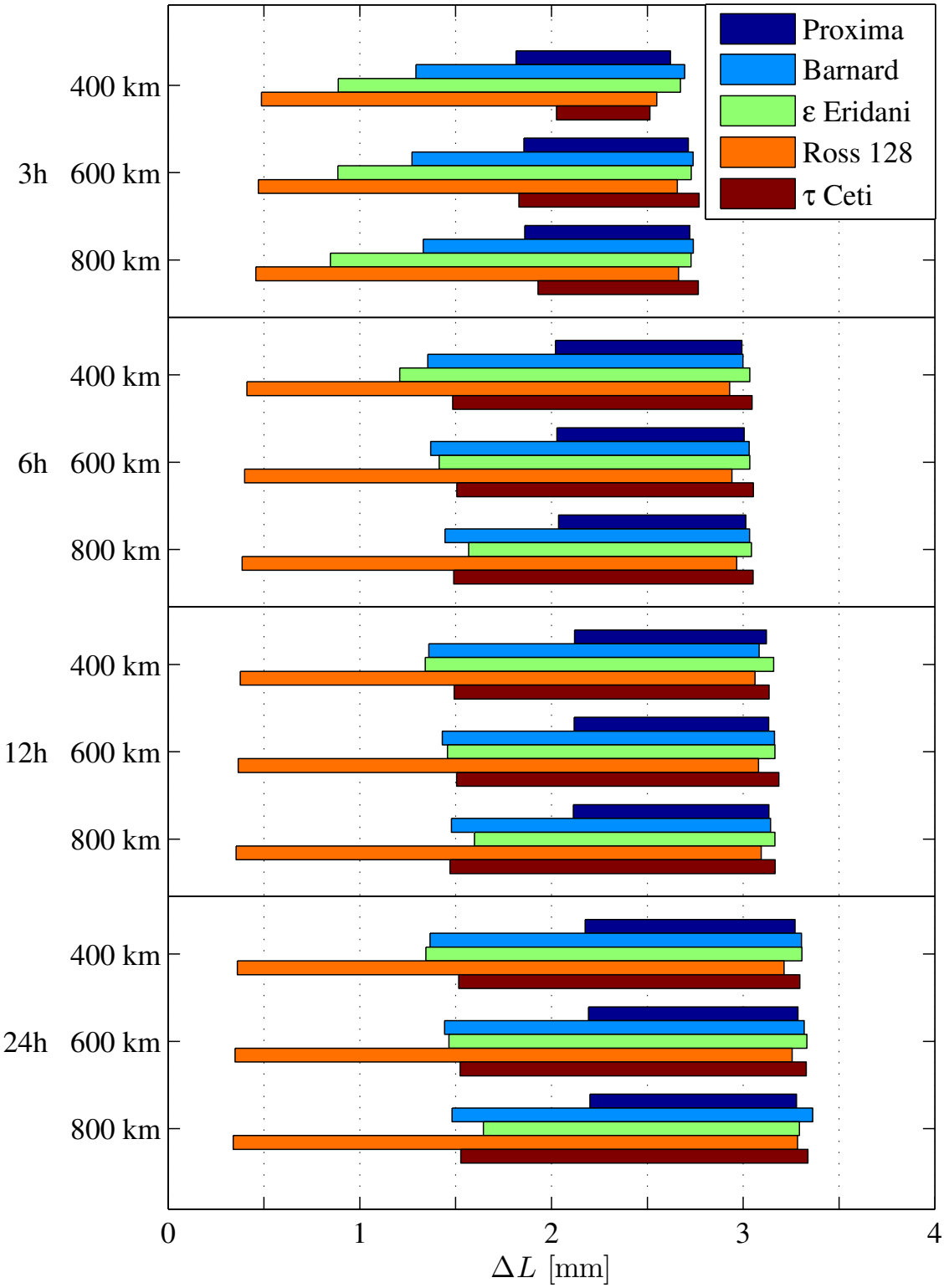

Figure 6.8: Elongation ranges estimation in 24h for 1/13h LTAN SSOs at different altitudes and for all selected spinning periods.

6.2.1 β angle discussion

It was decided to study SMILE orbits for different LTAN again. Contrariwise to the SSO, SMILE is a HEO having an orbital period of 54h (see Tab. 3.3) which is the longer of all selected orbits of this work. Comparing to SSOs, β profiles of SMILE orbits are much more varying over the year. This is depicted in Fig. 6.9. The LTAN are varying from 0h to 24h with a 4h step. The study of all of these orbits allows to cover a large part of possibilities field. The legend indicates the corresponding LTAN hour.

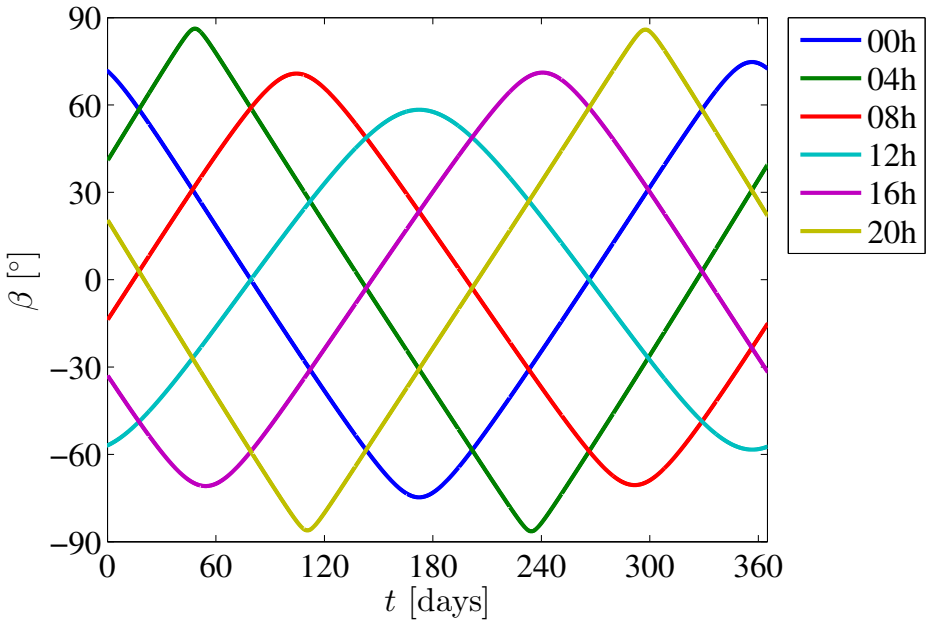

Figure 6.9: Distribution of β angles for SMILE orbits with different LTAN over the year. Legend indicates the LTAN hour.

Profiles are as a matter of fact highly variable over the year. In SSO case, their β distributions are varying but not crossing each others for the different LTAN. In this SMILE instance, all angle profiles are interweaving over the year. Moreover, they are all symmetric towards $\beta = 0°$. Some profiles are the same over the year, but just shifted on time. This is the case for 4h and 20h LTAN but also for 8h and 16h. In addition, the 12h LTAN is the one with the lowest maximum β angle. It could be sufficient to limit the SMILE study on only 4h, 12h and 20h LTAN due their extreme β values. However, some β can be at an extremum while Φ angle (see its distribution over the year in Fig. 5.20) can be weak at this time and conversely. This is why temperature ranges are computed for all selected LTAN. This will enable to be more aware on all range possibilities in each pointed star.

6.2.2 Influence on satellite's temperatures

The temperature ranges of SMILE orbit for all LTAN estimated over the year are given in Fig. 6.10 for Proxima star and in the appendix from Fig. 32 to Fig. 35

for other stars. In addition, the range of temperatures is given over one orbit and not one day, because the SMILE orbit period is longer than 24h.

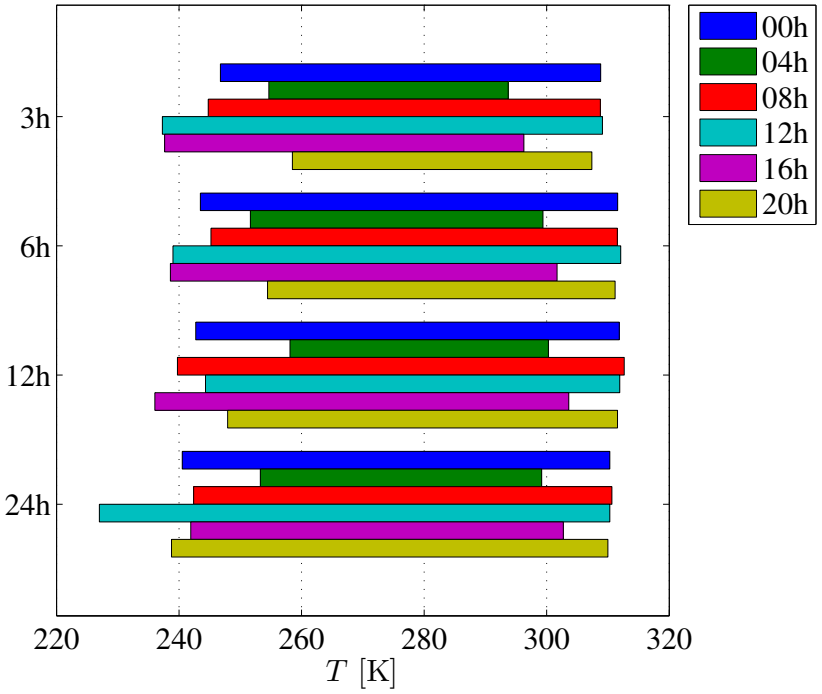

Figure 6.10: Temperature ranges of the satellite on SMILE with different LTAN over 2020 year for all selected spinning periods and pointing Proxima. Legend indicates the LTAN hour.

Once again, temperature seems to be sometimes too hazardous for 3h and 6h spinning period. This is the case when the pointed star is ϵ Eridani and τ Ceti. It would appear than some particular cases are too much frequent for those periods. On the other hand, ranges from 12h and 24h are in every case quite similar. Moreover, all the graphs are showing that temperature distributions are highly depending on the sighted star compared to the Sun and satellite position at the time when simulations are run. Indeed, the width of temperature ranges for all LTAN are different from a star to another. For instance, LTAN providing the same but shifted in time β distribution over the year (4h/20h and 8h/16h) involves different temperature ranges for a same pointed star. In fact, graphs allow to make a first choice on the desired LTAN, depending on the observed star and then on the temperature range needed by the satellite.

6.2.3 Corresponding elongations

Concerning the elongation, it has to be generally given over 24h because observations are done on a day. The elongation has then to be corrected before each observation. However, it does not change to compute the elongation over one entire SMILE orbit (54h). Indeed, its profile is periodic, which gives a same total elongation for 24h than for 54h. In the worst case, it can be modified by a maximum of

1%, which is negligible in this work. The elongation ranges are then displayed in Fig. 6.11 for all sighted stars and spinning periods.

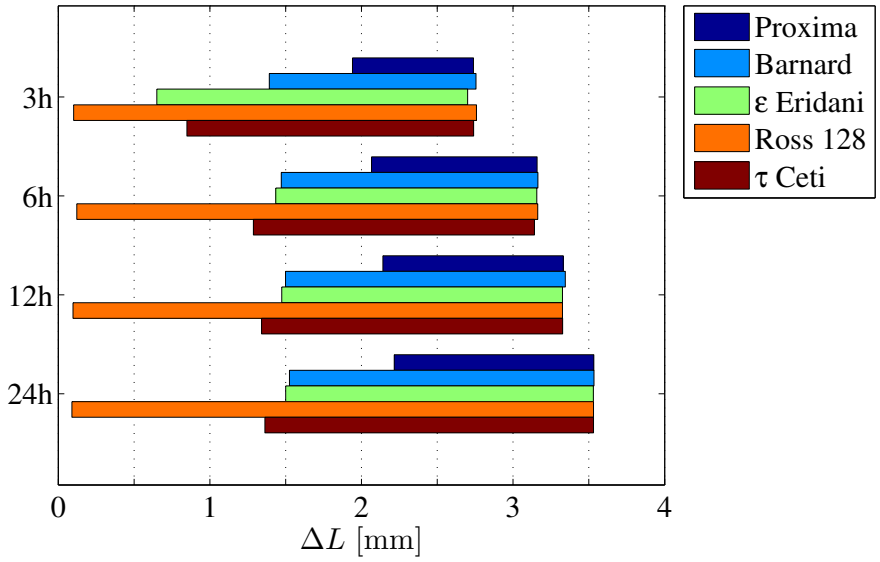

Figure 6.11: Elongation ranges estimation of the satellite on a SMILE orbit over 2020 year for all selected spinning periods.

Elongation ranges are directly generalized regardless LTAN variation because results are identical when pointing a star, or extremely close. This is due to the symmetric and periodic profile of β angle. Nevertheless, some sparse results coming from 3h and 6h spinning rotation pointing ϵ Eridani and τ Ceti are still present. They are not taken into account with the aim of achieving consistent results.

Nonetheless, it makes wondering if LTAN has an influence on the total elongation of the satellite under SMILE orbit since results are generalized. In fact, this is important to distinguish the temperature and elongation ranges. Indeed, the temperature range is the approximation of the coldest and the hottest temperature which could be reached during the year. On the other hand, the largest and smallest elongation are not especially computed at the same dates but when $\Phi = 90°$ or where it is extremum. Therefore, if elongation ranges from SMILE orbit are not significantly changing with a different LTAN, it is because the temperature difference between tip faces (where sub-pupils are located) is the same from a LTAN to another, at their corresponding computation date.

6.3 LEO results

All variations describing SSO and SMILE orbits are discussed. It is then possible to firstly present results from all selected Low Earth Orbits (LEOs). These are HUB, ISS, POL and SSO. As altitude and LTAN have been presented as a variable for SSO, the made choice is to represent the two LTAN cases of 1/13h and 7/19h because all other cases are included in their ranges. The selected altitude is 600 km

since it has been demonstrated that it does not influence significantly temperature and especially elongation ranges. This altitude is then more complementary to the other LEOs altitudes.

6.3.1 Temperature ranges

The temperature ranges of LEOs are then displayed in Fig. 6.12 for 3h and 6h spinning period around normal to $+X$ face, and in Fig. 6.13 for 12h and 24h, including all selected LEOs. Results have been computed for a 24h simulation and are given in each pointing star case. These figures are helping to be aware of the temperature behavior on satellite faces without any thermal control.

This time again, ranges obtained for $\tau_{spin} = 3$h are too much sporadic compared to results from other spinning periods. This is slightly the same problem for the 6h rotation period, but way less frequently than for 3h. For a same sighted star, some orbits provide colder temperatures than others and conversely. For example while pointing τ Ceti with $\tau_{spin} = 12$h, the estimated range induced by ISS orbit is [261; 327] K while it is [241; 313] K and [242; 310] K respectively for HUB and 7/19h LTAN SSO. Moreover, the width of these ranges can significantly change from one orbit to another. For instance, the corresponding range when pointing Barnard's star with $\tau_{spin} = 24$h is [236; 321] K for the POL orbit, then temperature is estimated to vary up to 85 K during the year. This represents around the double of the total variation of HUB orbit, and around two third more than the 7/19h LTAN SSO. Some similarities from different orbits can be observed because some are giving sensitively quite close results in each star case. Temperature ranges from HUB and 7/19h LTAN SSO or even ISS and POL are as a matter of fact inducing results with a similar order of magnitude. Furthermore, HUB, ISS and POL have no variable in their orbital elements description while SSO results are split for its two extreme LTAN cases. As a consequence, 7/19h LTAN SSO involves the coldest mean temperature while the hottest comes from 1/13h LTAN. For the reason that other orbits have their orbital elements from a real mission or from a visibility study,[13] their estimated mean range temperature is about to be included between the two selected SSOs.

6.3.2 Elongation ranges

In the same way, elongation ranges of LEOs appearing over the year are illustrated in Fig. 6.14 for 3h and 6h spinning period around the normal to $+X$ face, and in Fig. 6.15 for 12h and 24h. Maximum and minimum elongation have been computed for a 24h simulation. They are given in each pointing star case.

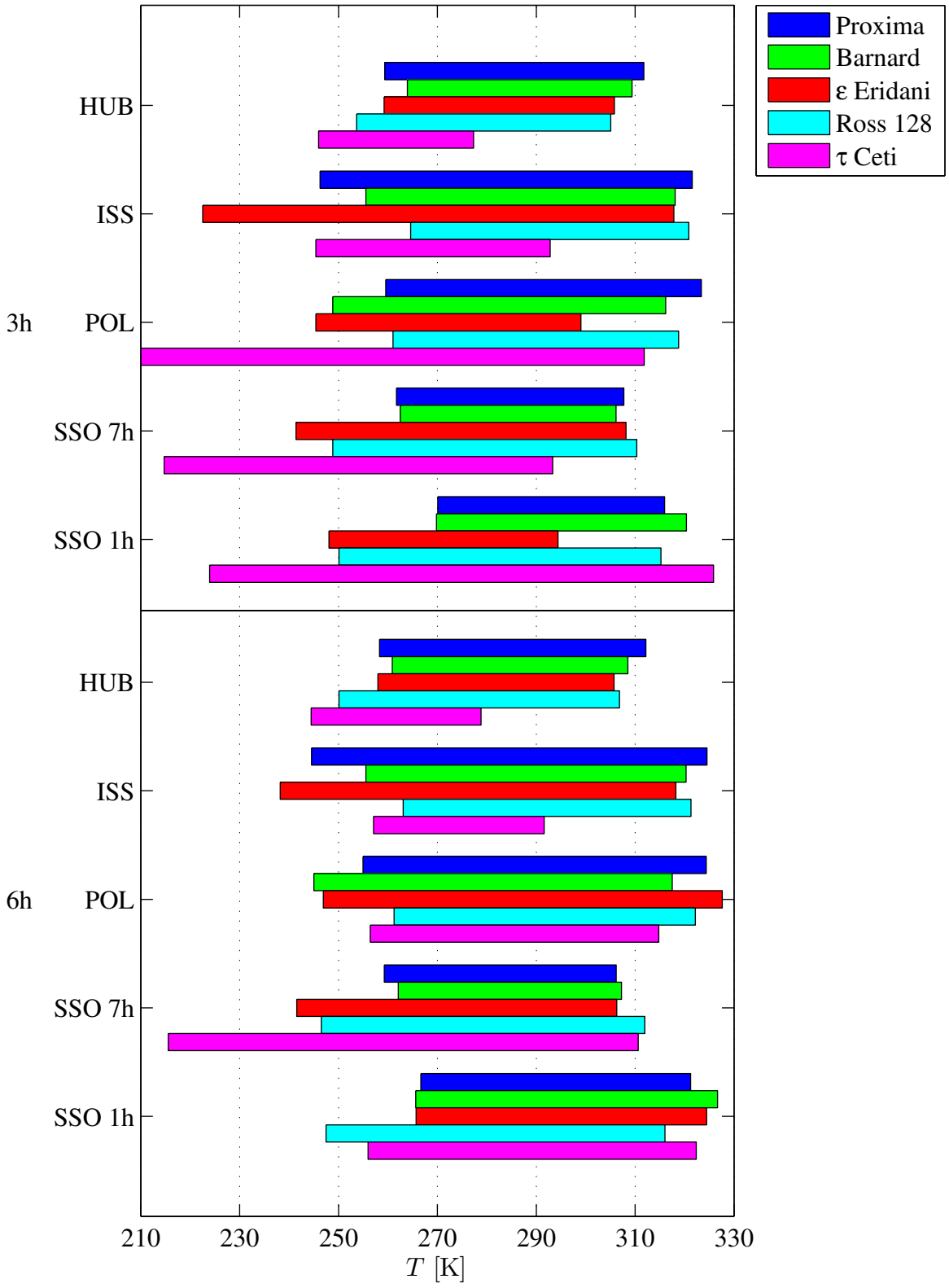

Figure 6.12: Estimated temperature ranges appearing in one day for selected LEOs in each pointed star case. Presented spinning rotations around normal to $+X$ face are 3h and 6h.

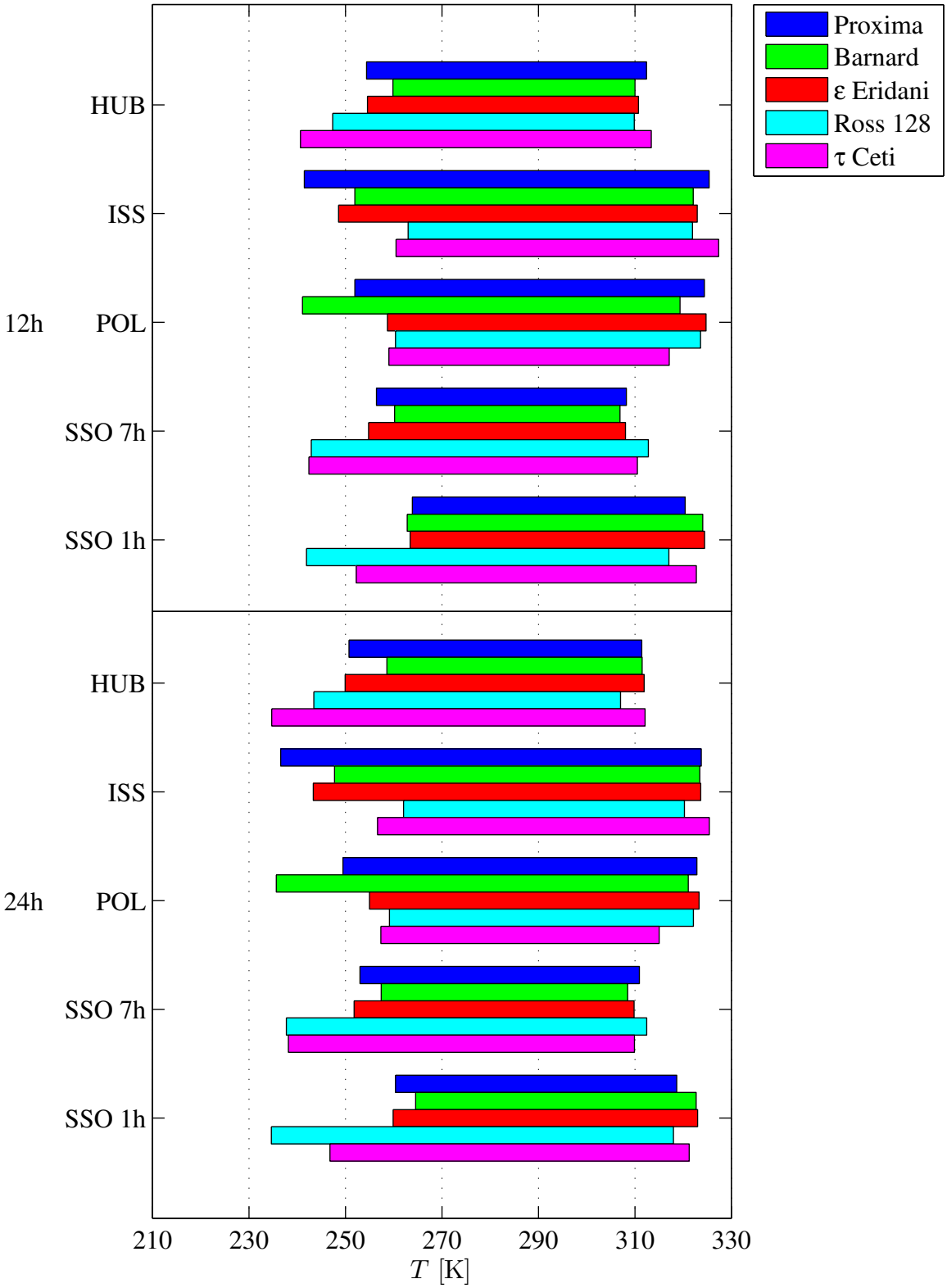

Figure 6.13: Estimated temperature ranges appearing in one day for selected LEOs in each pointed star case. Presented spinning rotations around the normal to $+X$ face are 12h and 24h.

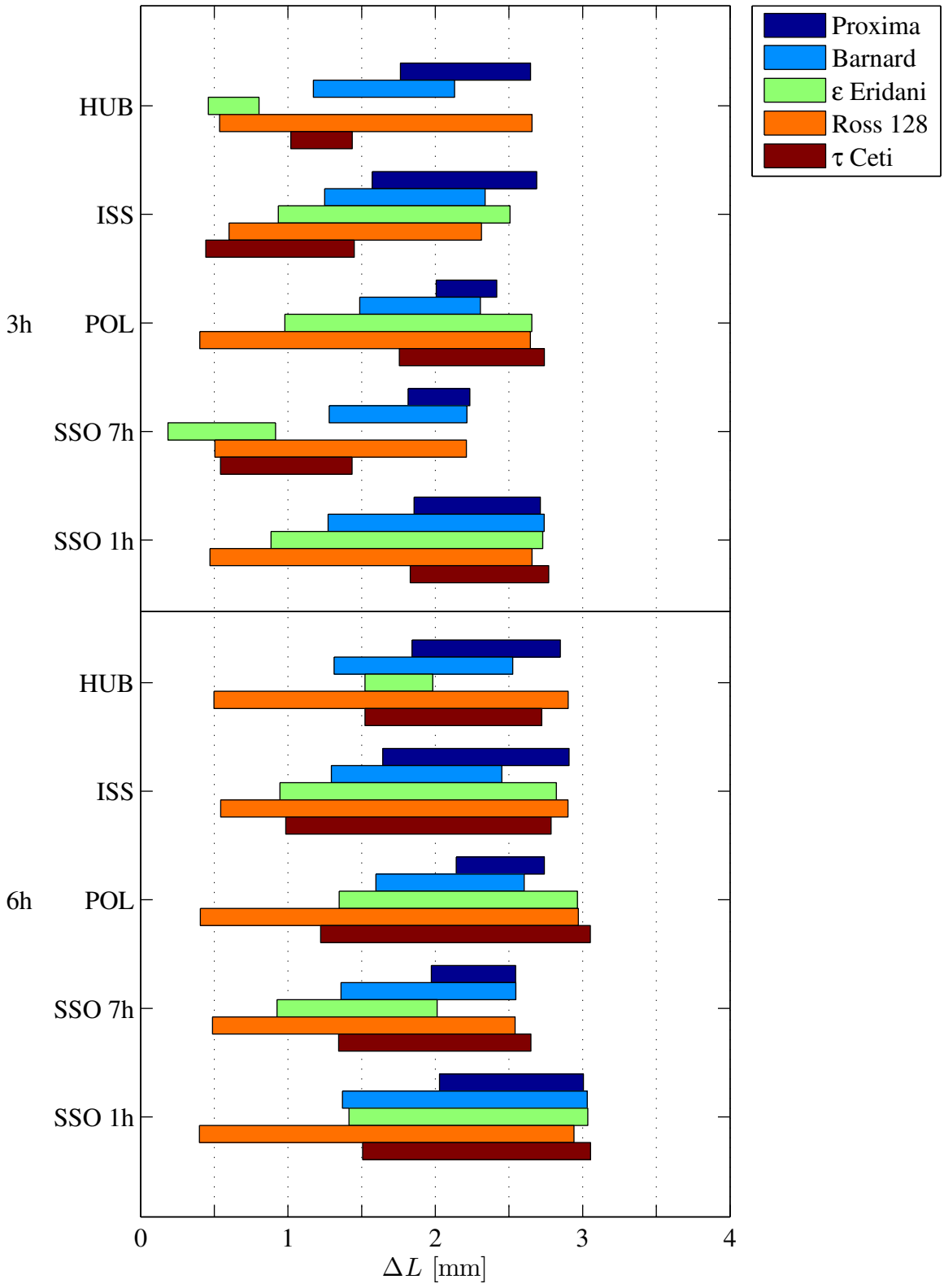

Figure 6.14: Estimated elongation ranges appearing in one day for selected LEOs in each pointed star case. Presented spinning rotations around the normal to $+X$ face are 3h and 6h.

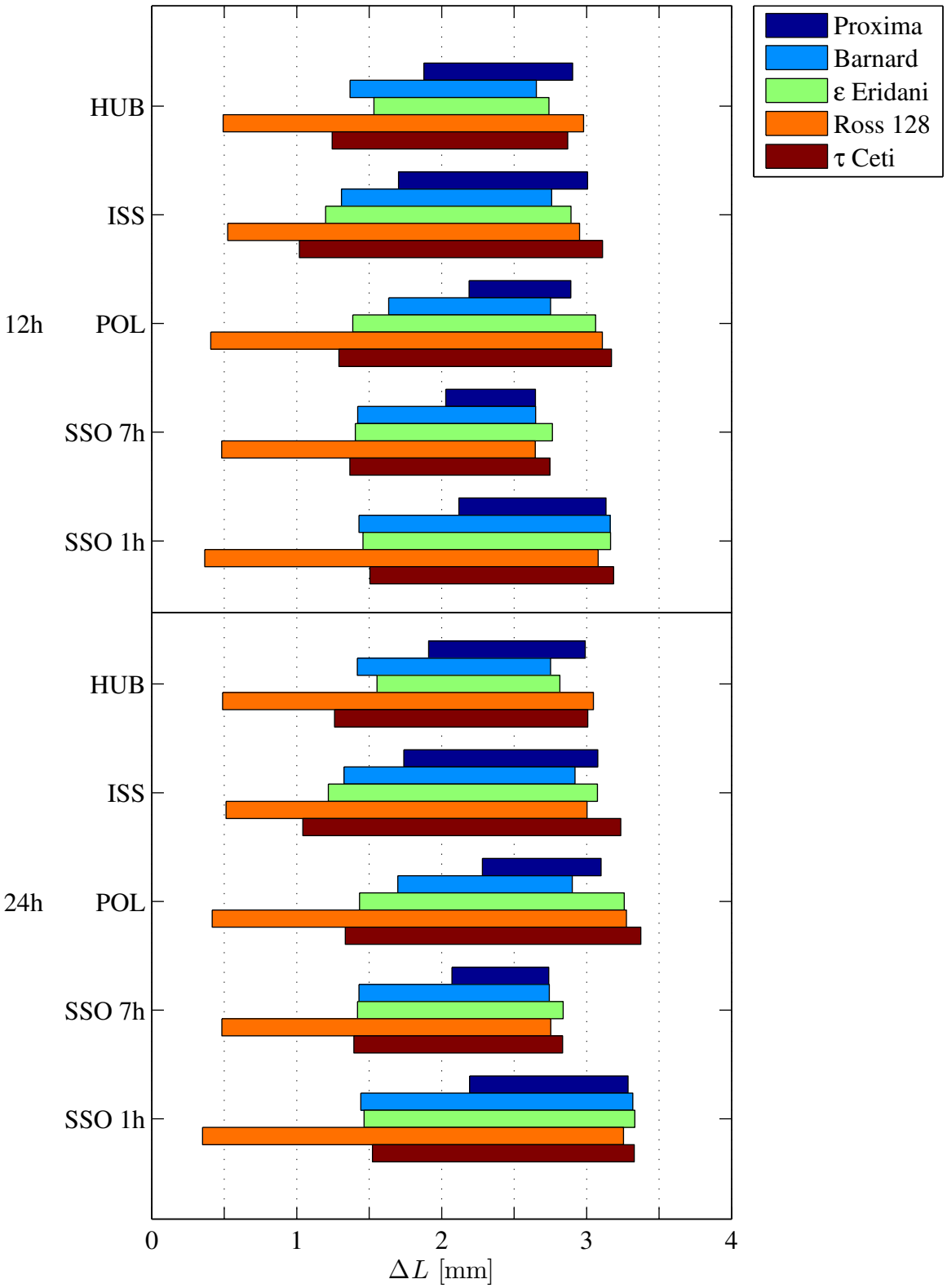

Figure 6.15: Estimated elongation ranges appearing in one day for selected LEOs in each pointed star case. Presented spinning rotations around the normal to $+X$ face are 12h and 24h.

Range results are still a too sporadic for the 3h rotation period, especially when pointing ϵ Eridani and τ Ceti. However, they give a first idea on the deformation for other stars. These sparse results are once again slightly present when $\tau_{spin} = 6$h pointing ϵ Eridani. Regardless of the orbit, this is always when having Proxima star in the line of sight that the difference between maximum and minimum elongation is the smallest. Contrariwise, the widest bandwidth is always obtained in the Ross 128 pointing star situation. Indeed, as shown in the Tab. 6.1, this is Proxima which has the smallest angle difference at its extremum with $\Phi = 90°$, while Ross 128 has the highest. One reminds that when the angle between the line of sight direction of the satellite and the Sun is orthogonal ($\Phi = 90°$), the elongation is maximal since the rotation around the normal to $+X$ face[13] involves that $+Y$, $+Z$, $-Y$ and $-Y$ are successively perfectly receiving direct Sun all over the face. The temperature difference between opposite Y faces is therefore higher and induces a larger deformation. On the other hand, more the extremum Φ value is remote from 90°, less the elongation will be important. The minimum elongation when pointing Ross 128 (around 0.5 mm) is finally due to its extremum Φ angle which is almost reaching 180° and 0° during the year (see Fig. 6.9).

In terms of elongation and without taking into account visibility challenges, the 7/19h LTAN SSO seems to be the more convenient orbit since its maximal elongation is the smallest in all star cases. The HUB orbit is an alternative because its maximal elongations are most of the time slightly longer that 7/19h SSO. Furthermore, ISS could also be convenient. Indeed, maximum elongations are not too much longer while more importantly, it involves the smallest elongations of all star cases. However, POL and 1/13h LTAN SSO are not yielding enough consistent results compared to other selected LEO orbits.

6.4 HEO and GEO results

This section presents the results from selected High Elliptical Orbits (HEOs) and the Geostationary Earth Orbit (GEO). These are GEO, GTO, MOL, XMM and SMILE. As the LTAN orbital parameter of SMILE orbit is variable, it was decided to select only two different LTAN for each star. This helps to not overload the graphs of this section.

6.4.1 Temperature ranges

The temperature ranges of these orbits are displayed in Fig. 6.16 for 3h and 6h spinning periods around the normal to $+X$ face and in Fig. 6.17 for 12h and 24h. Maximum and minimum temperatures have been computed for a 24h simulation when the rotation period around $+X$ normal is shorter than a complete day. Otherwise, these temperatures are computed for one complete orbit. The last remark concerns SMILE temperatures. As it was seen in Sec. 6.2, temperature ranges of SMILE orbits are varying with LTAN and the pointed star. Therefore, it has been

[13]Face which is pointing to the star

decided to only take two temperature ranges for each star. The selected LTAN are those providing the smallest and widest range. They are summed up in Tab. 6.2.

Star	LTAN: smallest range	LTAN: widest range
Proxima	04h	12h
Barnard's star	04h	12h
ϵ Eridani	04h	08h
Ross 128	20h	16h
τ Ceti	20h	08h

Table 6.2: Corresponding LTAN of SMILE orbit for the smallest and widest temperature range of each star.

Maximum temperatures are sensitively quite similar for all orbits and all stars from a rotation period of at least 12h. This maximum temperature averages 310 K. Results are again too sporadic for shorter spinning period around $+X$. Then, two behaviors are observed concerning the minimum estimated temperature. Indeed, GEO, GTO, XMM and SMILE 2[14] present the coldest minimum temperatures while MOL and SMILE 1[15] orbits have higher minimum values. From this, the orbit choice has to be done with regard to component requirements. If components have to operate at colder temperatures, then orbits involving the widest ranges and so colder minimum temperatures has to be chosen. On the other hand, if components have to operate in a narrow temperature range, MOL and SMI 1 should be more convenient due to their smallest ranges. However,there could require a more efficient cooling system.

6.4.2 Elongation ranges

In the same way than for temperatures, elongation ranges are given for all selected GEO and HEOs. They are represented in Fig. 6.14 for 3h and 6h rotation periods and in Fig. 6.19 for 12h and 24h in each pointing star case. As for temperatures, maximum and minimum elongations are computed for a 24h simulation in GTO and MOL orbits and for one complete orbital revolution in GEO, XMM and SMILE orbits. Elongations from SMILE are not presented for two LTAN cases anymore since those are generalized in one range per star. This is due to the lack of significant difference between distinct LTAN (see Sec. 6.2.3).

Contrary to elongations involved by LEOs, the corresponding estimated elongations when pointing a star are extremely similar from all selected HEOs and GEO, even when $\tau_{spin} = 3$h without taking into account ϵ Eridani and τ Ceti. Therefore, the choice of satellite orbit has not to be done according to elongation ranges. This is basically only if the final desired satellite orbit is HEO or GEO.

[14]LTAN involving widest ranges from SMILE orbit.
[15]LTAN involving smallest ranges from SMILE orbit.

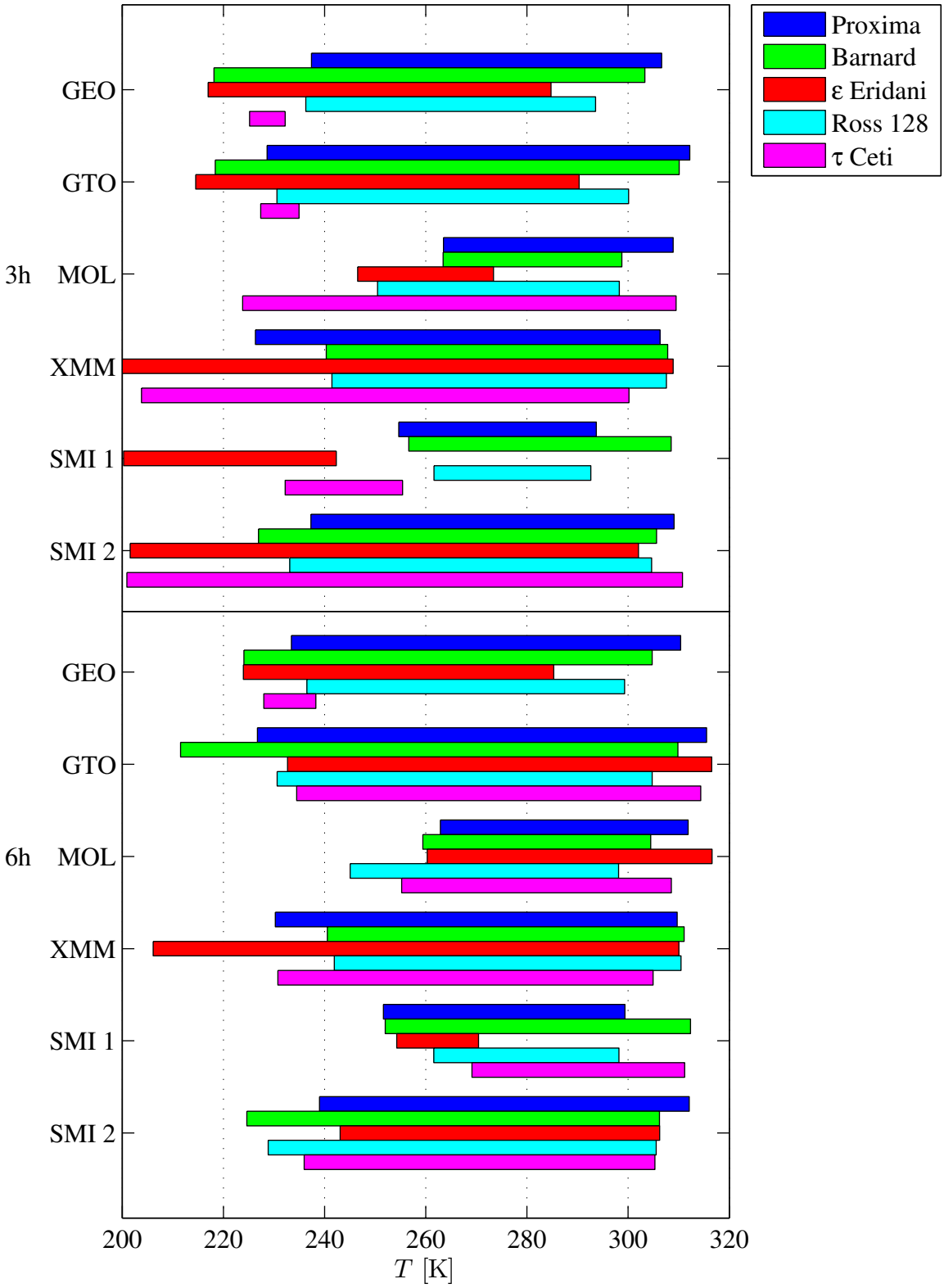

Figure 6.16: Estimated temperature ranges for selected GEO and HEOs in each pointed star case. Presented spinning rotations around the normal to $+X$ face are 3h and 6h.

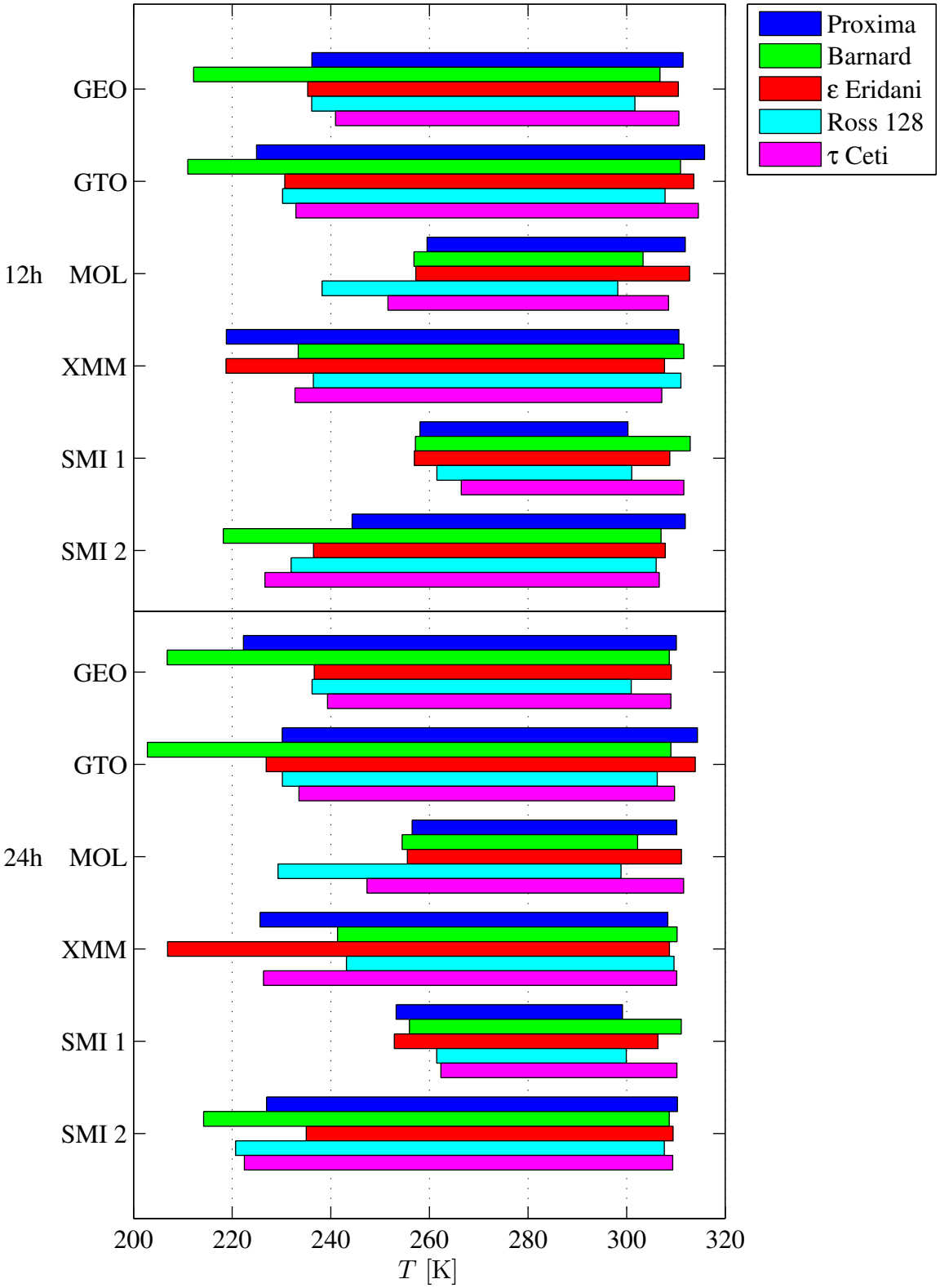

Figure 6.17: Estimated temperature ranges for selected GEO and HEOs in each pointed star case. Presented spinning rotations around the normal to $+X$ face are 12h and 24h.

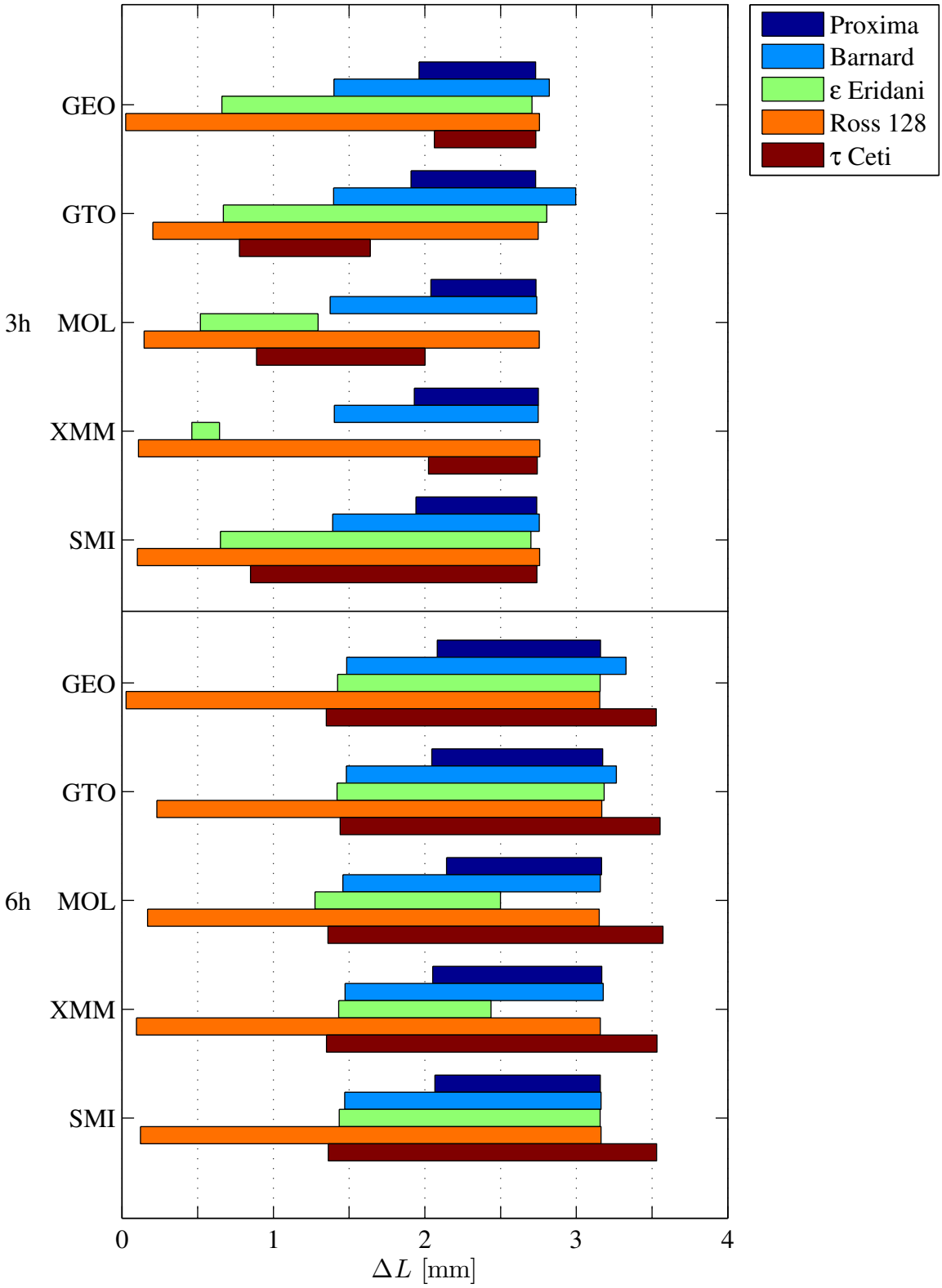

Figure 6.18: Estimated elongation ranges for selected GEO and HEOs in each pointed star case. Presented spinning rotations around the normal to $+X$ face are 3h and 6h.

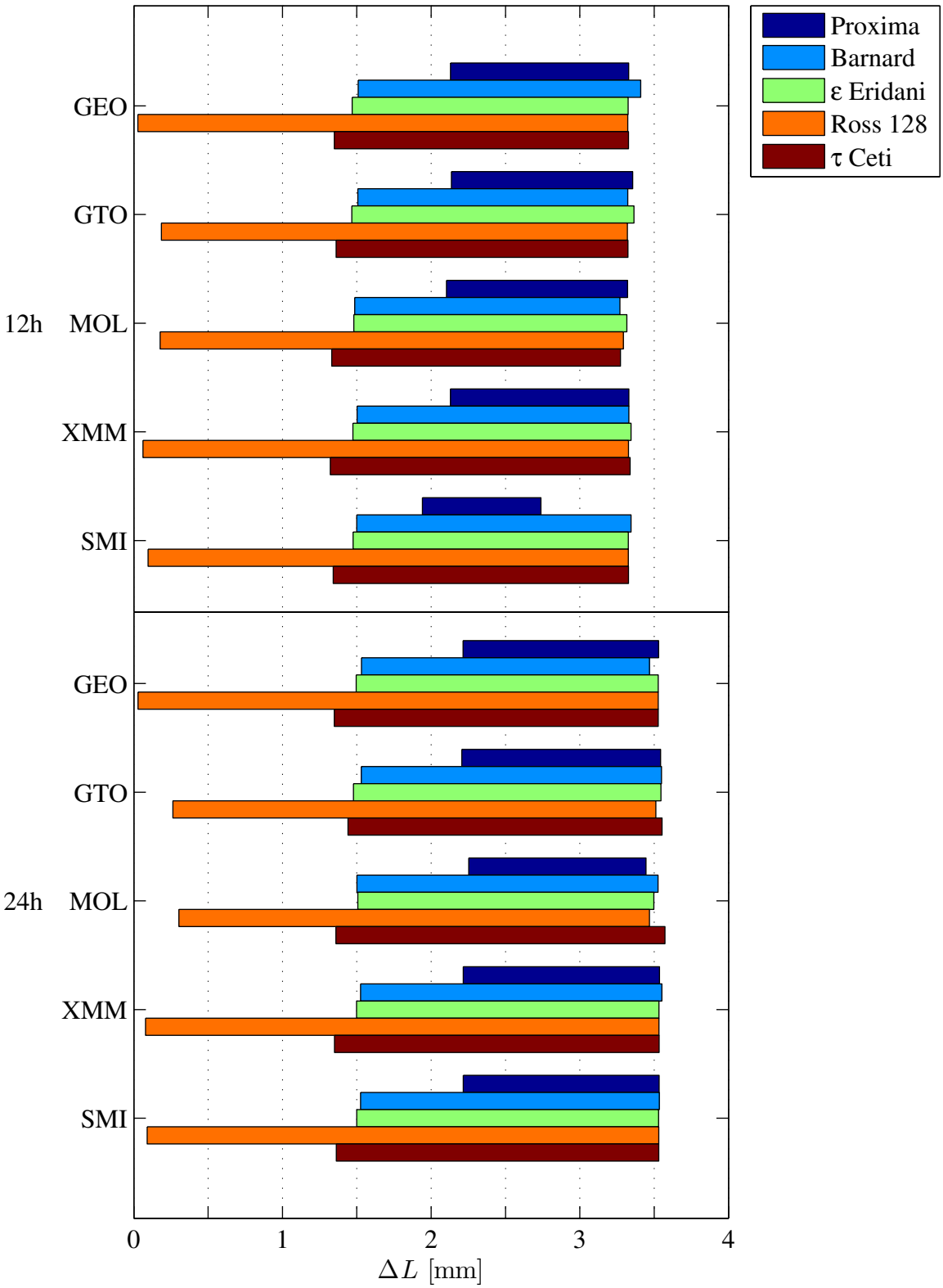

Figure 6.19: Estimated elongation ranges for selected GEO and HEOs in each pointed star case. Presented spinning rotations around the normal to $+X$ face are 12h and 24h.

6.5 Discussion

The satellite elongation lead to a decline in optical properties. Indeed, as shown in Fig. 1.3, the gathered light from the two sub-pupils located at each satellite extremity (near $+Y$ and $-Y$ faces) is recombinated in the center with a $+\pi$ dephasing in one of the arm linked to the telescope. Therefore, it allows the nulling interferometry process to take place and finally collect information on a possible exoplanet. However, a non homogeneous distance modification involves a decline in optical performances: the Optical Path Difference. In practice, each arm has to be measured in order to correct this OPD. This section is presenting some technical thermal controls propositions allowing to secure optical performances of the satellite.

First, optical components of a 12U Cubesat have to operate at around 150 K.[11] Any thermal control was used for results computation. However, even for orbits providing coldest temperatures, optical component have to be cooled. A thermal control is therefore essential in order to reach the ideal operating mode of optical components.

Temperatures has to be cooled as much as possible. In this purpose, a thermal control such a radiator to the deep space should be a convenient solution. Indeed, all heat transfers are done by conductivity through the radiator which finally expels the heat in the space environment in a radiative way. Then, both thermal conductivity and emissivity of this radiator have to be higher as possible. The corresponding sink of temperature is approximately equal to the average of radiative environment, but also to the radiative equilibrium temperature reached by the radiator when no heat load is applied (conductively decoupled).[30] Moreover, a great advantage is that a radiator to deep space enables to maintain instruments and electronic devices in a tight temperature range. This is highly important for space-based interferometry since lower is the temperature range, lower will be the corresponding elongation range. In addition, another improvement idea is suggested: the Peltier element. This method is unusual for a Cubesat since active thermal control techniques are much more expensive than a passive thermal control, and a main characteristic of Cubesat demonstrators is their cheap price. This method could be linked to the radiator if it is not enough powerful to cool components under their thermal requirements.

Secondly, the temperature has to remain sufficiently stable because otherwise, the OPD should be permanently corrected. Unfortunately, this is not possible to fix it during the observation time. The radiometric study have stated that the OPD should not exceed few tens of nm for an integration time of 24h.[11] Exceeding these theoretical value should involve a decline in detection properties. As a consequence, the interference fringes (see Fig. 1.4) will be diluted. The interferometry process should not working anymore since fringes cannot be identified. In that respect to avoid these problems, an isolation is unavoidable. Indeed, mirrors components have to be insulated from the structure. However, all components will have to be highly insulated from the structure since telescopes are located at each satellite extremity,

and have to be linked to recombine the light.

These solutions will have to be investigated in the future of this project. All results from all selected orbits and pointing to all selected stars are presented in this section. By choosing the ones providing the best temperature and elongation ranges (discussed in Sec. 6.3 for LEOs and in Sec. 6.4 for HEOs and GEO), the next study will have to concentrate all these results onto an optical consideration with existing optical components.

Conclusion

This Master's Thesis is a part of the development of a Small Sat demonstrator project conducted by the University of Liège. It aims to observe exoplanets using the space-based interferometry technique. The purpose of this work was to assess a first thermal analysis of the satellite. In addition, the mechanical consequences such as structure elongations have been deduced because they induce defects onto optical performances. The computational process is achieved on a 12U spacecraft pointing to five selected stars for a panel of nine various orbits. This thesis will provide several useful features to future project mission designers.

Essential processes and subjects are first presented and discussed in order to understand the operating mode and objectives of such a satellite based on the nulling interferometry. The main reasons of the choice on star and orbit panels studied all along the work are explained. The five star are in fact the nearest with at least one confirmed exoplanet, and the various orbits allow to cover a wide range of possibilities that could be encountered.

The satellite is then approximated in its environment by a thermal model. Two was studied: a single node and a six nodes model. As this is the first thermal study conducted on this spacecraft, the single node is necessary to obtain the general thermal behavior for each orbit. All the structure has therefore to be considered isothermal, but it show all influences that are involved by the thermal environment. It is mainly constituted of the direct solar radiation, the albedo and finally the Earth IR radiation. A first comparison is done, stating that HEOs and GEO orbits provide temperature ranges which are tighter and more stable that LEOs.

The advanced thermal model allow to obtain the temperature behavior of each face. All temperature distributions are following the expected profile given by the single node model. Faces variations are mainly explained by their orientation with the Sun, which is the more powerful heat source for each orbit. The whole process enabling to gather the lowest and highest temperatures as elongations is described. It includes the spin of the satellite around the star line of sight needed by the interferometry technique in order to detect the exoplanet signal, but also the dependence on two angles which are varying over time. Indeed, the β angle (between the Sun vector and its projection onto the orbital plane) allows to find the extreme temperature ranges. The Φ angle (between Sun and star vectors) enables to identify the extreme elongation ranges.

After that the computation process is applied on one orbit acting like a demonstrator, it is adapted to each selected orbit. It was decided to separate LEOs from HEOs and GEO analysis. The aim is to avoid a decline onto optical properties. Hence, the structure elongation has to be as small as possible, which corresponds to a tight range of temperature. For LEOs cases, smaller elongations are obtained when orbiting at SSO with 7/19h LTAN, but HUB and ISS gives also attractive results. However, the temperature range of ISS is too large compared to 7/19h SSO and HUB orbits. For HEOs and GEO cases, all elongation ranges are quite similar. Then, the advised orbit selection is conducted by temperature results. Depending on operating range of optical component requirements, SMILE and MOL orbits are providing tighter temperature ranges, but others ones have smaller minimum temperatures. A compromise choice has therefore to be done, depending in the future on the thermal control efficiency.

At this stage of the satellite development, recommended orbits are 7/19h LTAN SSO and HUB if LEO is chosen. Otherwise, SMILE or MOL orbit are advised.

Future prospects

The Small Sat to observe exoplanet based on interferometry is still in its early stage. The research study of this demonstrator project is subject to be completed within a few years. Indeed, a team composed of Jérôme Loicq, Denis Defrère and Colin Dandumont is working and assisting students through this challenging project, which could also join the Liège space missions program OUFTI.

As stated in the beginning, some stars are recently confirmed to have at least one exoplanet orbiting them. This work could then be completed by adding these stars into consideration.

The satellite platform configuration will have to be stated in order to process to a first iteration onto optical performances. Indeed, a thermal study exclusively focused on optics could be very useful and convenient to demonstrate the feasibility of such a spacecraft demonstrator. Once components will be known, a more complete research with an advanced thermal model composed of one node for each component should be relevant to consider.

Appendix

A View factors for three-dimensional geometries

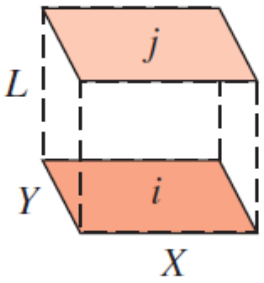

Figure 20: View factors for Three-Dimensional geometries: aligned parallel rectangles case.[27]

$$\begin{aligned}\bar{X} =& X/L, \bar{Y} = Y/L \\ F_{i,j} =& \frac{2}{\pi \bar{X}\bar{Y}} \left\{ \ln \left[\frac{\left(1+\bar{X}^2\right)\left(1+\bar{Y}^2\right)}{1+\bar{X}^2+\bar{Y}^2} \right]^{1/2} \right. \\ &+ \bar{X}\left(1+\bar{Y}^2\right)^{1/2} \tan^{-1} \frac{\bar{X}}{\left(1+\bar{Y}^2\right)^{1/2}} \\ &+ \bar{Y}\left(1+\bar{X}^2\right)^{1/2} \tan^{-1} \frac{\bar{Y}}{\left(1+\bar{X}^2\right)^{1/2}} \\ &\left. - \bar{X}\tan^{-1}\bar{X} - \bar{Y}\tan^{-1}\bar{Y} \right\}\end{aligned}$$

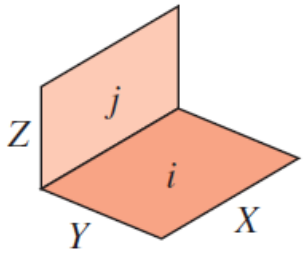

Figure 21: View factors for Three-Dimensional geometries: perpendicular rectangles with a common edge case.[27]

$$\begin{aligned}H =& Z/X, W = Y/X \\ F_{i,j} =& \frac{1}{\pi W} \left(W\tan^{-1}\frac{1}{W} + H\tan^{-1}\frac{1}{H} \right. \\ &- \left(H^2+W^2\right)^{1/2} \tan^{-1}\frac{1}{\left(H^2+W^2\right)^{1/2}} \\ &+ \frac{1}{4}\ln \left\{ \frac{\left(1+W^2\right)\left(1+H^2\right)}{1+W^2+H^2} \left[\frac{W^2\left(1+W^2+H^2\right)}{\left(1+W^2\right)\left(W^2+H^2\right)} \right]^{W^2} \right. \\ &\left. \left. \times \left[\frac{H^2\left(1+H^2+W^2\right)}{\left(1+H^2\right)\left(H^2+W^2\right)} \right]^{H^2} \right\} \right)\end{aligned}$$

B Temperature differences between faces: POL orbit

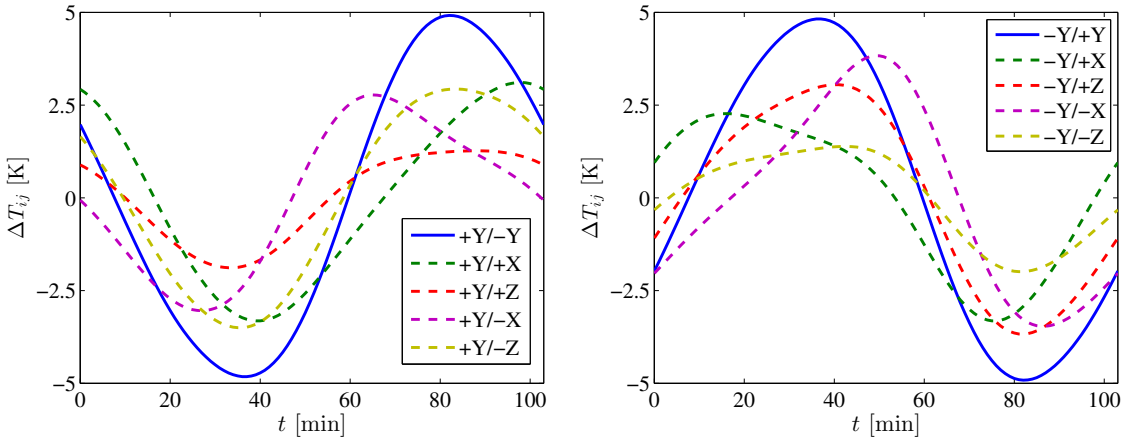

(a) Between $+Y$ and other faces. **(b)** Between $-Y$ and other faces.

Figure 22: Normalized temperature differences over one POL orbit pointing Proxima star. β angle is maximum.

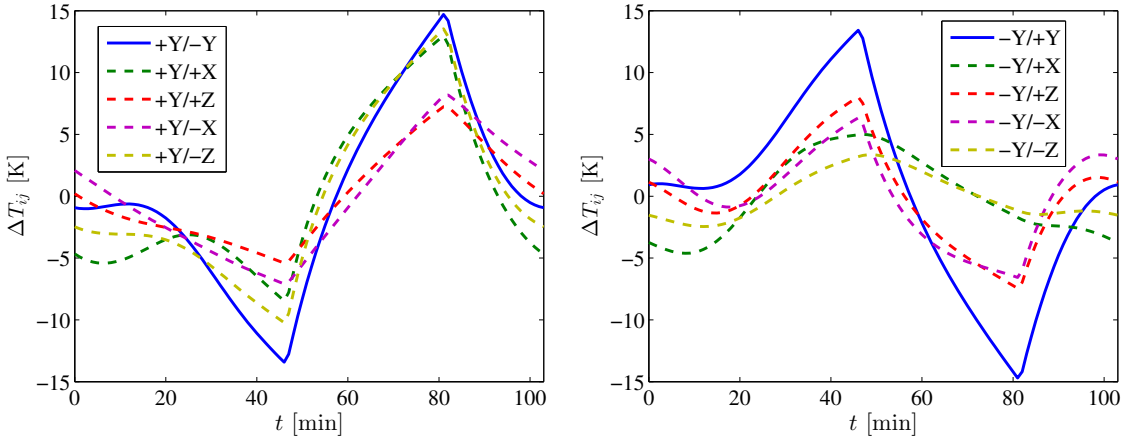

(a) Between $+Y$ and other faces. **(b)** Between $-Y$ and other faces.

Figure 23: Normalized temperature differences over one POL orbit pointing Proxima star. β angle is null.

C Relevant temperatures: POL orbit

Star	$\boldsymbol{\tau_{\text{spin}}}$	**case**	**Face**	$\boldsymbol{T_{\max}}$	$\boldsymbol{T_{\min}}$	$\boldsymbol{T_{\text{mean}}}$	$\lvert\dot{\boldsymbol{T}}\rvert_{\max}$	$\lvert\dot{\boldsymbol{T}}\rvert_{\text{mean}}$
				[K]	[K]	[K]	[K/min]	[K/min]
Barnard	3h	β max	$+Y$	312	282	295	0.75	0.28
			$-Y$	312	282	295	1.01	0.27
		$\beta = 0$	$+Y$	309	249	270	2.17	0.56
			$-Y$	305	249	270	2.31	0.56
	6h	β max	$+Y$	313	280	295	0.58	0.19
			$-Y$	314	280	295	0.49	0.19
		$\beta = 0$	$+Y$	308	245	271	2.27	0.49
			$-Y$	306	246	270	2.50	0.49
	12h	β max	$+Y$	311	278	294	1.30	0.14
			$-Y$	315	276	295	1.47	0.15
		$\beta = 0$	$+Y$	310	241	270	2.30	0.46
			$-Y$	308	244	269	2.72	0.47
	24h	β max	$+Y$	313	275	295	0.87	0.13
			$-Y$	313	275	295	1.38	0.13
		$\beta = 0$	$+Y$	309	237	269	2.54	0.45
			$-Y$	310	236	269	2.56	0.46
ϵ **Eridani**	3h	β max	$+Y$	322	277	296	1.24	0.45
			$-Y$	323	277	296	1.22	0.46
		$\beta = 0$	$+Y$	309	258	281	1.87	0.70
			$-Y$	278	245	254	0.62	0.24
	6h	β max	$+Y$	325	274	296	0.90	0.28
			$-Y$	324	274	296	0.83	0.28
		$\beta = 0$	$+Y$	307	261	278	1.66	0.44
			$-Y$	305	262	278	1.60	0.40
	12h	β max	$+Y$	323	269	296	1.96	0.18
			$-Y$	325	271	297	1.55	0.19
		$\beta = 0$	$+Y$	306	258	278	1.69	0.39
			$-Y$	304	260	278	1.69	0.39
	24h	β max	$+Y$	323	263	295	0.44	0.12
			$-Y$	324	262	295	0.44	0.12
		$\beta = 0$	$+Y$	307	254	278	1.70	0.39
			$-Y$	305	255	278	1.68	0.38

Table 3: Summary of relevant temperature values on $+Y$ and $-Y$ faces. Barnard's star and ϵ Eridani, all spinning periods τ_{spin}, the two β angle cases, one day simulation.

Star	$\tau_{\mathbf{spin}}$	**case**	**Face**	$T_{\mathbf{max}}$	$T_{\mathbf{min}}$	$T_{\mathbf{mean}}$	$\lvert\dot{T}\rvert_{\max}$	$\lvert\dot{T}\rvert_{\mathrm{mean}}$
				[K]	[K]	[K]	[K/min]	[K/min]
Ross 128	3h	β max	$+Y$	318	271	291	1.36	0.49
			$-Y$	323	271	292	1.36	0.50
		$\beta = 0$	$+Y$	286	261	272	0.60	0.28
			$-Y$	286	261	272	0.62	0.29
	6h	β max	$+Y$	322	268	291	0.95	0.30
			$-Y$	324	268	291	1.01	0.30
		$\beta = 0$	$+Y$	286	261	272	0.66	0.27
			$-Y$	286	262	272	0.83	0.28
	12h	β max	$+Y$	324	262	290	0.78	0.19
			$-Y$	322	262	291	1.34	0.20
		$\beta = 0$	$+Y$	287	261	272	0.73	0.27
			$-Y$	285	261	272	0.65	0.27
	24h	β max	$+Y$	322	254	291	2.58	0.15
			$-Y$	322	254	292	1.28	0.13
		$\beta = 0$	$+Y$	286	259	272	0.68	0.27
			$-Y$	285	260	272	0.69	0.27
τ **Ceti**	3h	β max	$+Y$	316	259	282	1.42	0.54
			$-Y$	314	259	282	1.39	0.55
		$\beta = 0$	$+Y$	282	254	263	0.65	0.28
			$-Y$	315	261	294	2.57	0.87
	6h	β max	$+Y$	318	255	282	1.02	0.32
			$-Y$	316	256	282	0.98	0.33
		$\beta = 0$	$+Y$	292	261	275	0.95	0.32
			$-Y$	294	261	275	1.36	0.34
	12h	β max	$+Y$	316	249	281	2.17	0.14
			$-Y$	318	251	283	1.69	0.21
		$\beta = 0$	$+Y$	293	260	275	1.01	0.32
			$-Y$	294	260	275	1.10	0.32
	24h	β max	$+Y$	315	241	280	0.50	0.12
			$-Y$	316	239	280	0.61	0.13
		$\beta = 0$	$+Y$	293	257	275	1.10	0.32
			$-Y$	292	258	275	1.09	0.32

Table 4: Summary of relevant temperature values on $+Y$ and $-Y$ faces. Ross 128 and τ Ceti, all spinning periods τ_{spin}, the two β angle cases, one day simulation.

D Face temperature ranges: 600 km SSOs

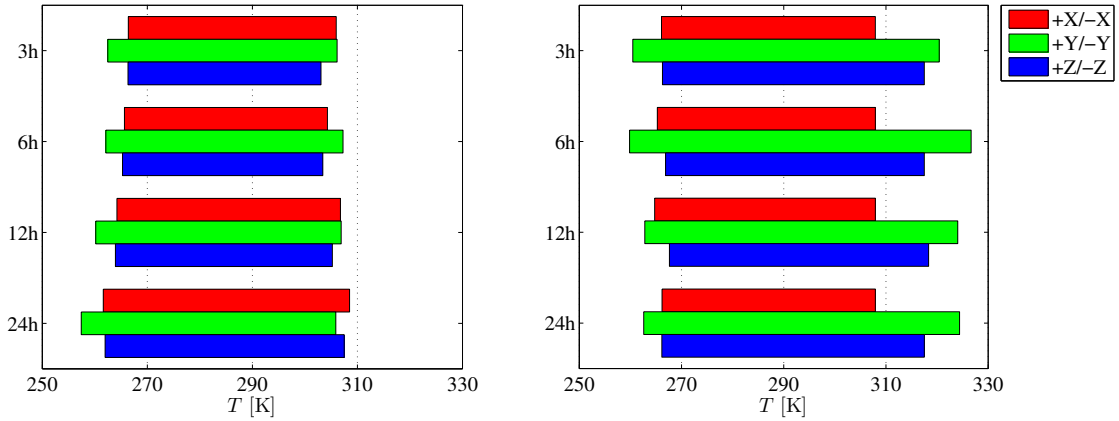

(a) 7/19h LTAN. **(b)** 1/13h LTAN.

Figure 24: Faces temperature ranges of the two studied extreme 600 km SSOs over 2020 year, pointing Barnard's star.

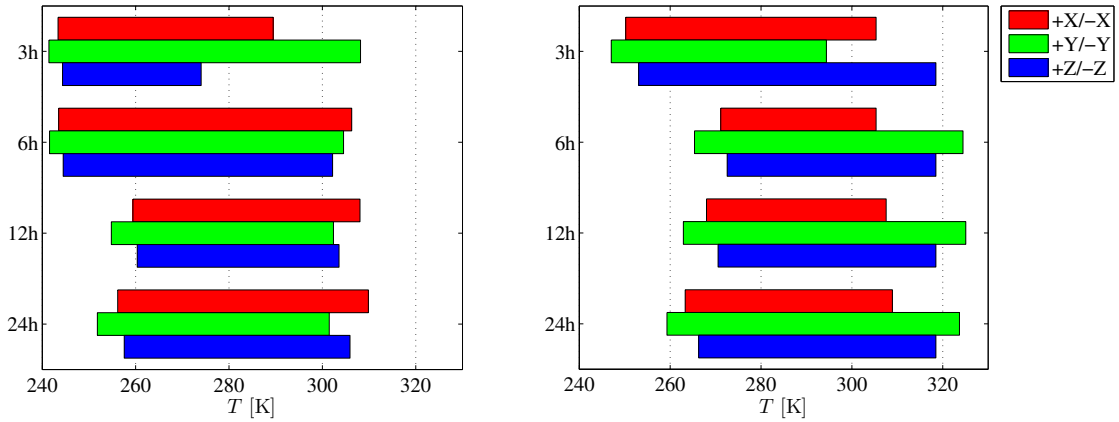

(a) 7/19h LTAN. **(b)** 1/13h LTAN.

Figure 25: Faces temperature ranges of the two studied extreme 600 km SSOs over 2020 year, pointing Epsilon Eridani.

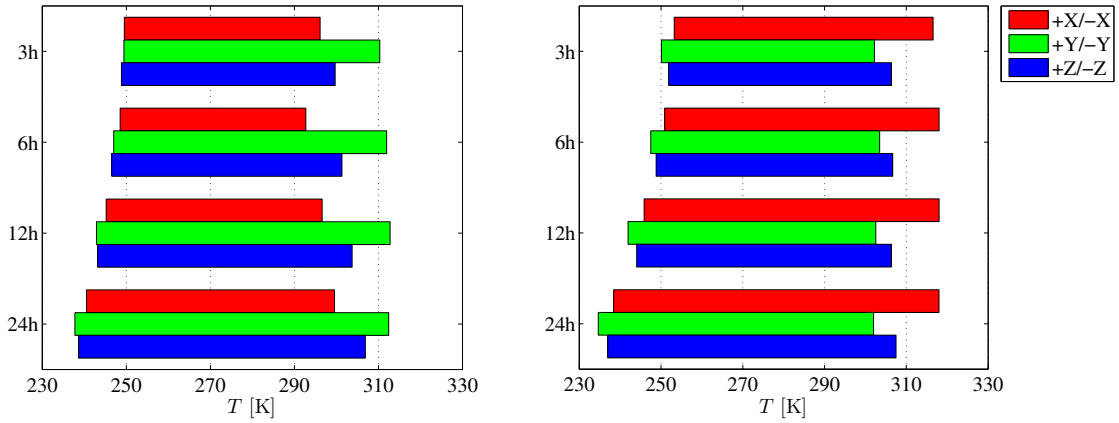

(a) 7/19h LTAN. **(b)** 1/13h LTAN.

Figure 26: Faces temperature ranges of the two studied extreme 600 km SSOs over 2020 year, pointing Ross 128.

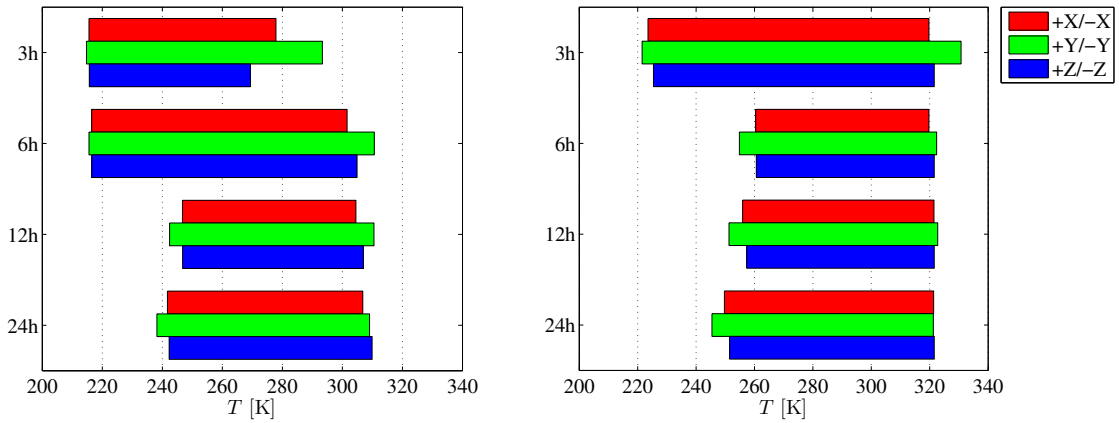

(a) 7/19h LTAN. **(b)** 1/13h LTAN.

Figure 27: Faces temperature ranges of the two studied extreme 600 km SSOs over 2020 year, pointing Tau Ceti.

E Temperature ranges for different SSOs altitudes

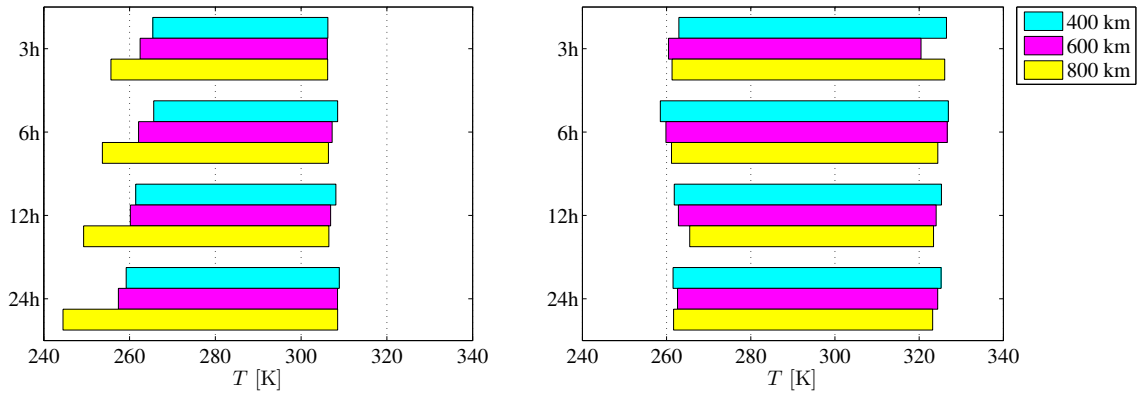

(a) 7/19h LTAN. **(b)** 1/13h LTAN.

Figure 28: Temperature ranges of the satellite for different altitudes SSOs over 2020 year. Two extreme LTAN cases are represented for all selected spinning periods and pointing Barnard's star.

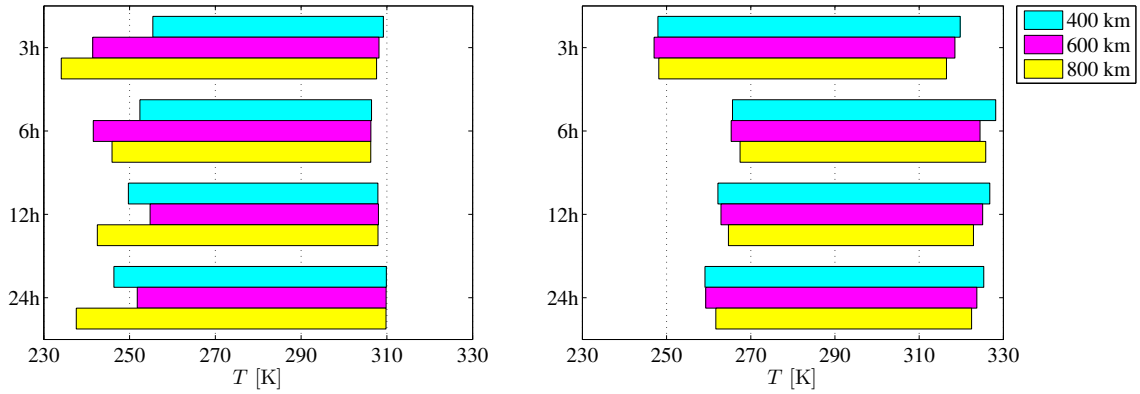

(a) 7/19h LTAN. **(b)** 1/13h LTAN.

Figure 29: Temperature ranges of the satellite for different altitudes SSOs over 2020 year. Two extreme LTAN cases are represented for all selected spinning periods and pointing ϵ Eridani.

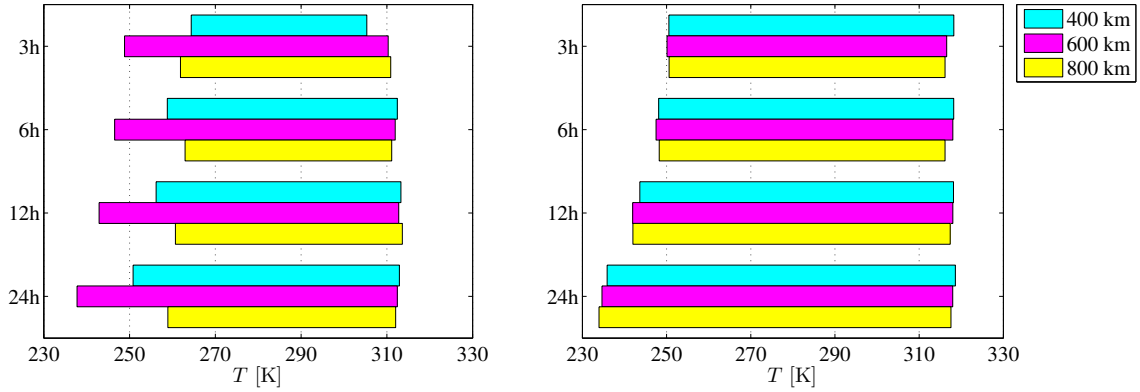

(a) 7/19h LTAN. **(b)** 1/13h LTAN.

Figure 30: Temperature ranges of the satellite for different altitudes SSOs over 2020 year. Two extreme LTAN cases are represented for all selected spinning periods and pointing Ross 128.

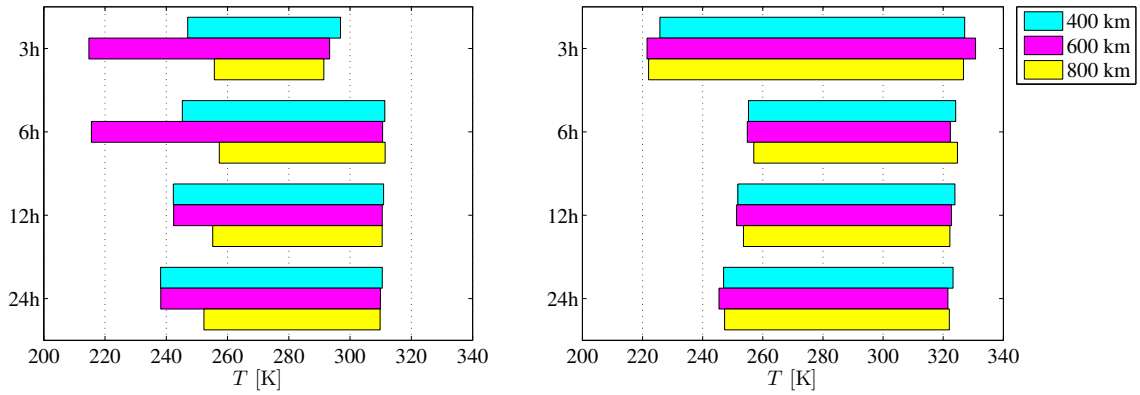

(a) 7/19h LTAN. **(b)** 1/13h LTAN.

Figure 31: Temperature ranges of the satellite for different altitudes SSOs over 2020 year. Two extreme LTAN cases are represented for all selected spinning periods and pointing τ Ceti.

F SMILE temperature ranges with various LTAN

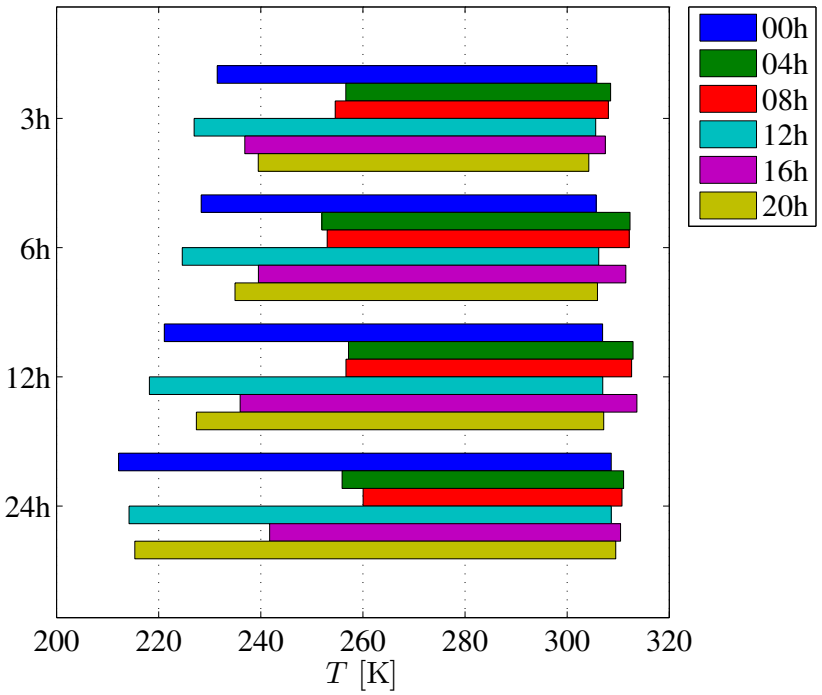

Figure 32: Temperature ranges of the satellite on SMILE with different LTAN over 2020 year for all selected spinning periods and pointing Barnard's star. Legend indicates the LTAN hour.

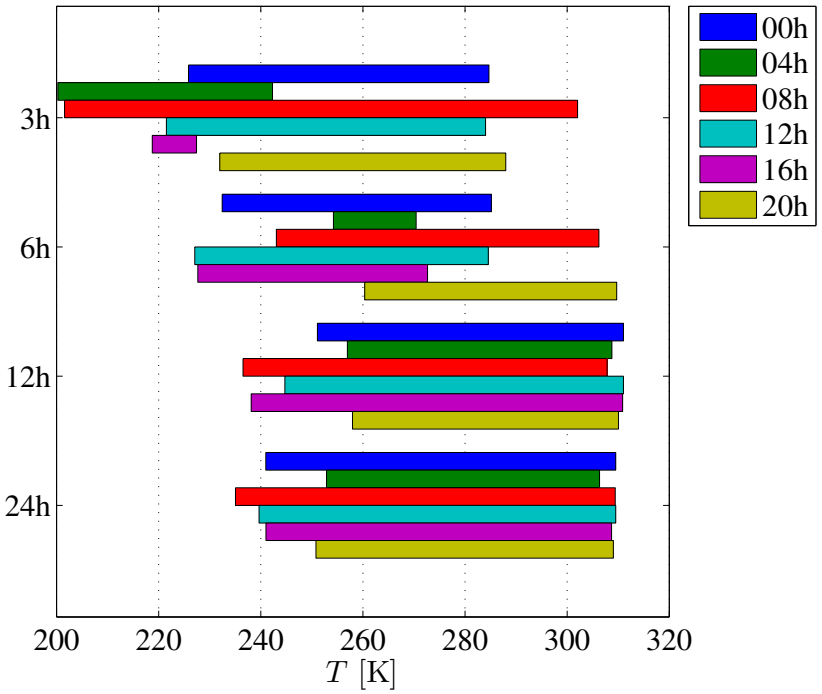

Figure 33: Temperature ranges of the satellite on SMILE with different LTAN over 2020 year for all selected spinning periods and pointing ϵ Eridani. Legend indicates the LTAN hour.

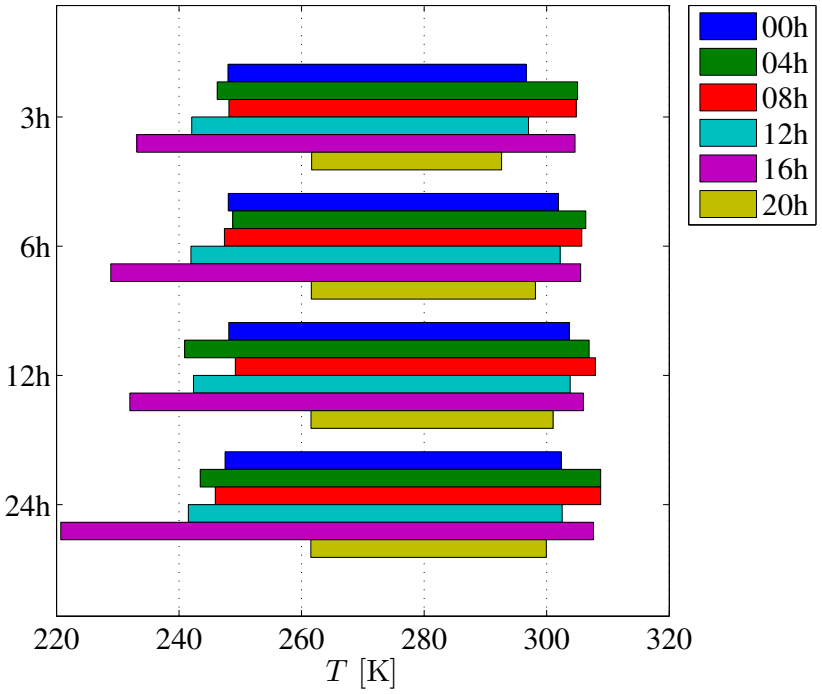

Figure 34: Temperature ranges of the satellite on SMILE with different LTAN over 2020 year for all selected spinning periods and pointing Ross 128. Legend indicates the LTAN hour.

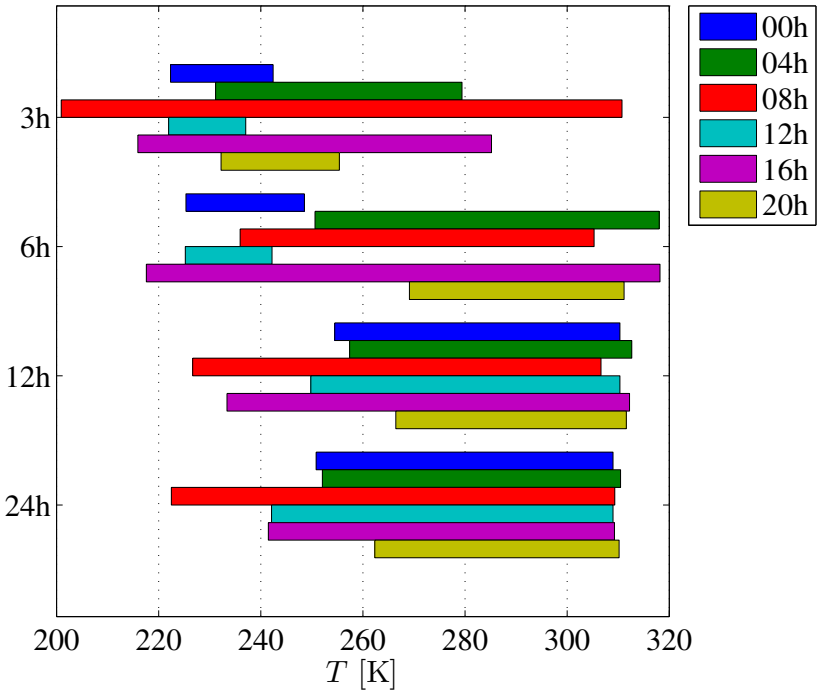

Figure 35: Temperature ranges of the satellite on SMILE with different LTAN over 2020 year for all selected spinning periods and pointing τ Ceti. Legend indicates the LTAN hour.

Bibliography

[1] *30 seconds summary*. en-US. Library Catalog: www.life-space-mission.com. URL: https://www.life-space-mission.com/the-project/ (visited on 06/07/2020).

[2] *Exoplanet and Candidate Statitics*. URL: https://exoplanetarchive.ipac.caltech.edu/docs/counts_detail.html (visited on 05/18/2020).

[3] *Pre-generated Exoplanet Plots*. URL: https://exoplanetarchive.ipac.caltech.edu/exoplanetplots/ (visited on 05/18/2020).

[4] C. Lovis et al. "Atmospheric characterization of Proxima b by coupling the SPHERE high-contrast imager to the ESPRESSO spectrograph". en. In: *Astronomy & Astrophysics* 599 (Mar. 2017), A16. ISSN: 0004-6361, 1432-0746. DOI: 10.1051/0004-6361/201629682.

[5] *Pouvoir de résolution*. fr. Page Version ID: 171041308. May 2020. URL: https://fr.wikipedia.org/w/index.php?title=Pouvoir_de_r%C3%A9solution&oldid=171041308 (visited on 06/04/2020).

[6] Jean Surdej. "Introduction to optical/IR interferometry". en. In: (), p. 39.

[7] R. N. Bracewell. "Detecting nonsolar planets by spinning infrared interferometer". en. In: *Nature* 274.5673 (Aug. 1978). Number: 5673 Publisher: Nature Publishing Group, pp. 780–781. ISSN: 1476-4687. DOI: 10.1038/274780a0. (Visited on 06/04/2020).

[8] Colin Dandumont. "Feasibility study of an interferometric CubeSat for exoplanet science". en. In: (), p. 33.

[9] D. Defrère et al. "Nulling interferometry: impact of exozodiacal clouds on the performance of future life-finding space missions". en. In: *Astronomy and Astrophysics* 509 (Jan. 2010), A9. ISSN: 0004-6361, 1432-0746. DOI: 10.1051/0004-6361/200912973. URL: http://www.aanda.org/10.1051/0004-6361/200912973 (visited on 05/21/2020).

[10] D. Defrère et al. "Space-based infrared interferometry to study exoplanetary atmospheres". en. In: *Experimental Astronomy* 46.3 (Dec. 2018). arXiv: 1801.04150, pp. 543–560. ISSN: 0922-6435, 1572-9508. DOI: 10.1007/s10686-018-9613-2. URL: http://arxiv.org/abs/1801.04150 (visited on 05/21/2020).

[11] Colin Dandumont et al. "1 Exoplanet detection yield of a space-based Bracewell interferometer, 2 from nano- to medium-satellites". en. In: (), p. 36.

[12] D Defrere, O Absil, and C Beichman. "Interferometric Space Missions for Exoplanet Science: Legacy of Darwin/TPF". en. In: (), p. 20.

[13] Di Bartolomeo. "Master thesis : Mission analysis of an interferometric smallSat to observe exoplanets". en. In: (), p. 96.

[14] *Home*. en-US. Library Catalog: www.life-space-mission.com. URL: https://www.life-space-mission.com/ (visited on 05/19/2020).

[15] Sascha P. Quanz et al. "Atmospheric characterization of terrestrial exoplanets in the mid-infrared: biosignatures, habitability & diversity". In: *arXiv:1908.01316 [astro-ph]* (Aug. 2019). arXiv: 1908.01316. URL: http://arxiv.org/abs/1908.01316 (visited on 06/04/2020).

[16] S Duijsens. "Master thesis : Cubesat deployment". en. In: (), p. 81.

[17] Z Mansoor. "Development of a deployable arm to hold mirrors for space interferometric instrument". en. In: (), p. 91.

[18] L Schifano. "Développement d'un interféromètre spatial pour la détection et la caractérisation d'exoplanètes". fr. In: (), p. 106.

[19] Guillem Anglada-Escudé et al. "A terrestrial planet candidate in a temperate orbit around Proxima Centauri". In: *Nature* 536.7617 (Aug. 2016). arXiv: 1609.03449, pp. 437–440. ISSN: 0028-0836, 1476-4687. DOI: 10.1038/nature19106. URL: http://arxiv.org/abs/1609.03449 (visited on 05/20/2020).

[20] I. Ribas et al. "A candidate super-Earth planet orbiting near the snow line of Barnard's star". In: *Nature* 563.7731 (Nov. 2018). arXiv: 1811.05955, pp. 365–368. ISSN: 0028-0836, 1476-4687. DOI: 10.1038/s41586-018-0677-y. URL: http://arxiv.org/abs/1811.05955 (visited on 05/20/2020).

[21] Artie P Hatzes et al. "EVIDENCE FOR A LONG-PERIOD PLANET ORBITING e ERIDANI". en. In: 544 (), p. 4.

[22] D. Backman et al. "EPSILON ERIDANI'S PLANETARY DEBRIS DISK: STRUCTURE AND DYNAMICS BASED ON *SPITZER* AND CALTECH SUBMILLIMETER OBSERVATORY OBSERVATIONS". en. In: *The Astrophysical Journal* 690.2 (Jan. 2009), pp. 1522–1538. ISSN: 0004-637X, 1538-4357. DOI: 10.1088/0004-637X/690/2/1522. URL: https://iopscience.iop.org/article/10.1088/0004-637X/690/2/1522 (visited on 05/21/2020).

[23] information@eso.org. *Découverte, à très grande proximité du Système Solaire, d'un monde tempéré autour d'une étoile calme - L'instrument HARPS de l'ESO a découvert une exoplanète de type Terre autour de Ross 128*. fr-be. Library Catalog: www.eso.org. URL: https://www.eso.org/public/belgium-fr/news/eso1736/ (visited on 05/21/2020).

[24] Mikko Tuomi et al. "Signals embedded in the radial velocity noise. Periodic variations in the tau Ceti velocities". en. In: *Astronomy & Astrophysics* 551 (Mar. 2013). arXiv: 1212.4277, A79. ISSN: 0004-6361, 1432-0746. DOI: 10.1051/0004-6361/201220509. URL: http://arxiv.org/abs/1212.4277 (visited on 05/21/2020).

[25] Fabo Feng et al. "Color difference makes a difference: four planet candidates around tau Ceti". en. In: *The Astronomical Journal* 154.4 (Sept. 2017). arXiv: 1708.02051, p. 135. ISSN: 1538-3881. DOI: 10.3847/1538-3881/aa83b4. URL: http://arxiv.org/abs/1708.02051 (visited on 05/21/2020).

[26] M. Tuomi et al. "Frequency of planets orbiting M dwarfs in the Solar neighbourhood". en. In: *arXiv:1906.04644 [astro-ph]* (July 2019). arXiv: 1906.04644. URL: http://arxiv.org/abs/1906.04644 (visited on 06/08/2020).

[27] Frank P. Incropera, ed. *Fundamentals of heat and mass transfer*. en. 7th ed. Hoboken, NJ: Wiley, 2011. ISBN: 978-0-470-50197-9.

[28] L Salvador and Pr Jérôme Loicq. "Chapter 4: Thermal Control". en. In: (), p. 145.

[29] *2.4.3 Gebhart method | DSPE, your portal for precision engineering*. URL: https://www.dspe.nl/knowledge-base/thermomechanics/chapter-2---in-depth/2-4-thermal-radiation/2-4-3-gebhart-method/ (visited on 06/04/2020).

[30] Lionel Jacques. "Spacecraft Thermal Control". en. In: (), p. 122.

[31] Dominic Ford. *Orbital elements of HST - In-The-Sky.org*. en. Library Catalog: in-the-sky.org. URL: https://in-the-sky.org/spacecraft_elements.php?id=20580&startday=1&startmonth=1&startyear=2020&endday=23&endmonth=4&endyear=2020 (visited on 04/23/2020).

[32] Dominic Ford. *Orbital elements of ISS - In-The-Sky.org*. en. Library Catalog: in-the-sky.org. URL: https://in-the-sky.org/spacecraft_elements.php?id=25544&startday=1&startmonth=1&startyear=2020&endday=31&endmonth=4&endyear=2020 (visited on 04/23/2020).

[33] *Space Research Facilities for Commercial Microgravity Research*. URL: https://nanoracks.com/products/ (visited on 06/05/2020).

[34] "COROT Mission Engineering: Cost-Effective Solutions for Stellar Photometry in Low Earth Orbit". en. In: *55th International Astronautical Congress of the International Astronautical Federation, the International Academy of Astronautics, and the International Institute of Space Law*. Vancouver, British Columbia, Canada: American Institute of Aeronautics and Astronautics, Oct. 2004. DOI: 10.2514/6.IAC-04-Q.1.01. URL: http://arc.aiaa.org/doi/10.2514/6.IAC-04-Q.1.01 (visited on 04/17/2020).

[35] *COROT mission strategy*. en. Library Catalog: www.esa.int. URL: https://www.esa.int/Science_Exploration/Space_Science/COROT/COROT_mission_strategy (visited on 04/17/2020).

[36] Dominic Ford. *Orbital elements of XMM-NEWTON - In-The-Sky.org*. en. Library Catalog: in-the-sky.org. URL: https://in-the-sky.org/spacecraft_elements.php?id=25989&startday=1&startmonth=1&startyear=2020&endday=23&endmonth=4&endyear=2020 (visited on 04/23/2020).

[37] *6 SmallSat Companies Building and Launching Satellites*. en-US. Library Catalog: www.nanalyze.com. Mar. 2019. URL: https://www.nanalyze.com/2019/03/smallsat-companies-building-launching-satellites/ (visited on 04/19/2020).

[38] Michel Capderou. *Handbook of Satellite Orbits*. en. Cham: Springer International Publishing, 2014. ISBN: 978-3-319-03415-7 978-3-319-03416-4. DOI: 10.1007/978-3-319-03416-4. URL: http://link.springer.com/10.1007/978-3-319-03416-4 (visited on 06/05/2020).

[39] WANG Chi. "Progress of Solar wind Magnetosphere Ionosphere Link Explorer(SMILE) Mission". en. In: (), p. 6.

[40] *ESA Science & Technology - Launch of XMM*. URL: https://sci.esa.int/web/xmm-newton/-/18135-launch-of-xmm (visited on 06/05/2020).

[41] David Gilmore. *Spacecraft Thermal Control Handbook, Volume I: Fundamental Technologies*. en. Washington, DC: American Institute of Aeronautics and Astronautics, Inc., Dec. 2002. ISBN: 978-1-884989-11-7. DOI: 10.2514/4.989117. URL: http://arc.aiaa.org/doi/book/10.2514/4.989117 (visited on 06/05/2020).

[42] Lionel Jacques. "Thermal Design of the Oufti-1 nanosatellite". en. In: (), p. 142.

[43] Eric W. Weisstein. *Runge-Kutta Method*. en. Text. Library Catalog: mathworld.wolfram.com Publisher: Wolfram Research, Inc. URL: https://mathworld.wolfram.com/Runge-KuttaMethod.html (visited on 06/07/2020).

[44] A Kellens. "Master thesis : Thermal design of the OUFTI-Next mission". en. In: (), p. 140.

[45] Jonathan Becedas and Andrés Caparrós. "Additive Manufacturing Applied to the Design of Small Satellite Structure for Space Debris Reduction". en. In: *Applications of Design for Manufacturing and Assembly*. Ed. by Ancuţa Păcurar. IntechOpen, Jan. 2019. ISBN: 978-1-78984-935-6 978-1-78984-936-3. DOI: 10.5772/intechopen.78762. URL: https://www.intechopen.com/books/applications-of-design-for-manufacturing-and-assembly/additive-manufacturing-applied-to-the-design-of-small-satellite-structure-for-space-debris-reduction (visited on 06/05/2020).

[46] *Coefficients of Linear Thermal Expansion*. URL: https://www.engineeringtoolbox.com/linear-expansion-coefficients-d_95.html (visited on 06/05/2020).

[47] *ESA Science & Technology - SMILE*. URL: https://sci.esa.int/web/smile (visited on 06/08/2020).